Delft University of Technology

Progress in CFD-based automated design with application to unconventional turbomachines

Anand, N.

DOI
10.4233/uuid:9d050254-0ff8-4f1c-81e0-15b02450edc6

Publication date
2021

Document Version
Final published version

Citation (APA)
Anand, N. (2021). *Progress in CFD-based automated design with application to unconventional turbomachines*. [Dissertation (TU Delft), Delft University of Technology].
https://doi.org/10.4233/uuid:9d050254-0ff8-4f1c-81e0-15b02450edc6

Important note
To cite this publication, please use the final published version (if applicable).
Please check the document version above.

Copyright
Other than for strictly personal use, it is not permitted to download, forward or distribute the text or part of it, without the consent of the author(s) and/or copyright holder(s), unless the work is under an open content license such as Creative Commons.

Takedown policy
Please contact us and provide details if you believe this document breaches copyrights.
We will remove access to the work immediately and investigate your claim.

This work is downloaded from Delft University of Technology.
For technical reasons the number of authors shown on this cover page is limited to a maximum of 10.

Progress in CFD-based automated design with application to unconventional turbomachines

Dissertation

for the purpose of obtaining the degree of doctor
at Delft University of Technology
by the authority of the Rector Magnificus Prof.dr.ir. T.H.J.J. van der Hagen,
chair of the Board of Doctorates,
to be defended publicly on
Monday, 31th of May 2021 at 12:30 hours

by

Nitish ANAND

Master of Science in Mechanical Engineering,
Delft University of Technology, the Netherlands,
born in Jamshedpur, India.

This dissertation has been approved by the promotors.

Composition of the doctoral committee:

Rector Magnificus	Chairperson
Prof.dr.ir. P. Colonna di Paliano	Delft University of Technology, promotor
Dr.ir. M. Pini	Delft University of Technology, copromotor

Independent members:

Prof.dr.ir. M. Vahdati	Imperial College London, United Kingdom
Prof.dr.ir. T. Verstraete	von Karman Institute, Belgium
Prof.dr.ir. D. von Terzi	Delft University of Technology
Dr.ir. L. Souverein	Ariane Group, Germany
Prof.dr.ir. S. A. Klein	Delft University of Technology (*reserve member*)

Other member:

Dr.ir. R. Pecnik	Delft University of Technology

This research was supported by Triogen BV and the Applied and Engineering Sciences Domain (TTW) of the Dutch Organization for Scientific Research (NWO), Technology Program of the Ministry of Economic Affairs, grant number 14711.

ISBN 978-94-6384-219-8

Copyright © 2021 by Nitish Anand[1]

All rights reserved. No part of the material protected by this copyright notice may be reproduced or utilized in any form or by any means, electronic or mechanical, including photocopying, recording or by any information storage and retrieval system, without the prior permission of the author. An electronic version of this thesis is available at `http://www.library.tudelft.nl`

Published by Nitish Anand, Delft.
Printed by Gildeprint - Enschede – www.gildeprint.nl
Cover Designed by Elisa Augusto Perpignan.

---

[1] Author e-mail address: `nitish.ug2@gmail.com`

Dedicated to my parents, Neeta and Umesh.

मेरे माता पिता, नीता और उमेश, को समर्पित।

Table of Contents

Summary

The urgent need to transition to a climate-neutral society requires rapid development and adoption of renewable technologies. Key enablers of conventional and future renewable energy conversion technologies are turbomachines. However, the specific requirements of these turbines and compressors, e.g. operation under highly non-uniform flow or with novel fluids, make the available design methods insufficiently capable of providing efficient designs. Hence, novel and disruptive design methods are pivotal to achieve a paradigm shift in turbomachinery performance across all energy technology platforms.

Thanks to the recent advancements in numerical methods and availability of high-performance computational resources, advanced automated design methods tailored to turbomachinery applications are now available. These methods will increasingly allow for the quick and optimum realization of the needed unconventional turbomachines. Besides, these methods lay the foundation stone for a more holistic multi-disciplinary design of turbomachinery in general.

Unconventional turbomachines which can greatly benefit from such methodological advancements are those whose performance is penalized by inherently non-uniform flows, like, for example, supersonic turbines and boundary-layer-ingestion fans. For these machines, not only the fluid dynamic efficiency can be unsatisfactory, but they also suffer from poor structural performance. To overcome these shortcomings, two strategies can be adopted: first, the non-uniform loading of the blades must be reduced and, second, the mechanical structure must be made optimally strong to withstand these loads without other detrimental effects.

This dissertation presents research on two automated CFD-based design methods for turbomachines affected by strong non-uniform flows. Specifically, a supersonic vane design method in part I and an adjoint-based optimization framework in part II.

One outcome of this research, described in part I of this dissertation, is a novel supersonic vane design method which generates geometries with higher fluid-dynamic performance and flow uniformity if compared to those obtained from computationally expensive fluid dynamics optimization methods. Besides, it also highlights that the symmetric configuration of supersonic vanes provides superior off-design performance in comparison to the asymmetric configuration.

The results reported in part II of this thesis show that a CAD-based blade parametrization approach increases the robustness of adjoint-based optimization methods. Furthermore, the synthesis and successful test of a computationally-efficient aeroelastic optimization framework using the harmonic-balance method is also presented and discussed.

Samenvatting

De dringende noodzaak om over te schakelen op een klimaatneutrale samenleving vereist een snelle ontwikkeling en toepassing van hernieuwbare technologieën. Turbomachines spelen een belangrijke rol in conventionele en toekomstige herniewbare energie conversie technieken. Echter, de specifieke vereisten aan deze turbines en compressoren leiden ertoe dat beschikbare ontwerpmethodes onvoldoende in staat om efficiente ontwerpen te maken. Daarom zijn nieuwe en disruptieve ontwerpmethodes van cruciaal belang om een paradigmaverschuiving teweeg te brengen in de prestaties van turbomachines voor alle energietechnologie platformen.

Dankzij de recente vooruitgang in numerieke methoden en de beschikbaarheid van krachtige rekenhulpmiddelen, zijn er nu geavanceerde geautomatiseerde ontwerpmethoden beschikbaar die zijn toegespitst op turbomachineprocessen. Deze methoden zullen in toenemende mate een snelle en optimale realisatie van de benodigde onconventionele turbomachines mogelijk maken. Bovendien leggen deze methoden de basis voor een meer holistisch multi-disciplinair ontwerp van turbomachines in het algemeen.

Onconventionele turbomachines die veel baat kunnen hebben bij dergelijke methodologische ontwikkelingen zijn die waarvan de prestaties worden benadeeld door inherent niet-uniforme stromingen, zoals bijvoorbeeld supersonische turbines en “boundary layer ingestion”. Voor deze machines kan niet alleen de vloeistofdynamische efficiëntie onbevredigend zijn, maar zij hebben ook slechte structurele prestaties. Om deze tekortkomingen te verhelpen kunnen twee strategieën worden gevolgd: ten eerste moet de niet-uniforme belasting van de schoepen worden verminderd en ten tweede moet de mechanische structuur optimaal sterk worden gemaakt om deze belastingen te weerstaan zonder andere nadelige effecten.

Dit proefschrift presenteert onderzoek naar twee geautomatiseerde op CFD gebaseerde ontwerpmethoden voor turbomachines die worden beïnvloed door sterke niet-uniforme stromingen. Om precies te zijn, de ontwerpmethode voor een supersonische schoep wordt gepresenteerd in deel I, en een optimalisatie structuur gepaseerd op de adjoint methode wordt gepresenteerd in deel II.

Een resultaat van dit onderzoek, beschreven in deel I van dit proefschrift, is een nieuwe ontwerpmethode voor supersonische schoepen die geometrieën genereert met hogere vloeistofdynamische prestaties en stromingsuniformiteit, in vergelijking met de ontwerpen verkregen met behulp van rekenintensieve met behulp van rekenintensieve

vloeistofdynamica-optimalisatiemethoden. Bovendien blijkt ook dat de symmetrische configuratie van supersonische schoepen superieure prestaties levert buiten de ontwerpconditie in vergelijking met de asymmetrische configuratie.

De resultaten in deel II van dit proefschrift tonen aan dat een op CAD gebaseerde benadering van de bladparametrisering de robuustheid van adjoint-gebaseerde optimalisatiemethoden verhoogt. Verder wordt ook de synthese en succesvolle test van een rekenkundig efficiënt aëro-elastisch optimalisatie raamwerk met behulp van de harmonische-balans methode gepresenteerd en besproken.

1

Introduction

1.1 Turbomachines for Next-Generation Power and Propulsion Systems

The current generation of the human kind is arguably the first to suffer from the irreversible effects of global warming. This is primarily due to the unconstrained industrial development which led to a surge in the global energy demand. Currently, this energy demand is met using fossil fuels which are responsible for gaseous emissions. The International Energy Agency (IEA) predicts approximately 40% increase in the consumption of energy by the year 2030 [1]. This is a result of the global population increase and the surge of the energy demand from developing nations. To enable the sustainable development of society, dependency on fossil fuels needs to be reduced and eventually eliminated [2]. This can be done by increasingly adopting renewable energy technologies which utilise resources like, wind, solar, geothermal, hydro and bio energy [3]. In the year 2019, only 28% of the global energy demand was met by renewable energy conversion [1]. To transition into a climate-neutral society, the share of exploited renewable energy source should rise to 57% of the total by year 2030 and at least to 85% by year 2050 [4], as per the Paris Agreement [5].

Currently, clean power is generated by means of a mix of green technologies which exploit low power-density energy resources, like, wind, solar radiation, geothermal reservoirs, and more recently also ocean tides and waves [6]. Thanks to these technologies, the share of renewable energy is expected to increase steadily in the future. However, high power-density renewable and non-renewable energy sources, like hydrogen and natural gas, will still be required to perform the needed grid balancing due to the intermittent nature of renewable energy generation. In addition, this type of fuels will be needed for intercontinental mobility and transport (e.g., long-haul flights, and freight shipping) because no alternative can be easily imagined for the foreseeable future [7].

A solution to this lack of high-power density renewable energy conversion needs are technologies employing turbomachines as prime movers. Unconventional turbomachines like those used in supercritical CO_2 power plants [8], organic Rankine cycle turbogenerators [9] and hydrogen-fired gas-turbine-based power plants [10] have emerged as alternatives. Moreover, new propulsion technologies like hybrid-electric and boundary layer ingestion propulsors are investigated as the evolution of conventional aero-engines [11]. Besides, turbomachines play a vital role in all existing renewable technologies (except solar PV), directly or indirectly, for pressurizing, expanding, pumping or cooling.

It is therefore clear that turbomachines are an essential component of all these systems and crucial to realize the envisaged climate-neutral future [12]. The permanent solution to the climate crisis can only be attained if novel turbomachinery technologies supporting the new green energy technologies are developed and made mainstream [2], especially in the power generation, mobility and transport sectors. Currently, the readiness level of such turbomachines is rather low, which points to a large potential for performance improvements [13].

The needed performance improvement of turbomachinery in the readiness level of novel green conversion technologies can be achieved by enhancing design methods, manufacturing techniques, and materials. Novel and disruptive design methods are pivotal to obtain a paradigm shift in turbomachinery performance across all energy technologies.

In the past, the development of turbomachines, mostly relied on mean-line and throughflow calculations for design purposes. The obtained design was then verified by extensive fluid, structural, vibration and rotor-dynamic analysis, and finally the design chain was closed by testing the prototype in an experimental setup. In this design process, any suboptimal performance detected during the analysis or the testing phase, led to the repetition of the entire design chain starting from the mean-line design. This made the entire process extremely expensive and cumbersome. In contrast, the next-generation of turbomachinery prototypes will rely on a more holistic multi-disciplinary design approach [14]. In this approach, coupled physical phenomena, like fluid dynamics, heat transfer, structural dynamics and acoustics will be dealt with simultaneously. In addition, the optimization process will encompass multiple operating conditions, or even, possibly, dynamic operation. Examples are part-load operation in stationary or mobile power systems, or operation of aero-engines under the influence of strong flow non-uniformity or durable operation of rocket or aircraft engines under extreme vibrations experienced during lift-off or take-off.

This is clearly a gigantic endeavor. This projected design procedure will rely on much more accurate simulations and, very importantly, will drastically reduce the prototype development time. Prime enablers of such a multi-disciplinary design framework are CFD-based design methods. In the last decades, the design of compressors, turbines and pumps has increasingly relied on high-fidelity CFD simulations, consequently leading to the evolution of several turbomachinery-specific CFD-based analysis and design tools [15]. High-fidelity CFD-based design methods are expected to become the backbone of turbomachinery design, thanks to the ever reducing cost of computer hardware, and increase of computational performance and data storage capacity, together with the continuous development of numerical methods.

A numerical design framework which includes coupled physics taking into account application-specific operational conditions and interaction effects among upstream and downstream components will result in what nowadays are called digital-twins of turbomachines, though very small modelling errors and simplifications with respect to true operational conditions will always be unavoidable.

One of the most relevant categories of turbomachinery which can greatly benefit from methodological advancements is that of compressors and turbines operating under highly transonic and supersonic flow and under highly non-uniform flow conditions which can arise due to transient operation or asymmetric inlet flow due to requirements posed by certain propulsion concepts. This happens, for instance, in rocket-engine turbopumps and in the envisaged boundary layer ingestion fans of next-generation aircraft propulsors.

1.1.1 Supersonic turbines

In the 1960s a need for ultra compact high-performance turbopumps arose to complement the large rocket engines powering the space exploration program [16]. The only type of turbine that can achieve high work output, has a compact size and is light weight was and still is the impulse supersonic turbine. As the name suggests, these turbines operate at supersonic flow conditions because of their high-expansion ratio, resulting from the constraint of keeping the number of stages to a minimum. Other than in rocket engines, supersonic turbines were also used for the first stages of high-expansion ratio steam and gas turbines [17, 18, 19] and in small auxiliary turbines [20].

Today supersonic turbines play a pivotal role in several propulsion and power systems. For instance, in supersonic military aircraft engines [21, 22], as an alternative to Joules-Thompson valves commonly used for expanding cryogenic fluids [23, 24], in place of the expansion valve in heat pumps [25, 26], and as expanders in supercritical CO_2 Brayton cycle [8] power plants. Apart from these examples, perhaps the most impactful application of supersonic turbines today is in organic Rankine cycle power plants [9].

The organic Rankine cycle (ORC) concept is a derivative of the steam Rankine cycle whereby an organic compound is the working fluid instead of water. The possibility to select from a wide range of organic compounds makes the ORC power technology extremely flexible. This is because, the proper selection of the working fluid allows ORC systems to be tailored to the conversion of energy sources that are widely different in terms of temperature and capacity. Steam power plants are limited to the conversion of thermal energy sources at temperature levels higher than $\sim$ 400 °C and thermal power larger than tens of MW [9]. ORC power plants are currently employed to convert into electricity as diverse energy sources as geothermal reservoirs [27], biomass fuels [28] concentrated solar radiation [29], and, importantly, waste heat [9].

Large scale ORC units are widely adopted in case of water or polluted steam geothermal reservoirs, in biomass combustion or gasification power plants and for boosting the efficiency of co-generation power stations and of integrated desalination plants [28]. The use of ORC technology for waste heat recovery from large thermal energy sources is increasing. In addition, more recently, small-scale ORC units, see Figure 1.2, are investigated as waste heat recovery devices for automotive engines [30], highly decentralized biomass power units [31], low temperature industrial and domestic waste heat recovery [32]. Small ORC energy converters are also studied as power units for satellites [33, 34, 35], as components of thermal storage devices [36], and are considered for waste heat recovery on board of aircraft [37, 38].

The techno-economic viability of large scale ORC power plants [40] is testified by the successful establishment of several manufacturing companies starting from the 1970s [41]. In contrast, small scale ORC technology has not become mainstream yet because of tightly intertwined technical and economical reasons. From a technical perspective, this is primarily due to the inherent low energy conversion efficiency of small ORC systems if compared to large ORC systems. In order to achieve sufficiency large conversion

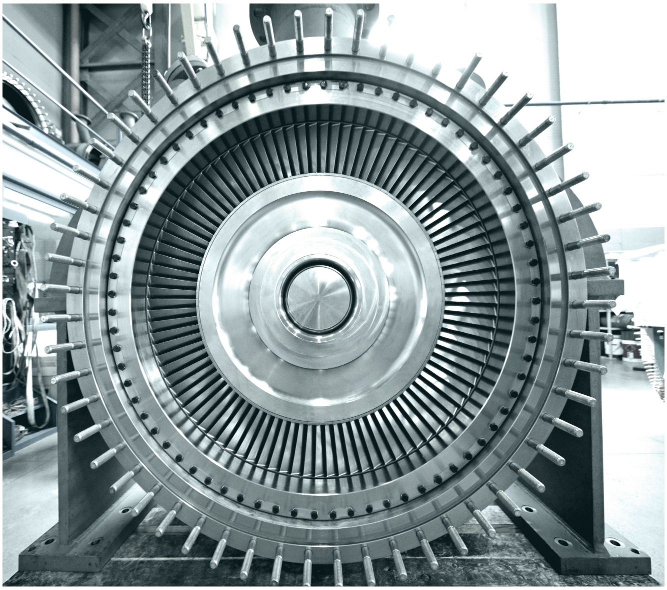

Figure 1.1: Inside of the the casing of a 10 MW organic Rankine cycle turbine, courtesy of Turboden.

efficiency, the turbine inlet temperature must be sufficiently high, which in turns entails high turbine expansion ratio [9]. Given that, in order to keep the cost low, single-stage turbines are preferable, and this leads to supersonic flow conditions in the stator of the turboexpander. As a consequence, strong shockwaves are bound to form in the flow passages causing high fluid dynamic losses, unless sophisticated design solutions are adopted. This in turn provokes highly non-uniform flow at the stator outlet which affects the efficient operation of the rotor downstream. In addition, high flow non-uniformity causes unsteady loading on the rotor blades, which might induce structural fatigue and premature failure [42].

Although small-scale ORC systems are extremely attractive as a green technology, the realisation of efficient designs, which is mandatory for economic viability, is still challenging. A paradigm shift in the performance of supersonic turbines can only be achieved with an advanced automated design methodology that enables to mitigate the formation of strong shockwaves in the stationary vanes.

1.1.2 Transonic boundary layer ingestion fans

Fuel efficiency of jet engines has been of concern since the beginning of the ‘Jet Age’. Today, engines used in commercial aircraft are substantially more efficient compared to the first generation of simple jet engines. This is primarily due to the improvements in

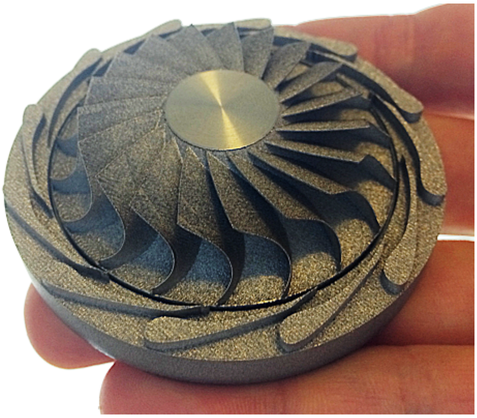

Figure 1.2: Mockup of the rotor and stator assembly of a 10 kW high-speed organic Rankine cycle turboexpander being realized by the Propulsion and Power group of TU Delft [39].

the propulsive and thermal efficiency of the system which took place during the last six decades. In the next decade, it is envisaged that a substantial gain in propulsive efficiency will be achieved by implementing novel propulsion system concepts [11], for example, open-rotor engines [43], ultra-high bypass ratio turbofans [44] and boundary layer ingestion propulsors [45], which is perhaps the configuration with the highest potential for improvement.

The idea of a propulsor with boundary layer ingestion (BLI) was first conceived in the 1920s [46]: propulsor efficiency increases if the velocity of the airflow aspirated by the fan is lower than that of the free stream [11]. The concept was originally developed for the propulsion system of hydro submerged bodies, like, for example, torpedoes and ships [47]. In addition, it is reported [48] that unpublished documents mention that a propulsion system with BLI was used in early aerial cruise missiles.

Today, the quest to make commercial aviation climate-neutral has brought the BLI propulsor concept back at the epicentre of global research. A recent study mentions that the integration of the BLI propulsor with the aircraft fuselage promotes the ingestion and the transfer of energy to the air boundary layer and can lead to an increase in propulsive efficiency of up to ~8% [49, 50, 51]. Based on these findings, aircraft concepts which can benefit from BLI propulsors, like the *propulsive fuselage concept* (see Figure 1.3), has emerged and are being actively studied [52, 53]. In addition, the BLI propulsor concept is rather flexible, therefore it can be applied to turbofan, hybrid electric [54] or distributed electric [55] configurations.

Although extremely attractive as an alternative to conventional podded aircraft engines, the BLI propulsor concept poses severe design challenges. For instance, in case of the podded turbo-fan engines hanging under the wing, the fan inlet is exposed to rel-

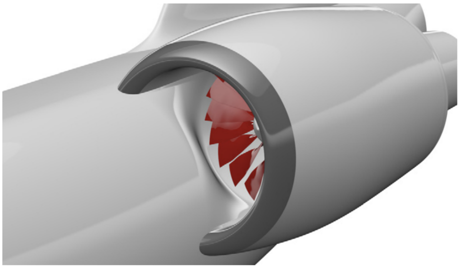

Figure 1.3: Illustration of a boundary layer ingestion propulsor integrated with the aircraft fuselage. Image taken from Ref. [56].

atively uniform flow. This is desirable for turbomachinery engineers as the fan blades experience constant pressure and flow with each rotation. In contrast, a BLI turbofan engine encounters a distorted low-momentum boundary layer emerging from the aircraft surface, consequently, exposing the fan blades to non-uniform airflow at every revolution [57]. This would penalise the efficiency, noise, operability and life of the engine, if the BLI configuration were implemented with current state-of-the art fan and fan installation technology. Overcoming this challenge will require the detailed assessment of the deficiencies inherent in current technology, as well as pursuing design solutions that can mitigate such drawbacks [58].

In order to mitigate the issues associated with non-uniform flow in the BLI fans, advanced automated design methods which can efficiently handle complex multi-disciplinary design problems are required. Adjoint-based optimization is one of such design methods that can handle complex design problems efficiently [59]. Hence, a cost effective adjoint-based aeroelastic design framework capable of handling problems similar to that of BLI fans can potentially provide a solution to the design challenges of BLI fans.

1.2 Automated turbomachinery design

Turbomachines operating under non-uniform flow conditions suffer from aerodynamic performance penalties and pre-mature structural failure [42]. In order to overcome these issues, design methods able to mitigate the negative impact of non-uniform flow are essential. This goal can be effectively achieved in two successive steps: first, by obtaining an optimum baseline geometry through aerodynamic design methods accounting for non-uniform flow effects and, second, by performing the aeroelastic design optimization of this baseline, yet already well-designed, geometry having as objective function the maximization of the life-span of the component.

Thanks to the ever reducing cost of high performance computers and their memory, the use of automated design methods is increasingly spreading and is entering the routine design process. Automated design methods can be classified into aerodynamic [60, 61, 62, 63], aeroelastic [64] and multi-disciplinary [65] design methods, in order of increasing complexity. These methods are applicable to turbomachines operating with both uniform and non-uniform flow conditions.

This dissertation presents two automated methods which address the knowledge gap associated with the design of turbomachines operating with non-uniform flows. One pertains to the detailed design of the stator vanes of supersonic turbines, while the other regards a cost-effective adjoint-based aero-structural shape optimization framework.

Supersonic stator vane design. A design method to obtain a shock free supersonic stator is essential to drastically improve the techno-economic viability of small-scale ORC turbines. The design of supersonic devices, like turbines and ducts in general, differs from their transonic/subsonic counterparts, primarily because the local flow properties depend on the flow characteristics downstream. Hence to design supersonic devices, a precise control over the cross-section and flow angle distribution is required in order to abate the strenght of shockwaves in the flow passage or to prevent their formation altogether.

A well-known method to design supersonic flow devices is the *method of characteristics*. This method, when extended to non-ideal flow conditions and coupled with a unified geometrical transformation method, provides optimal blade shape configurations for supersonic stators. This topic is treated in Part I of this dissertation.

Adjoint-based aero-structural shape optimization. Turbomachines operating under the influence of strong non-uniform flow often suffer from premature structural failure primarily due to vibrational resonance, also known as forced response [42]. Forced response is a phenomenon in which the flow unsteadiness excite the blades natural frequency, adding more energy to the vibration and ultimately causing failure. Designing a reliable turbine or compressor that can sustain vibration over its life-span, which can range from 5 minutes in a rocket engine to 15 years in an industrial gas turbine, is essential.

Currently, forced response analysis is performed using the modal-superposition method. However, due to the high manual labour and computational cost, a design framework in which the whole process is automated would arguably be inefficient.

An alternative to the modal superposition method is the *energy method* which is less laborious. In addition, if coupled with the *harmonic balance method* to solve unsteady Reynolds averaged Navier Stokes equations, the computational cost can be substantially reduced. It is therefore possible to obtain a cost-effective, automatic design framework by solving the adjoint equations associated with the unsteady harmonic balance simulation. Part II covers research about this subject.

The objective of the research documented in this dissertation is to conceive and develop automated design methods for unconventional turbomachinery to reduce the effect of non-uniform flows on fluid-dynamic and structural performance.

1.3 Original contributions

The research contributions documented in this dissertation can be summarized as follows.

- A generalised vane generation methodology for radial and axial supersonic vanes was conceived, developed and employed in order to verify its capabilities. It is based on the method of characteristics extended to fluid flows in the non-ideal compressible regime. This geometry generation method is the state-of-art for the design of supersonic stators. This method was used to design the supersonic vanes of the ORCHID turbine, a research high-speed ORC turbine being realized by the Propulsion and Power group of TU Delft, and to improve the stationary blades of the centripetal turbine equipping the Triogen ORC system, which is commercially available. The code was developed using the python language and is available open-source.

- A reduced order method to estimate the preliminary design parameters of ORC stators was devised. Using this method, the applicability and accuracy of an existing method to estimate the optimum preliminary design parameters was assessed. In addition, based on this method, design guidelines for supersonic ORC stator vanes were drawn.

- A generalised CAD-based blade parameterisation software tool was conceived, developed and employed in some realistic design cases. The program provides surface sensitivity using the complex-step method, which is crucial for gradient-based shape optimization. The code was coupled with the adjoint solver of SU2, a multi-physics modeling, simulation and design software suite. The parametrisation code was also developed with the python language and is available open-source.

- A full-3D adjoint-based aerodynamic and aero-elastic shape optimization framework was conceived and implemented. It is coupled with the above-mentioned CAD-based parametrisation program. The adjoint sensitivities were validated using a first-order forward finite-difference method. The optimization framework was tested by computationally improving the estimated performance of exemplary transonic turbomachines.

All the new methods presented in this dissertation are implemented in the open-source SU2 software suite or in stand-alone open-source python packages. The combination of software allowing for adjoint-based steady/unsteady shape optimization using CAD-based parametrisation and the fact that all these tools are made available open source is also deemed an original contribution of the work documented in this dissertation.

1.4 Outline

This dissertation is divided into two parts. Part I, focuses on the supersonic stator vane design method, while Part II concerns the adjoint-based optimization. The content of this dissertation is organised in six chapters and a brief summary of the following five chapters is listed below.

Part I: Supersonic vane design

Chapter 2 presents a generalised design methodology to generate axial and radial supersonic vane geometries in asymmetric and symmetric vane configurations. The proposed design method was utilised to obtain geometries for an industrial partner. The performance of the obtained stator vane is compared numerically with that currently in use in operating machines using CFD.

Chapter 3 reports a study on the accuracy of Deych's law, which is commonly used to select optimal preliminary design parameters for supersonic vanes. The optimum design parameters obtained with this method is compared with that obtained from the newly developed method, namely a method based on analytical and CFD calculations.

Part II: Adjoint-based shape optimization

Chapter 4 introduces a new blade parametrisation procedure, tailored to adjoint-based shape optimization. The method is coupled with the SU2 adjoint solver. The proposed framework was then used to perform gradient validation and shape optimization of an axial transonic turbine cascade.

Chapter 5 treats an aeroelastic optimization framework employing the harmonic balance method. The mathematical formulation of the objective function and of the sensitivity information is also described. The method was applied to optimize an axial transonic fan.

Chapter 6, Conclusions and recommendations summarises the main findings and the limitations of the documented research. Alongside, it provides a compass for future research directions.

References

[1] Various Authors, 2020. *Global Energy & CO_2 Status Report: The latest trends in energy and emissions*. International Energy Agency.

[2] Various Authors, 2020. *Global Renewables Outlook: Energy transformation 2050*. International Renewable Energy Agency, April.

[3] Various Authors, 2020. *Renewable Energy Statistics 2020*. International Renewable Energy Agency.

[4] Various Authors, 2019. *Going climate-neutral by 2050 - "A strategic long-term vision for a prosperous, modern, competitive and climate-neutral EU Economy"*. European Commission.

[5] United Nations, 2015. Paris agreement. Online Link [Accessed: 10-02-2021]. UN Treaty: Treaty No. XXVII-7-d.

[6] Ghosh, T. K., and Prelas, M. A., 2011. *Energy Resources and Systems: Renewable Resources*, Vol. 2. Springer.

[7] Garcia-Olivares, A., Sole, J., and Osychenko, O., 2018. "Transportation in a 100% renewable energy system". *Energy Conversion and Management,* **158**, pp. 266–285.

[8] Samad, T. E., and J. Amaral Teixeira, a. J. O., 2020. "Investigation of a radial turbine design for a utility-scale supercritical CO_2 power cycle.". *MDPI Applied Science,* **10**(4168), pp. 1–26.

[9] Colonna, P., Casati, E., Trapp, C., Mathijssen, T., Larjola, J., Turunen-Saaresti, T., and Uusitalo, A., 2015. "Organic Rankine cycle power systems: From the concept to current technology, applications, and an outlook to the future". *Journal of Engineering for Gas Turbines and Power,* **137**(10), p. 100801 (19 pages).

[10] Chiesa, P., Lozza, G., and Mazzocchi, L., 2005. "Using hydrogen as gas turbine fuel". *Journal of Engineering for Gas Turbines and Power,* **127**(1), pp. 73–80.

[11] Nelson, E. S., and Reddy, D. R., 2013. *Green Aviation: Reduction of Environmental Impact Through Aircraft Technology and Alternative Fuels*, Vol. 14. CRC Press.

[12] Various Authors, 2013. "NASA Tech Briefs Magazine". *SAE International,* **37**(5), May.

[13] Gokarakonda, S., Hennicke, P., Moore, C., Thomas, S., and Venjakob, M., 2018. "Relevant technologies for the energy transition in germany with potential relevance for Japan". *Wuppertal Institute for Climate, Environment and Energy*, February.

[14] Verstraete, T., Aissa, M., and Mueller, L., 2018. *Multidisciplinary Optimization of Turbomachinery Components using Differential Evolution*. No. LS 2018-04. von Karman Institute for Fluid Dynamics, Belgium, September.

[15] Horlock, J. H., and Denton, J. D., 2005. “A review of some early design practice using computational fluid dynamics and a current pespective”. *Journal of Turbomachinery,* **1**(175), 02, pp. 5–13.

[16] Moffitt, T. P., 1958. Design and experimental investigation of a single-stage turbine with a rotor entering relative Mach number of 2. Tech. rep., National Advisory Committee for Aeronautics.

[17] Stratford, B. S., and Sansome, G. E., 1959. “The performance of supersonic turbine nozzles”. *Aeronautical Research Council Reports and Memoranda*(3273), pp. 1–33.

[18] Colclough, C. D., 1966. “Design of turbine blades suitable for supersonic relative inlet velocities and the investigation of their performance in cascades: Part i-theory and design”. *Journal of Mechanical Engineering Science,* **8**(1), pp. 110–128.

[19] Colclough, C. D., 1966. “Design of turbine blades suitable for supersonic relative inlet velocities and the investigation of their performance in cascades: Part ii-experiments, results and discussion”. *Journal of Mechanical Engineering Science,* **8**(2), pp. 185–197.

[20] Ohlsson, G. O., 1964. “Supersonic turbines”. *Journal of Engineering for Gas Turbine and Power,* **1**(86), pp. 7–12.

[21] Sohn, C. W., Holcomb, F. H., Baldwin, P., Lawlor, S., Steele, R. C., and Belshaw, K., 2006. Ramgen power systems-supersonic component technology for military engine applications. Tech. rep., Energy Branch U.S. Army Corps of Engineers.

[22] Sun, H., Qin, J., Li, H., Huang, H., and Yan, P. “Research of a combined power and cooling system based on fuel rotating cooling air turbine and organic Rankine cycle on hypersonic aircraft”. *Energy,* **189**, p. 116183 (13 pages).

[23] Verma, R., Sam, A. A., and Ghosh, P., 2015. “CFD analysis of turbo expander for cryogenic refrigeration and liquefaction cycles”. In Proceedings of 25th International Cryogenic Engineering Conference and the International Cryogenic Materials Conference, Physics Procedia 67, pp. 373–378.

[24] Song, P., Sun, J., and Wang, K., 2015. “Swirling and capitation flow suppression in a cryogenic liquid turbine expander through geometric optimization”. *Journal of Power and Energy,* **229**(6), pp. 628–646.

[25] Chua, K., Chou, S., and Yang, W., 2010. “Advances in heat pump systems: A review”. *Applied Energy,* **87**(12), pp. 3611 – 3624.

[26] Hays, L., and Brasz, J. J., 2004. “A Transcritical CO_2 Turbine-Compressor”. In Proceeding of International Compressor Engineering Conference, no. C137, p. 1628.

[27] Moloney, F., Almatrafi, E., and Goswami, D., 2017. “Working fluid parametric analysis for regenerative supercritical organic rankine cycles for medium geothermal reservoir temperatures”. In Proceeding of 4th International Seminar on ORC Power Systems September 13-15th 2017, 129, Energy Procedia, pp. 599 – 606.

[28] Tian, H., and Shu, G. Q., 2017. “Organic Rankine Cycle systems for large-scale waste heat recovery to produce electricity”. In *Organic Rankine Cycle (ORC) Power Systems*. Woodhead Publishing, pp. 613 – 636.

[29] Ferrara, F., Gimelli, A., and Luongo, A., 2014. “Small-scale concentrated solar power (CSP) Plant: ORCs comparison for different organic fluids”. In Proceedings of 68th Conference of the Italian Thermal Machines Engineering Association, 45, Energy Procedia, pp. 217 – 226.

[30] Noriega, S. B., de Servi, C., and Colonna, P., 2020. “Hybrid electric powertrain for long-haul trucks and buses: Preliminary analysis of a new concept based on a combined cycle power plant.”. *Journal of the Global Power and Propulsion Society,* **4**, pp. 63–79.

[31] Moradi, R., Marcantonio, V., Cioccolanti, L., and Bocci, E., 2020. “Integrating biomass gasification with a steam-injected micro gas turbine and an organic Rankine cycle unit for combined heat and power production”. *Energy Conversion and Management,* **205**(112464), pp. 1–12.

[32] Kolasiński, P., Błasiak, P., and Rak, J., 2017. “Experimental investigation on multi-vane expander operating conditions in domestic CHP ORC system”. In Proceeding of 4th International Seminar on ORC Power Systems September 13-15th 2017, 129, Energy Procedia, pp. 0–8.

[33] Angelino, G., DeLuca, L., and Sirignano, W. A., 1991. “Modern research topics in aerospace propulsion: In honor of Corrado Casci”. *Springer Science Business Media*.

[34] Dorney, D. J., Griffin, L. W., Huber, F. W., and Sondak, D. L., 2003. “Off-design performance of a multi-stage supersonic turbine”. In Proceeding of 41th Aerospace Sciences Meeting and Exhibit, no. AIAA 2003-1212, AIAA, pp. 0–23.

[35] Leverone, F., Pini, M., Cervone, A., and Gill, E., 2020. “Solar energy harvesting on-board small satellites”. *Renewable Energy,* **159**, pp. 954 – 972.

[36] Rodríguez, J. M., Sánchez, D., Martínez, G. S., Bennouna, E. G., and Ikken, B., 2016. “Techno-economic assessment of thermal energy storage solutions for a 1mwe csp-orc power plant”. *Solar Energy,* **140**, pp. 206 – 218.

[37] Saadon, S., and Talib, A. R. A., 2016. “An analytical study on the performance of the organic Rankine cycle for turbofan engine exhaust heat recovery”. In Proceeding of IOP Conference Series: Materials Science and Engineering, Vol. 152, IOP Publishing, p. 012011.

[38] Zarati, K., Maalouf, S., and Isikveren, A., 2017. “Potential of the bottom organic Rankine cycle to recover energy on turboprop engine architecture”. In Proceedings of ISABE-2017, no. 21345, pp. 0–20.

[39] Servi, C. D., Azzini, L., Pini, M., Rao, A. G., and Colonna., P., 2017. “Exploratory assessment of a combined-cycle engine concept for aircraft propulsion.”. In Proceedings of the 1st Global Power and Propulsion Forum, no. GPPF-2017-78, Global Propulsion and Power Society, pp. 1–11.

[40] Quoilin, S., Broek, M. V. D., Declaye, S., Dewallef, P., and Lemort, V., 2013. “Techno-economic survey of Organic Rankine Cycle (ORC) systems”. *Renewable and Sustainable Energy Reviews,* **22**, pp. 168 – 186.

[41] Tartiere, T., and Astolfi, M., 2017. “A world overview of the organic Rankine cycle market”. In Proceedings of IV Internation Seminar on ORC Power Systems, no. 129(2017), Energy Procedia, pp. 1–9.

[42] Srinivasan, A. V., 1997. “Flutter and Resonant Vibration Characteristics of Engine Blades”. In Proceedings of TurboExpo 1997, no. 97-GT-533, pp. 1–36.

[43] Hendricks, E. S., and Tong, M. T., 2012. “Performance and weight estimates for an advanced open rotor engine”. In Proceedings of 48th AIAA/ASME/SAE/ASEE joint Propulsion Conference & Exhibit, no. AIAA 2012-3911, pp. 1–13.

[44] Vetters, D. K., Karam, M., and Fulayter, R. D., 2014. “Ultra high bypass ratio turbofan engine”. No. US 2014/0363276 A1. United States Patent Application Publication, pp. 1–6.

[45] Plas, A., Crichton, D., Sargeant, M., Hynes, T., Greitzer, E., Hall, C., and Madani, V., 2012. “Performance of a boundary layer ingestion (BLI) propulsion system”. In Proceedings of 45th AIAA Aerospace Sciences Meeting and Exhibit, no. AIAA 2007-450, AIAA.

[46] Fage, A., and Collins, H. E., 1920. An investigation of the mutual interaction of airscrews and bodies of the pusher type. Tech. rep., Technical Report, Advisory Committee for Aeronautics.

[47] Wislicenus, G. F., and Smith, L. H., 1953. Hydraulic jet propulsion and incipient cavitation. Tech. Rep. I-6, John Hopkins University.

[48] Smith, L. H., 1993. “Wake ingestion propulsion benefit”. *Journal of Propulsion and Power,* **9**(1), pp. 74–82.

[49] Hendricks, E. S., 2018. *A Review of Boundary Layer Ingestion Modeling Approaches for use in Conceptual Design.* No. NASA/TM—2018-219926. Glenn Research Center, Cleveland, Ohio.

[50] Plas, A. P., Sargeant, M. A., Madani, V., Crichton, D., Greitzer, E. M., Hynes, T. P., and Hall, C. A., 2007. “Performance of a boundary layer ingesting (bli) propulsion system”. In Proceedings of 45th AIAA Aerospace Sciences Meeting and Exhibit, no. AIAA 2007-450, AIAA.

[51] Arnhem, N. V., 2015. “Design and analysis of an installed pusher propeller with boundary layer inflow”. *MSc Thesis, Delft University of Technology*(047-15-MT-FPP).

[52] Seitz, A., and Gologan, C., 2015. “Parametric design studies for propulsive fuselage aircraft concepts”. *CEAS Aeronautical Journal*(6), pp. 69–82.

[53] Kenway, G. K. W., and Kiris, C., 2018. “Aerodynamic shape optimization of the starc-abl concept for minimal inlet distortion”. In Proceedings of AIAA SciTech Forum, no. AIAA 2018-1912, AIAA, pp. 1–14.

[54] Hoogreef, M., de Vries, R., Sinnige, T., and Vos, R., 2020. “Synthesis of aero-propulsive interaction studies applied to conceptual hybrid-electric aircraft design”. In Proceeding of AIAA SciTech 2020 Forum, no. AIAA 2020-0503, AIAA, pp. 1–25.

[55] de Vries, R., Hoogreef, M. F., and Vos, R., 2019. “Preliminary sizing of a hybrid-electric passenger aircraft featuring over-the-wing distributed-propulsion”. In Proceedings of AIAA Scitech 2019 Forum.

[56] Romani, G., Ye, Q., Avallone, F., Ragni, D., and Casalino, D., 2020. “Numerical analysis of fan noise for the nova boundary-layer ingestion configuration”. *Aerospace Science and Technology,* **96**(105532), pp. 1–22.

[57] Geiselhart, K. A., Daggett, D. L., Kawai, R., and Friedman, D., 2003. Blended wing body systems studies: boundary layer ingestion inlets with active flow control. Tech. Rep. Nasa/Cr-2003-212670, National Aeronautics and Space Administration.

[58] Propulsion, C. A., Global, R., and Emissions, C., 2016. *Commercial aircraft propulsion and energy systems research: Reducing global carbon emissions.*

[59] Pironneau, O., 1974. “On optimum design in fluid mechanics”. *Journal of Fluid Mechanics,* **64**(1), pp. 97–110.

[60] Vitale, S., Albring, T. A., Pini, M., Gauger, N. R., and Colonna, P., 2017. “Fully turbulent discrete adjoint solver for non-ideal compressible flow applications”. *Journal of the Global Power and Propulsion Society,* **1**, pp. 252–270.

[61] Paniagua, G., Iorio, M. C., Vonha, N., and Sousa, J., 2014. “Design and analysis of pioneering high supersonic axial turbines”. *International Journal of Mechanical Sciences*(89), pp. 65–77.

[62] Wheeler, A. P. S., and Ong, J., 2013. "The role of dense gas dynamics on ORC Turbine performance". *Journal of Engineering for Gas Turbine and Power,* **135**(8), p. 082604 (9 pages).

[63] Rubino, A., Pini, M., Colonna, P., Albring, T., Simmagadda, S., Economon, T., and Alonso, J., 2018. "Adjoint-based fluid dynamic design optimisation in quasi-periodic unsteady flow problems using a harmonic balance method". *Journal of Computational Physics,* **372**, 11, pp. 220–235.

[64] Wang, D. X., and He, L., 2009. "Concurrent Aerodynamic-Aeromechanic Design Optimization for Turbomachinery Blades Using Adjoint Method". In ASME TurboExpo, no. GT2009-59240, ASME, pp. 373–383.

[65] Verstraete, T., A. Z., and Van den Braembussche, R. A., 2010. "Multidisciplinary optimization of a radial compressor for microgas turbine applications.". *ASME. Journal of Turbomachinery,* **132**(3), March, p. 031004 (7 pages).

Part I
Supersonic vane design

The defining feature of supersonic turbines is the very high expansion and volumetric flow ratio. In particular, the stators of these turbines are bound to operate at highly supersonic flow conditions. This leads to the formation of shock-waves in the flow passages, which causes high fluid-dynamic losses. Study shows that the largest share of overall losses in supersonic turbines is due to high fluid velocity and shocks in the highly-loaded stators. As a result, a method to design efficient and possibly shock-less stationary vanes is essential to exploit the full potential of supersonic turbine technology.

This part of the thesis presents a methodology to design supersonic stators operating in non-ideal flow conditions. In addition, the sensitivity of the vane performance with respect to the design parameters is assessed. Using this design method and the guidelines drawn from the sensitivity analysis, an efficient supersonic vane geometry can be obtained without resorting to computationally expensive optimization calculations.

The design procedure presented in Chapter 2 employs the method of characteristics and a unified geometrical transformation strategy and is applicable both to radial and to axial supersonic vanes, in asymmetric and symmetric configurations. The performance of the obtained vanes is then assessed at on- and off-design conditions by means of computational fluid dynamics simulations. The method was tested with the aim of establishing a unified design methodology for axial and radial supersonic vanes of small-scale ORC turbines.

Chapter 3 describes the assessment of the accuracy and applicability of the only design rule to estimate preliminary design parameters for supersonic vanes. The assessment consists in a comparison among the preliminary design parameters obtained with the Deych's law and those estimated with two other methods, namely, an analytical procedure and those resulting from CFD simulations. The analytical method is based on a physical model of the flow through the passages to estimate fluid-dynamic losses. The CFD-based calculation of the design parameters uses the geometry generation sequence described in Chapter 2. The result of this comparison are design guidelines for supersonic vanes of small-scale ORC turbines and could easily be extended to other type of supersonic turbomachinery.

2

Automated design method for asymmetric and symmetric supersonic stators

The content of this paper will be submitted for publication to the
Journal of Engineering for Gas Turbines and Power as

N. Anand, P. Colonna, M. Pini, 2021.
Comparative Assessment of Asymmetric and Symmetric Supersonic Vanes at
On- and Off-Design Conditions for High-Temperature Organic Rankine Cycle Turbines.

Abstract *Fluid-dynamic losses in high-temperature mini organic Rankine cycle turbines occur mainly in the stationary vane flow passages. This is due to the inherently high expansion ratio of these turbines, which leads to the onset of strong shock waves and shock-induced entropy generation. Moreover, the flow characteristics of the supersonic nozzle greatly affects the fluid dynamic efficiency of the rotor, which depends from the direction and strength of shocks emanating from the nozzle, and, also related to them, from flow uniformity at the outlet of the nozzle. A suitable method to design efficient supersonic vanes is thus essential to achieve a sufficiently high fluid-dynamic performance of the turbine.*

This chapter presents two conceptually different vane design methods based on the method of characteristics extended to non-ideal flows and applicable to both axial and radial configurations. The methods are applied to design the supersonic stator of a high-temperature organic Rankine cycle turbine employing toluene as the working fluid. The stator of the turbine was previously designed by means of computationally expensive CFD-based shape optimization methods and the turbine performance was experimentally tested. The comparative assessment of the vane geometries provided by the two methods, referred to as symmetric and asymmetric vane, is carried out by computing their on- and off-design performance, expressed in terms of entropy-based loss coefficient and flow uniformity downstream of the cascade. The results pertaining to nominal operating conditions show comparable fluid dynamic performance. However, at part-load conditions, the symmetric vane design yields superior fluid dynamic performance. The next generation of axial and radial turbines for high-temperature mini organic Rankine cycle power plants should then be equipped with symmetric-shape stators because they provide higher overall turbine efficiency over the entire operating envelope. Moreover, performance data obtained through experiments show that supersonic stators designed using the proposed method perform better than those designed using computationally expensive optimization methods.

2.1 Introduction

A defining feature of single-stage turbines for small-scale high-temperature organic Rankine cycle (ORC) turbogenerators is the very high expansion and volumetric flow ratio. Due to this reason, the turbine stator operates with highly supersonic flows [1]. Moreover, the flow expansion within the stator passages occurs, to a large extent, in the so-called non-ideal compressible regime [2]. The combination of supersonic conditions and non-ideal flow effects complicates the understanding of the underlying flow physics, associated loss mechanisms and the relative implications in terms of optimal blade design. The optimal performance of the stator is arguably very critical, as an inefficient design prevents the attainment of high turbine efficiency considering that the stator alone accounts for two-thirds of the total fluid-dynamic losses [3, 4]. Given that the viability of the technology significantly depends on overall conversion efficiency, which in turn is determined to a large extent by turbine performance, the optimal design of the stator is of the utmost importance.

Research activities on high-temperature ORC technology recently increased, owing to the possibility of employing these systems as energy harvesters in mobile and distributed applications [5]. Currently, only a limited body of literature covers methods for the design of supersonic radial ORC turbines and, to date, best practices are not available. Reference [6], treats the influence of the molecular complexity of the working fluid on planar nozzle shapes; the study was carried out with the method of characteristics (MoC) extended to non-ideal flows. Reference [7] documents the development of an automated CFD-based optimization method for radial supersonic stator vane operating with toluene vapour at nominal operating conditions. The work described in Ref. [8] is about the assessment of dense gas effects on the performance of supersonic vanes designed with a simplified method of characteristics for non-ideal flows. In Ref. [9], a method to design supersonic radial vanes for mini-ORC turbines is described. Reference [4], illustrates for the first time a more systematic procedure to design radial supersonic vanes. More recently, in Ref. [10] the authors presented a first study aimed at establishing best design practices for supersonic vanes of high temperature ORC turbines by leveraging on the method described in Ref. [4].

One of the limitations of all the design methods covered in the literature is that they address the fluid dynamic design of the stator by assuming a single turbine operating condition and, as such, disregard the impact that certain design choices may have on part-load operation. Furthermore, these methods are based on the implicit assumption that the diverging part of the supersonic nozzle is symmetric and computed with the MoC. Given that high temperature ORC turbines seldom operate at nominal conditions during actual operation [11], supersonic stators optimally designed for a single operating point suffer from severe fluid dynamic losses [12]. As documented in Ref. [13], an increase of 20% of vane losses could translate in up to 5% of turbine efficiency decay and corresponding power reduction. This finding makes evident the relevance of accounting for off-design conditions during the design phase of these vanes. The performance penalty induced by a symmetric or an asymmetric stator design are, instead, not well comprehended yet.

A commonly adopted design objective when designing supersonic blading is to try to obtain uniform and parallel flows at the outlet of the diverging part of the nozzle and to minimize the nozzle length. References [14, 15] document that symmetric stators can effectively provide parallel flow, but Refs. [16, 17] report similar findings for asymmetric vanes. In summary, the evaluation of the fluid dynamic performance that can be achieved with a supersonic turbine vane design method prescribing either a symmetric or an asymmetric shape, and considering both on- and off-design conditions has not been treated yet and it is of paramount importance especially for high-temperature ORC turbines.

Stemming from this consideration, this chapter documents two conceptually different MoC-based design methods for supersonic stators capable of treating both symmetric and asymmetric nozzle shapes operating with non-ideal compressible flows. Contrary to previously documented supersonic stator design methods, the objective of the novel design methodology considers both on- and off-design performance.

The selected case study is a supersonic vane for an exemplary 200 kW high temperature ORC turbine operating with toluene as working fluid. Steady Reynolds-averaged Navier-Stokes (RANS) simulations of the flow through the stator are used to compute the fluid-dynamic performance. The governing flow equations are solved using the second-order-accurate finite volume solver *SU2* [18, 19], an open-source multiphysics analysis and design optimization software, and fluid thermodynamic properties are calculated with the polytropic Peng-Robinson equation of state model [20]. The performance of the vane configurations is evaluated by computing the entropy-based loss coefficient and the flow uniformity at the stator outlet.

The method to obtain either the asymmetric or the symmetric geometry of the vane is documented in Sec. 2.2. The description of the numerical model and the case study is treated in Sec. 2.3. The results of the study are presented and discussed in Sec. 2.4. Finally, concluding remarks are outlined in Sec. 2.5.

2.2 Methodology

Both the symmetric and asymmetric vane shapes are obtained in two successive steps: the profile of the supersonic diverging section is constructed with the MoC, and then the geometry of the converging part is obtained using NURBS curves. The diverging part is eventually scaled and connected to the converging part to obtain the vane.

2.2.1 Construction of the diverging section

The flow area distribution of the supersonic section of the vane is determined through the MoC adapted to non-ideal gas flows as described in Ref. [4]. The MoC is a method to solve hyperbolic partial differential equations under the assumption of 2D steady homentropic flow and it is widely adopted to determine the optimal shape of the diverging section of supersonic nozzles [21, 22]. This method reduces the governing flow equations to basic relations, commonly referred to as characteristic and compatibility equations. The procedure to derive these two equations can be found in Ref. [4]. These equations are solved starting from the sonic line at the throat until the flow reaches the prescribed boundary conditions. To model the non-ideal flow effects occurring in the expansion of dense organic vapour, the needed thermodynamic property values are calculated with the multi-parameter Equation of State (EoS) model by Lemmon and Span [23] implemented in the open-source *CoolProp* program [24]. An exemplary supersonic nozzle shape obtained with the MoC is displayed in Figure 2.1.

The flow domain in the supersonic nozzle can be divided into three regions, namely, the kernel, the reflex and the uniform flow region. In the kernel region, the flow is accelerated by the successive small pressure difference due to Mach waves originating from the convex wall $m_\text{o} - m_\text{k}$, see Figure 2.1, a circular arc in this study. The kernal region continues until the design condition, prescribed in terms of Mach number (M_a) or outlet

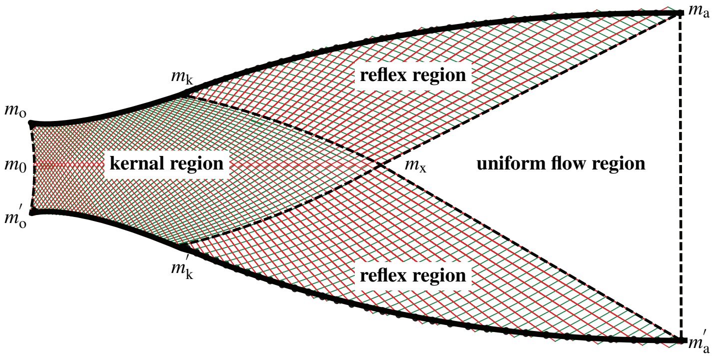

Figure 2.1: Supersonic nozzle section generated using the MoC. The dashed-black lines bound different flow regions while the red and green lines are the positive and the negative characteristics curves. $m_o - m_k$ is the user-defined curve, m_x is the point where the design condition is reached in the kernel region and m_a is the outlet of the nozzle. Figure adapted from Ref. [10].

pressure (p_a), is met at point m_x shown in Figure 2.1. In the reflex region, the concave surface $m_k - m_a$ is designed in such a way that the Mach waves disappear, allowing the flow to reach fully-uniform conditions at section $m_a - m_x - m'_a$, after which the flow enters in the so-called uniform-flow region.

In the following, the surface area enclosed within lines $m_o - m_a$ and $m_0 - m_x$ constitutes the asymmetric nozzle whereas the one comprised within the lines $m_o - m_a$ and its symmetric counterpart $m'_o - m'_a$ represents the symmetric one.

2.2.2 Construction of the vane

The detailed design of the entire vane is obtained by adapting the diverging profile to the axial or radial vane configuration and combining the resulting profile with the converging part of the nozzle. The method for the construction of symmetric stators for radial and axial turbines is reported in Ref. [4] and Ref. [10]. The procedure to construct asymmetric vanes is composed of the steps described in the following.

1. *Scaling.* Asymmetric nozzle profile obtained by MoC is geometrically scaled, such that section ($m_x - m_a$) in Figure 2.1 corresponds to section ($v_{te,x} - v_{te,a}$) in the physical blade domain, see Figure 2.2.

   The scaling factor ($\mathcal{S}$) is determined by obtaining the ratio between the stator pitch ($v_{te,x} - v_{te,a}$), see Figure 2.2, and the line separating the uniform flow region ($m_x - m_a$), see Figure 2.1, from the reflex region. The scaling factor can be mathematically

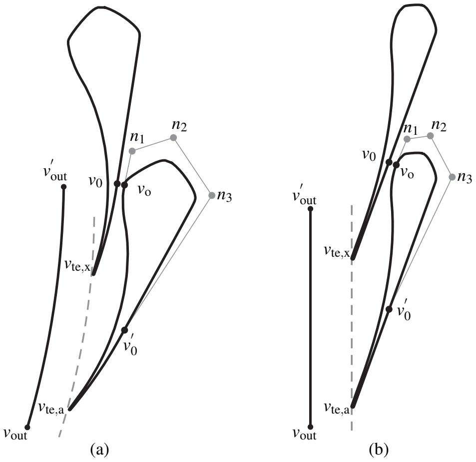

Figure 2.2: Geometric illustration of the asymmetric vanes. Black lines represent the vane profiles and the stator outlet. Grey lines are the lines used for the construction of the vane and are different in case the turbine is (a) radial, or, (b) axial.

written as

$$\mathcal{S} = \frac{l(v_{te,x},\ v_{te,a})}{l(m_x,\ m_a)}, \tag{2.1}$$

where, l denotes the distance between two points. The coordinates x, y of each point of the nozzle profile are then multiplied by the scaling factor.

2. *Transformation of the diverging section.* The scaled nozzle profile is then geometrically transformed such that section $(m_0 - m_x)$ in Figure 2.1 becomes section $(v_0 - v_{te,x})$ of Figure 2.2. In addition, to have the expansion process occur in the entire bladed sections, the last Mach wave leaving the trailing edge of the blade should end at the trailing edge of the adjacent blade. To achieve this, the complementary of the flow angle, i.e., $(90-\phi_a)$, should be approximately equal to the Mach angle corresponding to the design Mach number (M_a). As a result, vanes with only a certain combination of Mach number and flow angles are feasible. To construct the vane geometry, the scaled nozzle obtained from step (1) is rotated by an angle corresponding to the metal outlet angle of the vane (ϕ_a), which is known from the preliminary design of the turbine. For an axial vane configuration, the nozzle centreline remains at a constant angle (ϕ_a), see Figure 2.2(b). For radial vanes, the scaled nozzle from step (1) must be conformally mapped such that the profile of section $(v_0 - v_{te,x})$ becomes a logarithmic spiral [25, 26].

   Designs that do not feature the condition of Mach angle equal to $(90 - \phi_a)$ lead to infeasible designs. For instance, vanes featuring $90 - \phi_a \ll$ Mach angle, would

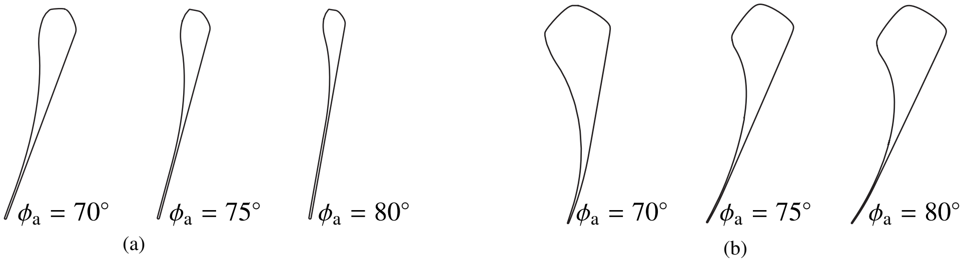

Figure 2.3: Variation of the asymmetric vane geometry with flow angle at a constant design Mach number $M_a = 2.45$, for (a) axial turbines (b) radial turbines.

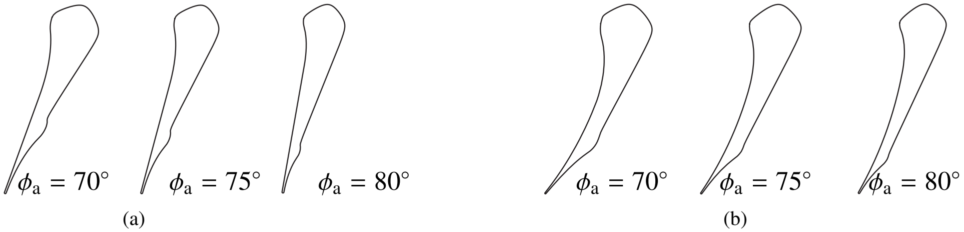

Figure 2.4: Variation of the symmetric vane geometry with flow angle at a constant design Mach number $M_a = 2.45$, for (a) axial turbines, (b) radial turbines.

entail expansion processes prominently occurring in the semi-bladed downstream region. In contrast, designs satisfying the condition $90 - \phi_a \gg$ Mach angle lead to blade shapes with thin trailing edges which may lead to premature structural failure. Figure 2.3 illustrates blade geometries with varying flow angle (ϕ_a) at a constant M_a of 2.45 and shows that the vanes with ϕ_a greater than 70° ($90 - \phi_a \gg$ Mach angle) feature a slender profile. Slender blade geometries featuring a thin aft part do not occur for symmetric vanes and the shape remain feasible over the range of flow angles typical of supersonic turbine stators, as shown in Figure 2.4.

In other words, This condition ensures that the last characteristic originating from the pressure side (from point $v_{\text{te,x}}$) ends close to the trailing edge of the adjacent vane (point $v_{\text{te,a}}$).

3. *Construction of the converging section.* The converging section is constructed by means of a C^2 continuous NURBS curve [27] using the control points $\{v_o, n_1, n_2, n_3, v_o^{'}\}$, where v_o and $v_o^{'}$ are the points on the throat of the same vane corresponding to the adjacent nozzle, see Figure 2.2 and 2.5.

The symmetric vanes are illustrated in Figure 2.5. In these vanes, the profile $v_o - v_a$ corresponds to $m_o - m_a$ (and their symmetric counterpart) shown in Figure 2.1, whereas, the section $v_a - v_{te}$ can be a logarithmic spiral [26] or a straight line depending on whether

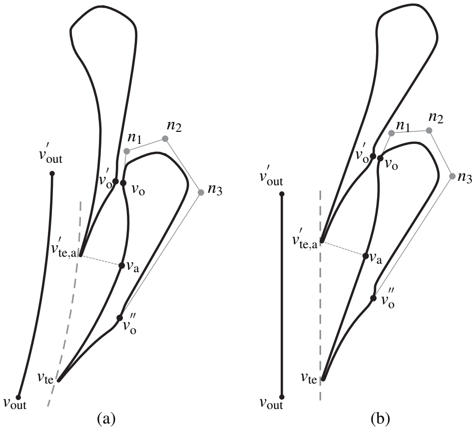

Figure 2.5: Geometric illustration of the symmetric vanes. Black lines represent the vane profiles and the stator outlet. Grey lines are the lines used for the construction of the vane and are different in case the turbine is (a) radial, or, (b) axial.

Table 2.1: Boundary conditions used for the numerical simulations.

Property	Value	Units
Fluid	Toluene	-
$T_{\text{tot,in}}$	587.65	K
$p_{\text{tot,in}}$	3.20	MPa
ϕ_{in}	0.00	°
$I_{\text{tur,in}}$	0.10	-
$\left(\frac{\mu_{\text{tur}}}{\mu_{\text{lam}}}\right)_{\text{in}}$	100.0	-
p_{out}	0.125	MPa

the configuration is radial or axial.

Figure 2.6 illustrates examples of symmetric and asymmetric supersonic blades designed with the proposed method.

2.3 Case study

The vane design method was applied to obtain an axial and a radial stator for an actual 200 kW supersonic turbine of a high temperature ORC power plant [28]. The turbine is the expander of a commercially available ORC genset and it is equipped with supersonic stators designed by means of CFD-based shape optimization [7]. The working fluid is toluene, the vane expansion ratio (total-to-static) is 25.6 at the nominal operating point,

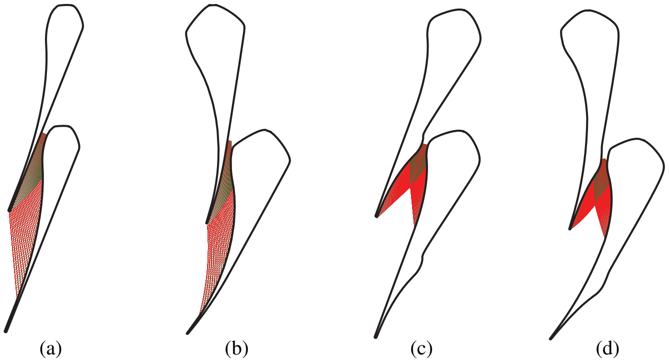

Figure 2.6: Vane geometries and characteristics lines. (a) and (b) are examples of asymmetric vanes and, (c) and (d) are examples of symmetric vanes.

while the imposed outlet camber angle is 70°, according to the current stator design. The boundary conditions and the parameters adopted for the CFD simulation aimed at the estimation of the nozzle fluid dynamic performance are tabulated in Table 2.1.

The computational flow domain was discretized with a hybrid-mesh using an in-house meshing tool [29]. The boundary-layer region close to the vane wall is clustered with quadrilateral elements so as to ensure $y^+ < 1$ and the rest of the flow domain is discretized using triangular elements. The flow domain and its discretization are illustrated in Figure 2.7, where (a) and (b) are symmetric vanes in the axial and radial frame, respectively. Figure 2.7 (c) shows the mesh utilized for the symmetric radial vane.

In order to ensure that the computational results are mesh-independent, a grid convergence study was performed following the method reported in Ref. [30]. The study was conducted on four h_i meshes, where i = 1, 2, 3, 4 denotes the very-coarse, coarse, medium and fine mesh respectively. The four meshes employed for the study comprise of 53 959, 100 263, 151 329 and 205 191 elements. Figure 2.8 illustrates the variation of the entropy-based loss coefficient with the mesh density and a monotonic convergence can be observed. In addition, the entropy-based loss coefficient calculated using the results of the simulation based on the h_3 mesh differs by as much as 1.6% from that obtained with the h_4 mesh. Therefore, meshes with more than 152 000 elements were used in this study.

The open-source computational fluid dynamics (CFD) solver *SU2* [18, 19] was used to carry out RANS flow simulations. The flow equations are complemented by the Spalart-Allmaras one-equation turbulence closure [31]. The laminar viscosity is assumed to be constant and its value is calculated as the algebraic average between the one computed using the total inlet conditions and that obtained by using the outlet thermodynamic state. Fluid thermodynamic properties are obtained by means of the polytropic Peng-Robinson equation of state model [20] implemented in *SU2*. The input fluid properties are: heat capacity ratio γ equal to 1.055, critical temperature T_{crit} equal to 591.75 K and critical pressure equal to p_{crit} 4.13 MPa. The total inlet pressure and temperature are set at the inlet

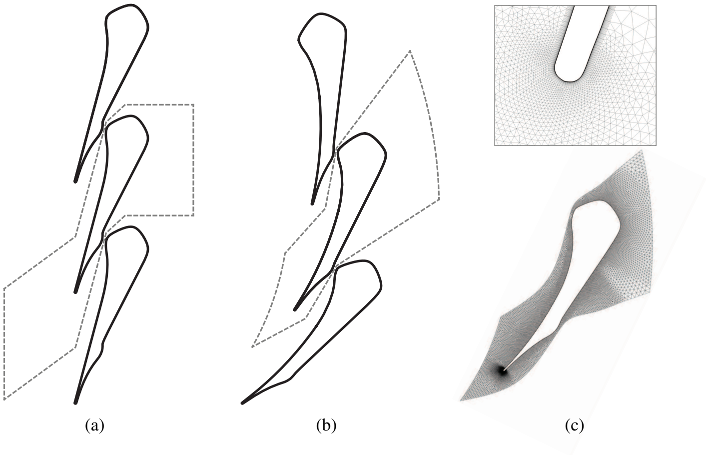

Figure 2.7: Computational flow domain (dashed grey lines) encompassing the vane. (a) axial stator (b) radial stator, (c) an exemplary mesh for a radial vane with a finely discretized trailing edge.

boundary, while a static back-pressure is imposed at the outlet. In addition, non-reflective boundary conditions are ensured at the inlet and outlet boundaries [32]. The integration of the partial differential equations governing the flow problem is performed with an Euler implicit time-marching scheme with CFL=1 and second-order spatial accuracy is ensured by adopting the Roe scheme and MUSCL approach [33]. Residual reduction of six orders of magnitude is attained by running the simulations for a maximum of 10 000 iterations.

2.3.1 Impact of non-ideal flow effects on flow-field and vane design

The inlet conditions in the considered test case are such that non-ideal compressible fluid dynamic (NICFD) effects occur along the expansion process. Figure 2.9(a) shows the isentropic expansion process superimposed to compressibility factor contours in the dimensionless pressure-temperature thermodynamic diagram of the fluid, while Figure 2.9(b) shows Z and γ_{pv} along the isentrope of the supersonic expansion. It can be observed that the thermodynamic process is strongly non-ideal, and the ideal gas conditions, i.e., the conditions for which $\gamma_{pv} = \gamma$ and $Z \approx 1$, are at the outlet of the nozzle. Note furthermore that the averaged γ_{pv} ($\bar{\gamma}_{pv}$), is well below the value of the specific heat capacity ratio of the fluid in the dilute gas limit, i.e., the maximum value of γ_{pv}.

The impact that non-ideal gas conditions have on the vane design can be understood by computing the isentropic pressure distribution or the corresponding flow Mach number,

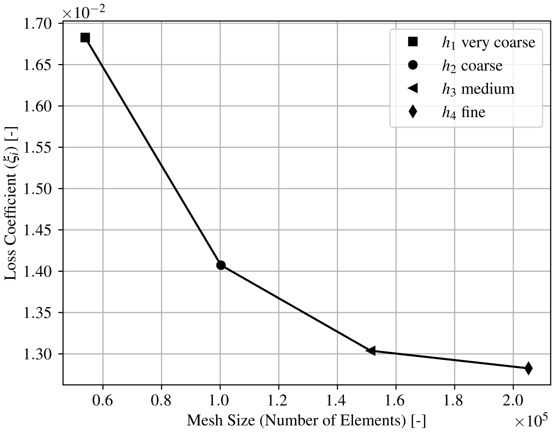

Figure 2.8: Entropy-based loss coefficient vs mesh size for the computational domain shown in Figure 2.7.

and the distribution of the critical area ratio using the following relations [34]

$$\frac{p}{p_{\text{tot}}} = \left[1 + \frac{(\gamma_{pv} - 1)M^2}{2}\right]^{\frac{-\gamma_{pv}}{\gamma_{pv}-1}}, \tag{2.2}$$

$$\frac{A}{A^*} = \frac{1}{M}\left[\frac{2 + (\gamma_{pv} - 1)M^2}{\gamma_{pv} + 1}\right]^{\frac{\gamma_{pv}+1}{2(\gamma_{pv}-1)}}, \tag{2.3}$$

by inspecting the trend of compressibility factor (Z) and of the generalized isentropic exponent (γ_{pv}) [8] along the expansion process.

For a given expansion ratio, the flow Mach number within the nozzle is lower than that occurring for a toluene flow expanding in the dilute gas state. Moreover, the area ratio, i.e., the ratio between the throat area and the area at which the flow reaches a certain Mach number is comparatively larger than the value needed to expand a flow of toluene in the ideal gas state. Figure 2.10 displays the flow properties as a function of the expansion ratio. It can be seen that even for pressure ratios well in excess of 20, the flow Mach number in supersonic ORC vanes whereby $\bar{\gamma}_{pv} < \gamma$ remains well below 2.5. As already known from the literature, the nozzle resulting from the application of the design method is longer and wider if compared with the nozzle that would be obtained by assuming that the fluid obeys the ideal gas law.

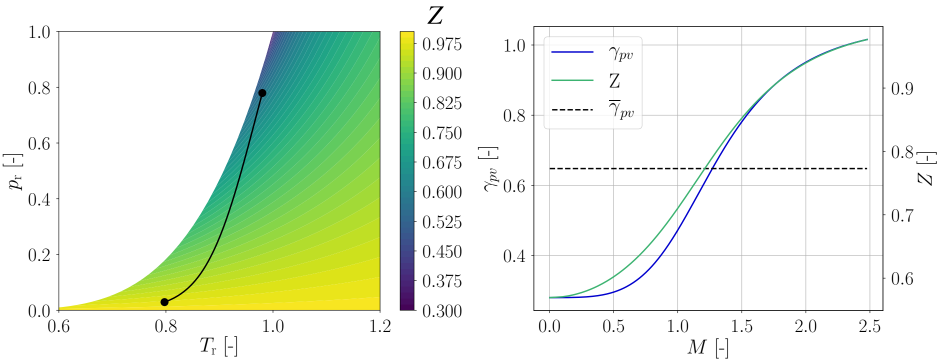

(a) (b)

Figure 2.9: NICFD effects in supersonic nozzle vanes. (a) Illustration of an isentropic expansion process in the $p_r - T_r$ thermodynamic plane displaying also contours of the compressibility factor, (b) Variation of the compressibility factor (Z) and of the generalized isentropic exponent γ_{pv} with Mach number over a supersonic expansion. $\overline{\gamma_{pv}}$ is the average value.

2.4 Results: Fluid dynamic comparison of vanes

The performance of the vanes is estimated by calculating the associated entropy-based loss coefficient ξ and flow uniformity value σ at the outlet boundary. The loss coefficient is defined as

$$\xi = 2 \cdot \frac{\bar{T}_{\text{tot,in}}(\bar{s}_{\text{out}} - \bar{s}_{\text{in}})}{\bar{u}^2_{\text{is,out}}}, \tag{2.4}$$

where, T is the temperature, s is the entropy and u is the flow velocity magnitude and the overbar indicates the quantities obtained by averaging over the mass flow rate. The characterizing quantities of the flow uniformity at the vane exit are the standard deviation of the Mach number and of the flow angle, defined as

$$\sigma = \sqrt{\frac{\sum(X_i - \mu)}{N}}, \tag{2.5}$$

where, X is the local flow quantity at a certain pitch-wise position of the outflow boundary, μ is the algebraic mean of the same flow quantity and N is the number of sampling points.

The performance of the vanes are assessed at their nominal and off-design operating conditions. In this study, the nominal operating conditions correspond to an expansion ratio β equal to 25.6, while the off-design conditions are obtained by varying the nominal static back-pressure.

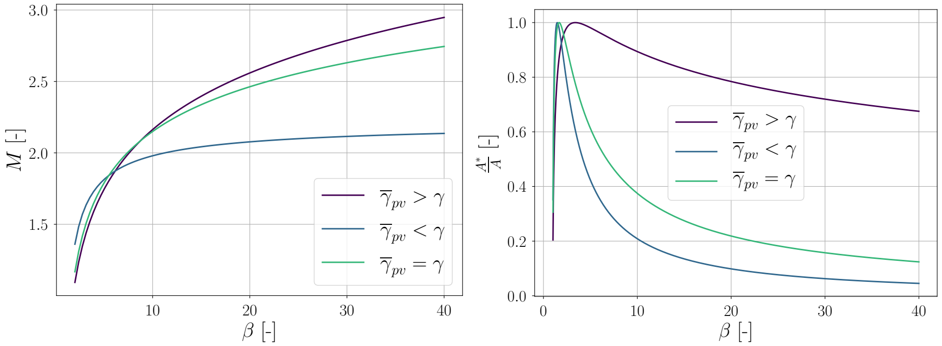

(a) (b)

Figure 2.10: Variation of nozzle flow properties with its expansion ratio. (a) Mach number; (b) area ratio. Values of γ_{pv} are averaged.

Table 2.2: Entropy-based loss coefficients and outlet flow properties for the considered ORC stator vanes. Values are calculated from the results of RANS flow simulations. Information on the boundary conditions and working fluid is reported in Table 2.1.

	axial		radial	
	asymmetric	symmetric	asymmetric	symmetric
ξ	0.0191	0.0182	0.0239	0.0246
M_{out}	2.44	2.43	2.44	2.46
ϕ_{out}	71.1°	70.5°	70.1°	68.6°

2.4.1 Performance at nominal operating condition

2.4.1.1 Axial stator

Table 2.2 shows the entropy loss coefficient ξ, the mass-flow averaged stator outlet Mach number M_{out} and flow angle ϕ_{out} calculated from the results of the simulation for all the considered nozzle geometries. It can be observed that the loss coefficient of the axial asymmetric vane is ~5% higher than that of the symmetric vane. Moreover, the values of M_{out} and ϕ_{out} are similar for all cases ($M_{\text{out}} \sim 2.45$ and $\phi_{\text{out}} \sim 70°$).

Figure 2.11 illustrates the Mach number contours related to the flow around the asymmetric and the symmetric vanes. As expected, for the asymmetric vane the majority of the expansion occurs in the diverging part of the nozzle, i.e., between $v_{\text{o}} - v_0$ and $v_{\text{te,x}} - v_{\text{te,a}}$, as shown in Figure 2.2. In the symmetric vane the expansion occurs between the throat and the nozzle outlet section, i.e., between $v_{\text{o}} - v_{\text{o}}^{'}$ and $v_{\text{te,a}}^{'} - v_{\text{a}}$, as shown in Figure 2.5. The area downstream of the nozzle, i.e., between $v_{\text{te,a}}^{'} - v_{\text{a}}$ and $v_{\text{te,a}}^{'} - v_{\text{te}}$, commonly referred to as semi-bladed region, only guides the flow towards the downstream region. Figure 2.12, displays the density gradient contour of the flow related to the two vane configurations.

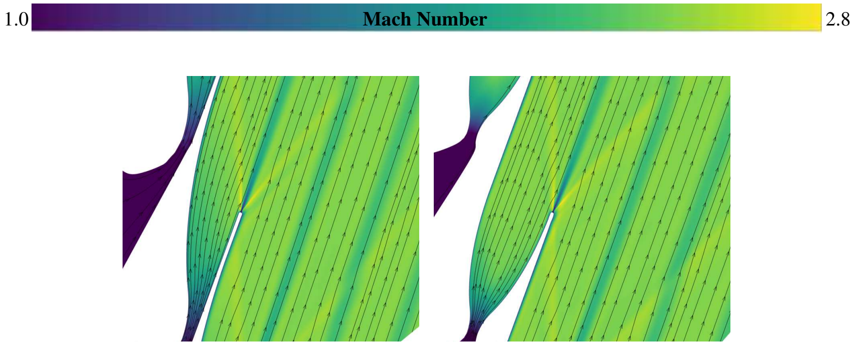

(a) (b)

Figure 2.11: Mach number contour obtained from the simulation of axial vanes with superimposed streamlines. (a) asymmetric vane; (b) symmetric vane.

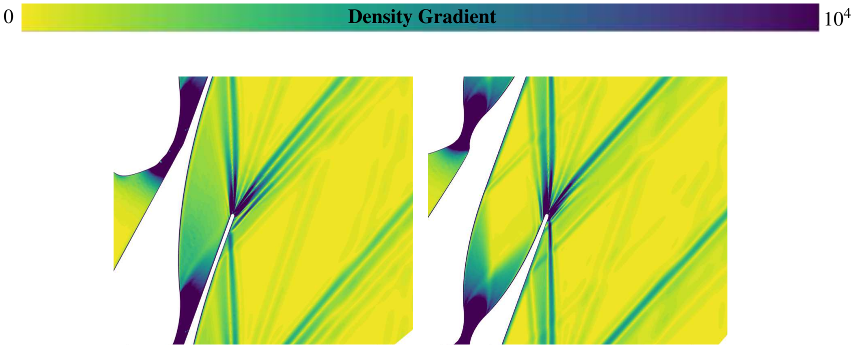

(a) (b)

Figure 2.12: Density gradient contours obtained from the simulation of axial vanes. (a) asymmetric vane; (b) symmetric vane.

No further expansion can be noted in the semi-bladed region. In addition, Figure 2.12 facilitates insights about the most relevant flow features. The fishtail shock system at the trailing-edge assumes a qualitatively different flow pattern. Specifically, the two oblique shock-waves originating at the trailing edge of the asymmetric vane are relatively weaker. This is arguably due to the reduced blockage effect induced by the rear part of the asymmetric vane, which allows the flow to reach the outlet back-pressure with less turning.

Figure 2.13 shows the pitchwise distribution of the Mach number and flow angle at the outflow boundary. Note that the Mach number and flow angle distribution pertaining to the asymmetric vane are more uniform than those pertaining to the symmetric vane. The averaged Mach numbers are approximately similar, while the difference between the mean flow angle is less than 0.5 degrees in the two cases. The slight difference in the outlet flow angle can be attributed to the trailing edge shock-wave pattern. The Mach

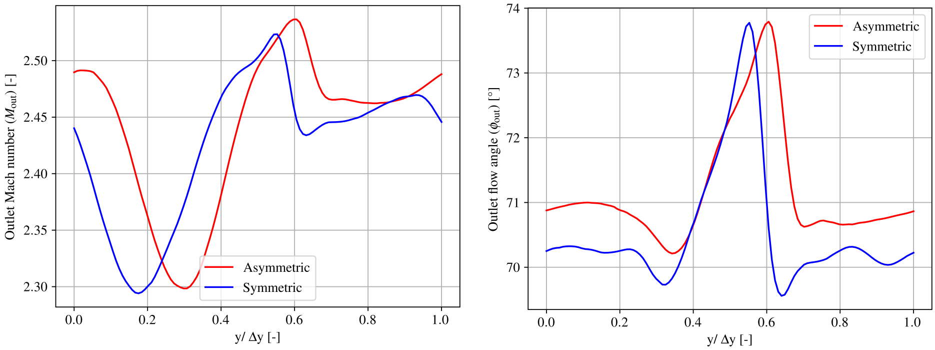

(a)

(b)

Figure 2.13: Flow properties obtained from simulation at the exit of axial stator for asymmetric and symmetric vanes, (a) Mach number (b) flow angle.

number uniformity parameter is 0.06 for both designs, whereas that of the flow angle is 0.8 and 0.9 for the asymmetric and symmetric vane, see Table 2.3. The largest deviation of the local flow quantities from the mean values occur in the wake region, located between $y/\Delta y = 0.0$ and $y/\Delta y = 0.4$ and the trailing edge shock-wave, which can be seen between $y/\Delta y = 0.4$ of 0.4 and $y/\Delta y = 0.6$ in Figure 2.13.

Based on the results obtained for the case study of vanes with $M_{\text{out}} \sim 2.45$ and $\phi_{\text{out}} \sim 70°$, it can be inferred that an asymmetric vane design provides increased flow uniformity at the expense of a slight increase of fluid-dynamic losses.

2.4.1.2 Radial stator

Table 2.2 reports the performance values calculated for the radial vane configurations. The loss coefficient resulting from an asymmetric vane design is ~3% lower than that resulting from a symmetric design. Moreover, the obtained mean values of M_{out} are close to the design Mach number of 2.45 and the flow deviation is ~1.5° for the symmetric design.

Figure 2.14 reports the Mach number contours related to flow around the vanes. Similarly to the case of axial vanes, it can be noted that the expansion process occurs both in the bladed and semi-blade region if the design of the vane is asymmetric, i.e., between $v_{\text{o}} - v_0$ and $v_{\text{te,x}} - v_{\text{te,a}}$ in Figure 2.2, while it occurs mostly in the bladed region if the design is symmetric, namely, between $v_{\text{o}} - v_{\text{o}}^{'}$ and $v_{\text{te,a}} - v_{\text{a}}$, see Figure 2.5. Figure 2.15 shows that a fishtail shock pattern, constituted by both expansion fans and oblique shock-waves, emanates from the trailing-edge of both vanes. Note that the right-side leg of the fishtail shock pattern, namely the shock-wave reflecting onto the blade suction side, features higher intensity if the design is symmetric, in analogy with what was found for the axial

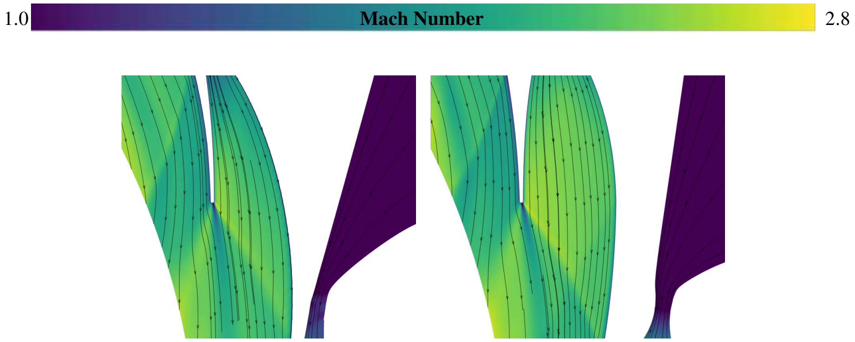

(a) (b)

Figure 2.14: Mach number contour obtained from the simulation of radial vanes with superimposed streamlines, (a) asymmetric (b) symmetric.

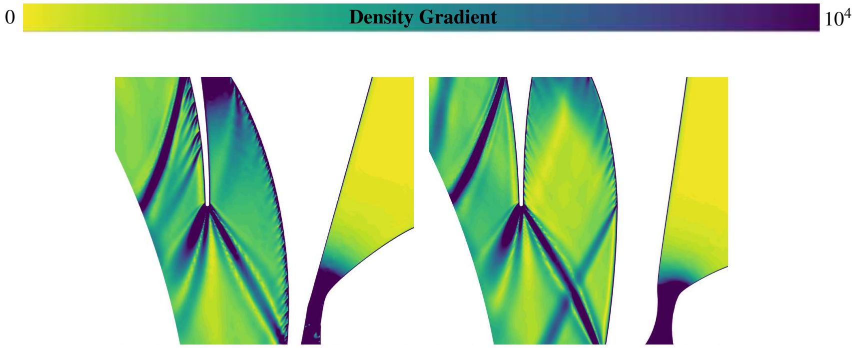

(a) (b)

Figure 2.15: Density gradient contours obtained from the simulation of radial vanes. (a) asymmetric vane; (b) symmetric vane.

case. Furthermore, for the symmetric design, an additional shock-wave originates at the exit of the diverging section, see Figure 2.15(b). This is due to the loss of C^2 continuity at the point connecting the kernel and reflex region, namely at point m_{k} in Figure 2.1. Note that C^2 continuity between the two sections is not guaranteed by the MoC. This additional shock-wave interacts with the one emerging from the trailing edge and reflecting off the suction side, leading to additional fluid-dynamic losses.

Figure 2.16 shows the pitchwise distribution of the Mach number and flow angle at the outflow boundary. Similarly to the axial case, it can be observed that the outlet flow properties are more uniform for the asymmetric vane than they are for symmetric vane. The averaged flow Mach numbers are similar, while the flow deviation angle is about 0.1 for the asymmetric vane and 1.4 degrees for the asymmetric vane, see Table 2.2. The large values of flow deviation angle can be attributed to the stronger shock-wave generated by

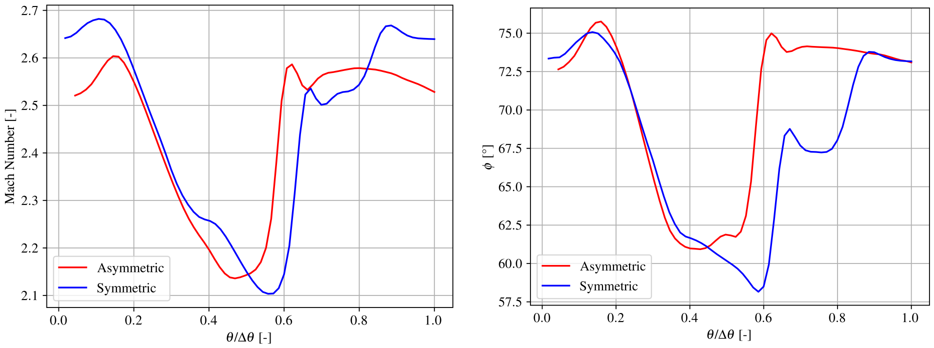

(a) (b)

Figure 2.16: Normalized pitchwise distribution of the flow Mach number (a) and flow angle (b) at the outlet boundary of the symmetric and asymmetric radial vanes.

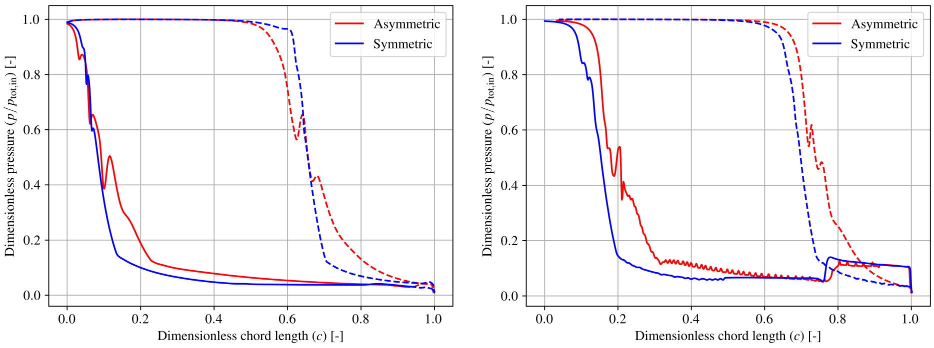

(a) (b)

Figure 2.17: Dimensionless blade loading distribution for symmetric (blue) and asymmetric (red) vanes. (a) axial vane; (b) radial vane. The solid and the dashed lines represent values corresponding to the suction and the pressure side of the vane, respectively.

symmetric vanes. The Mach number uniformity parameters is 0.16 for the asymmetric vane and 0.19 for the symmetric vane, while the flow angle is 5.3 for the asymmetric vane and 5.5 for the symmetric vane, see Table 2.4. In the symmetric case a further instance of flow non-uniformity occur between $\theta/\Delta\theta = 0.7$ and $\theta/\Delta\theta = 0.9$ and it is due to the pressure wave originating at the point where the second-order derivative becomes discontinuous.

Figure 2.17 shows the blade loading for the radial and axial vanes. It can be observed that in both cases the asymmetric design leads to a more gradual pressure reduction on the pressure side of the vane, and oscillations can be observed in the range 0.6<c<0.8. This is due to the pressure waves generated close to the nozzle throat. A Similar feature can be

Table 2.3: Entropy-based loss coefficient and outlet flow quantities obtained from the simulation of axial vane geometries. β_{design} indicates the nominal operating expansion ratio while the other β values refer to off-design conditions. $\beta_{\%}$ refer to a value of the expansion ratio that is different from the design value by the indicated percentage, e.g, $\beta_{-34\%}$ means that the value of β is 34% lower than β_{design}.

$\beta_{\%}$	β	Asymmetry vane					Symmetry vane				
		ξ	M_{out}		ϕ_{out}		ξ	M_{out}		ϕ_{out}	
		-	μ	σ	μ	σ	-	μ	σ	μ	σ
$\beta_{-34\%}$	16.8	0.0275	2.22	0.07	77.2	3.2	0.0214	2.24	0.08	76.0	2.7
$\beta_{-15\%}$	21.8	0.0207	2.35	0.06	74.1	1.5	0.0185	2.35	0.06	72.9	0.9
$\beta_{-8\%}$	23.7	0.0198	2.46	0.05	71.7	0.8	0.0183	2.46	0.04	69.8	0.9
β_{design}	25.6	0.0191	2.44	0.06	71.1	0.8	0.0182	2.43	0.06	70.5	0.9
$\beta_{+8\%}$	27.8	0.0223	2.49	0.05	68.1	0.8	0.0207	2.46	0.04	68.3	0.9

observed on the suction side. The higher loss coefficient resulting from the asymmetric design can be attributed to these surface pressure fluctuations as they may increase the boundary layer losses. Moreover, it can be observed that the simulation of the radial vane predicts a strong shock-wave impinging onto the rear part of the suction side. The presence of a stronger shock-wave in the radial vane can be explained by the reduction in the area distribution due to the decrease in radius. This consequently leads to higher flow turning to accommodate the supersonic expansion process. Such turning can only be achieved by means of a sufficiently strong shock on the blade suction side.

2.4.2 Performance at off-design operating conditions

Off-design operation is simulated by varying the expansion ratio of the vane. In actual ORC turbines, a change of the expansion ratio occurs because of either a variation of the inlet pressure or the static back-pressure. In this study, however, only the static back-pressure is varied so as to attain off-design conditions that can be encountered in supersonic ORC stators [13]. The four investigated off-design conditions are reported in Table 2.3 and 2.4.

2.4.2.1 Axial stator

Table 2.3 reports the entropy-based loss coefficient ξ, the mean μ and the standard deviation σ of the outlet Mach number M_{out} and of outlet flow angle ϕ_{out}. For both axial vane, the fluid dynamic performance is considerably worse at off-design conditions. Moreover, the variation of the loss coefficient as a function of the expansion ratio reported in Figure 2.18(a) highlights that the vane performance characteristic conforms with the expected "bucket shape". However, Figure 2.18(a) also shows that the fluid dynamic performance decay related to the asymmetric vane is considerably larger at $\beta = \beta_{-34\%}$. On the contrary, the variation of the fluid dynamic performance of the symmetric vane is less sensitive to

Table 2.4: Entropy-based loss coefficient and outlet flow quantities obtained from the simulation of radial vane geometries. β_{design} indicates the nominal operating expansion ratio while the other β values refer to off-design conditions. $\beta_{\%}$ refer to a value of the expansion ratio that is different from the design value by the indicated percentage, e.g, $\beta_{-34\%}$ means that the value of β is 34% lower than β_{design}.

$\beta_{\%}$	β	Asymmetry vane					Symmetry vane				
		ξ	M_{out}		ϕ_{out}		ξ	M_{out}		ϕ_{out}	
		-	μ	σ	μ	σ	-	μ	σ	μ	σ
$\beta_{-34\%}$	16.8	0.0289	2.24	0.17	77.0	7.9	0.0243	2.25	0.20	76.0	-
$\beta_{-15\%}$	21.8	0.0230	2.36	0.17	72.8	6.4	0.0233	2.36	0.19	71.4	6.8
$\beta_{-8\%}$	23.7	0.0233	2.40	0.17	71.7	5.9	0.0234	2.39	0.19	70.1	6.4
β_{design}	25.6	0.0239	2.44	0.16	70.1	5.3	0.0246	2.46	0.19	68.6	5.5
$\beta_{+8\%}$	27.8	0.0248	2.47	0.16	69.0	5.0	0.0241	2.46	0.19	67.9	5.5

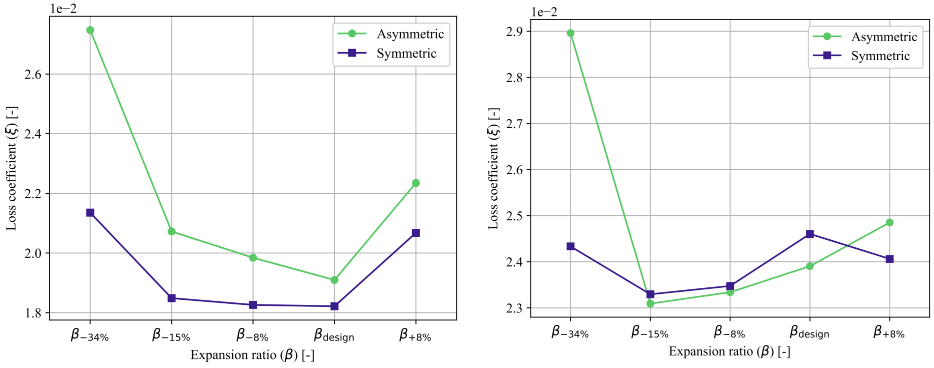

(a)

(b)

Figure 2.18: Loss coefficient as function of expansion ratio, (a) Axial vanes, (b) Radial vanes.

changes of the static back-pressure. This finding suggests that symmetric vanes should be preferred in case supersonic ORC turbines are expected to operate predominantly at part-load.

Figure 2.19(a) shows the variation of the outlet Mach number and of the outlet flow angle as a function of the expansion ratio. Despite the considerable variation of the expansion ratio, the outlet flow Mach number related to both vanes remains within ±10% of the nominal value, while the outlet flow angle increases by 2 to 4 degrees for values lower than the nominal value. Positive flow deviations, i.e, $\phi_{\text{a,nom}} - \phi_{\text{a}}$, can be associated to post-compression effects, while post-expansion effects turn the flow into the axial direction, thus the resulting flow deviation is negative by approximately 2 degrees. Given that the flow deviation has a large impact on rotor performance [13], these results indicate that the optimal design of supersonic vanes should be based on methods capable of

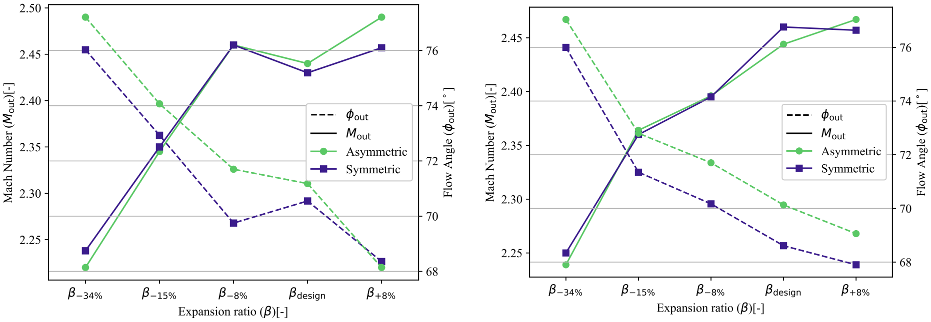

(a) (b)

Figure 2.19: Outlet Mach number and flow angle as function of the expansion ratio, (a) Axial vanes, (b) Radial vanes.

concurrently minimizing the deviation angle and the fluid-dynamic loss over the entire operating envelope.

Figure 2.20 illustrates the density gradient contours obtained from the simulation of the flow around the axial vanes at different operating conditions. It can be observed that the flow features change substantially in the post-expansion region of the vane, namely after the nozzle outlet section. In particular, for β lower than the nominal value, the simulation results show that the flow undergoes a strong re-compression through the shock wave located on the blade suction side. Conversely, a weak fish-tail shock-wave pattern is formed if the vanes operate at an expansion ratio higher than the design value.

2.4.2.2 Radial stator

Table 2.4 reports the performance parameters of the radial vane configurations, while Figure 2.18(b) displays the variation of the loss coefficient as a function of β. Differently from the axial case, the line does not conform with the typical “bucket shape”. In addition, the calculated performance of the two radial vanes is comparable within the range $\beta_{-15\%} < \beta < \beta_{-7\%}$, whereas the loss estimated for the asymmetric vane is considerably larger if β is more than 30% lower than the design value. Conversely, the trends of the outlet flow angle and Mach number illustrated for both vane configurations in Figure 2.19 are similar. These results suggest that a symmetric stator design can be beneficial in terms of efficiency if a high-temperature radial ORC turbine primarily operates at part-load.

Figure 2.21 shows the density gradient contours within the vane flow passage for several values of β. It can be observed that all flow-fields are qualitatively similar, contrary to what was obtained from the axial vane simulations. The main source of loss is the strong shock-wave originating from the trailing-edge and impinging on the rear suction side. Its occurrence, regardless of the value of the expansion ratio, is due to the reduction

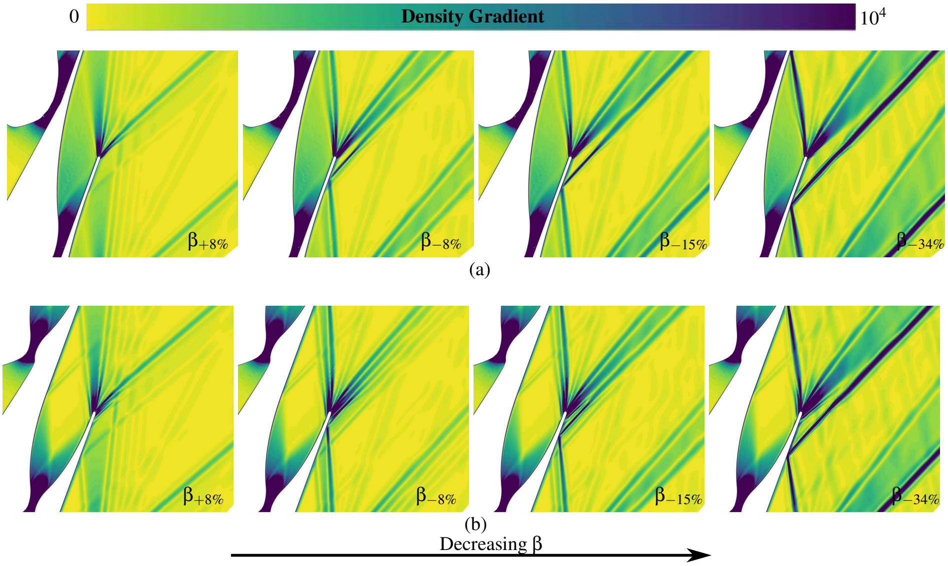

Figure 2.20: Density gradient contours of the flow around the axial vane for decreasing values of β.(a) asymmetric vane; (b) symmetric vane.

of the passage area with the radius. Despite the severe shock-induced flow deceleration, however, the values of the deviation angle of the flow downstream of the radial vanes are in agreement with those obtained for the axial stators, see Figure 2.19.

2.4.3 Preliminary experimental verification of the capability of the design method

The design of the radial supersonic stator vane of the turbine equipping the 200 kW commercial ORC unit is reported in Ref. [35] albeit no information is provided regarding the adopted design method. However, it can be deduced that the stator geometry was obtained by adapting axial nozzles so that they fit into the radial configuration of the turbine assembly, see also Ref. [3]. Simulations show that the flow resulting from this design was characterized by strong shock-waves and highly non-uniform flow at the exit of the nozzle. Once simulations helped identifying this pitfall, the vane was re-designed by means of shape optimization methods based on genetic algorithms as documented in Ref. [7]. Field measurements showed that the performance of the turbine improved by about 10% in terms of turbine power output [7].

A cascade made of symmetric radial vanes whose geometry was designed with the method documented here was manufactured and installed in an operational unit, together with some additional industrial-grade instrumentation, namely pressure and temperature

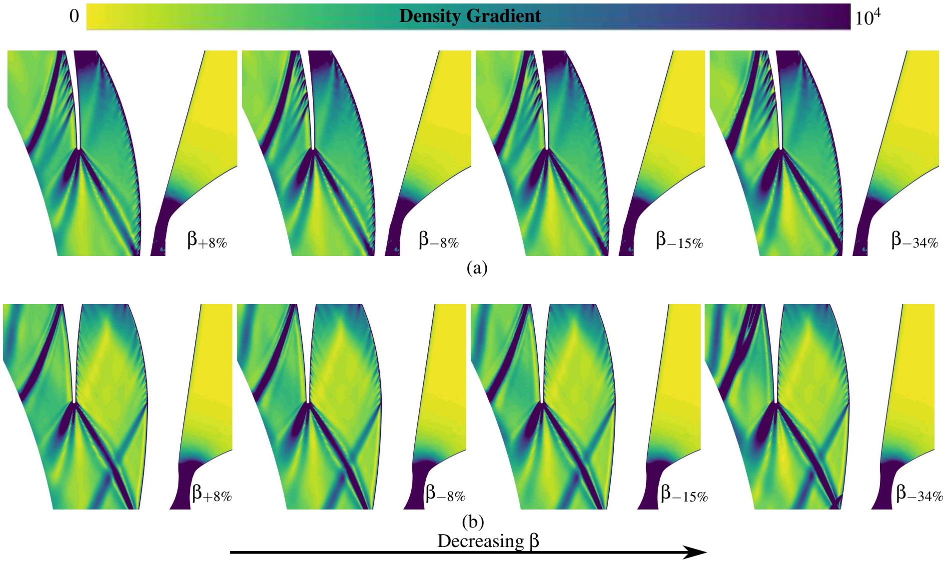

Figure 2.21: Density gradient contours of the flow around the radial vanes for decreasing values of β. (a) asymmetric vane; (b) symmetric vane.

transmitters at the inlet and outlet of the turbine. Data were recorded in the second quarter of 2020. The recordings show that measured power output was again increased by 10% [36] if compared to the previous design [7]. The power increase was attributed to a slight increase in the mass flow rate, to the fluid dynamic performance improvement of the stator, and, consequently, to the related improvement of the rotor performance. More detailed measurements are planned in the future to characterize the stator and rotor performance separately.

2.5 Conclusions

This chapter presents an assessment of the fluid-dynamic performance of asymmetric and symmetric vanes for supersonic high-temperature organic Rankine cycle turbines operating with non-ideal compressible flows. Both axial and radial vane configurations, applicable to ORC turbines ranging from low to high power capacity (few kW to several MW), were considered. The detailed blade design of two vanes was obtained by means of the method of characteristics, extended to arbitrary fluid models coupled to a geometrical transformation method. The exemplary case study regards the design and fluid-dynamic performance evaluation of the supersonic vanes of a 200 kW radial ORC turbine operating with toluene as the working fluid. The asymmetric and symmetric vane performance were characterized by means of CFD simulations at both nominal and off-design conditions in terms of entropy-based loss coefficient and flow uniformity values downstream of the cascade.

Based on the findings resulting from this work, the following conclusions can be drawn.

1. For the same expansion ratio, supersonic radial vanes are affected by higher fluid-dynamic losses than their axial counterparts. This is because the flow-field of radial vanes is characterized by the presence of a strong fishtail shock-wave impinging on the blade suction side at all operating conditions. The formation of the shock-wave is due to the area reduction caused by the radius decrease along the expansion path over the post-expansion region. Conversely, weaker shock-waves occur in axial vanes for operation at and in the proximity of the design point.

2. The vane of axial supersonic ORC turbines should be designed with a symmetric nozzle shape as this type of vane configuration allows to achieve superior fluid-dynamic performance at both on- and off-design conditions. However, the considered asymmetric geometry is affected by C^2 discontinuity. It is possible that the performance of asymmetric vanes is better if the blade profile is C^2 continuous, but this hypothesis has not been tested yet.

3. The value of the entropy-based loss coefficient of symmetric vanes was found to be less sensitive to operating conditions. For example, in the analyzed cases, the flow deviation is within the range ±2° if the expansion ratio β is within ±10% of the nominal value, while it can reach values in excess of $5-6^\circ$ for $\beta = 0.70 \cdot \beta_{\text{design}}$. Comparable values were found for both axial and radial vanes.

4. The symmetric vane design, in case of radial supersonic ORC turbines, leads to a better fluid dynamic performance, however the reduction of the value of the entropy-based coefficient is rather small, especially at operating conditions close to the nominal point. Nevertheless, similarly to the axial case, the asymmetric vane design is significantly less efficient if the vane expansion ratio is 34% lower than its design value. Therefore, a symmetric vane design can be highly advantageous in case the ORC power plant often operates at part-load conditions, like mini-ORC systems for mobile application or distributed thermal energy harvesting.

5. Preliminary measurements of the power output of a commercial ORC power plant whose turbine stator was selected as the test case for the investigation documented here show that the power output increased by approximately 10% once the symmetric stator geometry designed with the method illustrated in this article was installed. The previous stator geometry was obtained by means of automated shape optimization using a genetic algorithm. It can therefore be argued that a much simpler approach relying on the method of characteristics coupled with appropriate geometrical transformations, and on the result of this work that a symmetric vane is preferable, leads to better performance.

The outcomes of the study make evident that, even in the case of symmetric vanes, the large variation of the outlet flow angle at off-design condition remains of great concern, particularly for the efficient operation of the rotor. The optimal design of supersonic vanes of ORC turbines should then necessarily target also the minimization of such variation along with the reduction of entropy generation.

It can therefore be argued that the best performance of supersonic ORC turbines over the entire operational range can be obtained by first designing the stator according to the method documented here and the rotor according to an appropriate design method (e.g, the method of waves if the rotor is supersonic), and then by performing multi-point multi-objective optimization of the entire turbine (coupled stator and rotor). The development of a multi-point multi-objective optimization framework based on the adjoint method is ongoing and the assessment of its potential for the problem at hand is the goal of future work.

Nomenclature

Symbols

c	dimensionless chord length
C	continuity
h	mesh
I	turbulence intensity
l	length
M	Mach number
m	geometrical vertices used in MoC
n	NURBS control points
p	pressure
T	temperature
$\mathcal{S}$	scaling factor
s	entropy
u	velocity
v	geometrical vertices used in vane
y^+	y plus
x, y	Cartesian coordinates
Z	compressibility factor

Greek letters

β	pressure ratio
Δ	change in quantities
γ_{pv}	isentropic pressure volume exponent
μ	viscosity/mean
ϕ	flow angle
σ	standard deviation

θ	azimuthal angle
ξ	entropy generation coefficient

Subscripts

0	throat centre
1..3	NURBs control point index
a	nozzle outlet
crit	critical
design	design
i	index
in	vane inlet
is	isentropic
k	kernal
lam	laminar
o	throat
out	vane outlet
r	non-dimensional by critical quantities
te	trailing edge
tot	total conditions
tur	turbulence
x	end of kernal region

Accents

$\bar{.}$	mass average
$.'$	symmetric equivalent

References

[1] Colonna, P., Casati, E., Trapp, C., Mathijssen, T., Larjola, J., Turunen-Saaresti, T., and Uusitalo, A., 2015. "Organic Rankine Cycle Power Systems: From the Concept to Current Technology, Applications, and an Outlook to the Future". *Journal of Engineering for Gas Turbines and Power,* **137**(10), p. 100801 (19 pages).

[2] Colonna, P., Harinck, J., Rebay, S., and Guardone, A., 2008. "Real-gas effects in organic Rankine cycle turbine nozzles". *Journal of Propulsion and Power,* **24**(2), pp. 282–294.

[3] Rinaldi, E., Pecnik, R., and Colonna, P., 2016. "Unsteady operation of a highly Supersonic ORC Turbine". *Journal of Turbomachinery,* **138**(12), p. 121010 (9 pages).

[4] Anand, N., Vitale, S., Pini, M., Otero-Rodríguez, G. J., and Pecnik, R., 2018. "Design methodology for supersonic radial vanes operating in non-ideal flow conditions". *Journal of Engineering for Gas Turbines and Power,* **141**(2), p. 022601 (9 pages).

[5] Bahamonde, S., Servi, C. D., and Colonna, P., 2020. "Hybrid electric powertrain for long-haul trucks and buses: Preliminary analysis of a new concept based on a combined cycle power plant.". *Global Power and Propulsion Society Journal,* **4**, pp. 63–79.

[6] Guardone, A., Spinelli, A., and Dossena, V., 2013. "Influence of molecular complexity on nozzle design for an organic vapor wind tunnel". *Journal of Engineering for Gas Turbines and Power,* **135**(4), p. 042307.

[7] Pasquale, D., Ghidoni, A., and Rebay, S., 2013. "Shape Optimization of an Organic Rankine Cycle Radial Turbine Nozzle". *Journal of Engineering for Gas Turbines and Power,* **135**(4), p. 042308 (13 pages).

[8] Wheeler, A. P. S., and Ong, J., 2013. "The role of dense gas dynamics on ORC Turbine performance". *Journal of Engineering for Gas Turbines and Power,* **135**(8), p. 082604 (9 pages).

[9] Uusitalo, A., Turunen-Saaresti, T., Gourdane, A., and Grönman, A., 2014. "Design and flow analysis of a supersonic small scale orc turbine stator with high molecular complexity working fluid.". *ASME TurboExpo: Turbine Technical Conference and Exposition, Düsseldorf, Germany*(GT2014-26204), pp. 1–11.

[10] Anand, N., Colonna, P., and Pini, M., 2020. "Design guidelines for supersonic stators operating with fluids made of complex molecules". *Energy,* **203**, July, p. 117698 (9 pages).

[11] Casella, F., Mathijssen, T., Colonna, P., and van Buijtenen, J., 2013. "Dynamic Modeling of Organic Rankine Cycle Power Systems". *Journal of Engineering for Gas Turbines and Power,* **135**(4), 03, p. 042310 (12 pages).

[12] Pini, M., Persico, G., and Dossena, V., 2014. “Robust adjoint-based shape optimization of supersonic turbomachinery cascades”. In Proceeding of ASME TurboExpo, no. GT2014-27064, ASME, pp. 1–13.

[13] De Servi, C. M., Burigana, M., Pini, M., and Colonna, P., 2019. “Design Method and Performance Prediction for Radial-Inflow Turbines of High-Temperature Mini-Organic Rankine Cycle Power Systems”. *Journal of Engineering for Gas Turbines and Power,* **141**(9), p. 091021 (12 pages).

[14] Goldman, L. J., and Scullin, V. J., 1968. Analytical Investigation of Supersonic Turbo-machinery Blading, I - Computer Program for blading Design. Tech. Rep. NASA TN D-4421, NASA, Washington DC.

[15] Goldman, L. J., 1968. Analytical Investigation of Supersonic Turbo-machinery Blading, II - Analysis of Impulse Turbine-Blade Sections. Tech. Rep. NASA TN D-4422, NASA, Washington DC.

[16] Dorney, D. J., Huber, F. W., and Sondak, D. L., 2003. “Odd-design performance of a multi-stage supersonic turbine”. In Proceedings of 41th Aerospace Science Meeting & Exhibit, no. AIAA 2003-1212.

[17] Angelino, G., DeLuca, L., and William, S., 1991. *Modern research topics in aerospace propulsion - In honor of Corrado Casci*. Springer-Verlag New York Inc., January.

[18] Economon, D. T., Palacios, F., Copeland, S. R., Lukaczyk, T. W., and Alonso, J. J., 2015. “SU2: An open-source suite for multiphysics simulation and design.”. *AIAA Journal,* **54**(3), pp. 828–846.

[19] Vitale, S., Albring, T. A., Pini, M., Gauger, N. R., and Colonna, P., 2017. “Fully turbulent discrete adjoint solver for non-ideal compressible flow applications”. *Journal of the Global Power and Propulsion Society,* **1**, pp. 252–270.

[20] Peng, D.-Y., and Robinson., D. B., 1976. “A new two-constant equation of state”. *Industrial and Engineering Chemistry Fundamentals,* **15**(1), pp. 59–64.

[21] Zucrow, M. J., and Hoffman, J. D., 1976. *Gas Dynamics Volume 1*, Vol. 1. John Wiley & Sons.

[22] Zucrow, M. J., and Hoffman, J. D., 1977. *Gas Dynamics Volume 2: Multidimensional Flow*, Vol. 2. John Wiley & Sons.

[23] Lemmon, E., and Span, R. “Short fundamental equations of state for 20 industrial fluids”. *Journal of Chemical and Engineering Data,* **51**, pp. 785–850.

[24] Bell, I. H., Wronski, J., Quoilin, S., and Lemort, V., 2014. “Pure and pseudo-pure fluid thermophysical property evaluation and the open-source thermophysical property library coolprop”. *Industrial & Engineering Chemistry Research,* **53**(6), pp. 2498–2508.

[25] Whitfield, A., and Baines, N. C., 1990. *Design of Radial Turbo-machines*. Longman Scientific & Technical.

[26] Archibald, R. C., 1918. “The Logarithmic Spiral”. *The American Mathematical Monthly,* **25**(4), pp. 189–193.

[27] Piegl, L., and Tiller, W., 1997. “The NURBS Book”. *Springer*.

[28] Harinck, J., Pasquale, D., Pecnik, R., van Buijtenen, J., and Colonna, P., 2013. “Performance improvement of a radial organic Rankine cycle turbine by means of automated computational fluid dynamic design”. *Proceedings of the Institution of Mechanical Engineers, Part A: Journal of Power and Energy,* **227**(6), pp. 637–645.

[29] Ghidoni, A., Pelizzari, E., Rebay, S., and Selmin, V., 2006. “3d anisotropic unstructured grid generation”. *International Journal for Numerical Methods in Fluids,* **51**, pp. 1097–1115.

[30] Various Authors, 2009. “Standard for Verification and Validation in Computational Fluid Dynamics and Heat Transfer”. *ASME V&V 20*, pp. 1–100.

[31] Spalart, P. R., and Allmaras, S. R., 1992. “A one-equation turbulence model for aerodynamic flows”. *AIAA Journal,* **1**, pp. 5–21.

[32] Giles, M. B., 1990. “Nonreflecting boundary condition for euler equation calculation”. *AIAA Journal,* **28**(12), pp. 2050–2058.

[33] Roe, P. L., 1981. “Approximate riemann solvers, parameter vectors, and difference schemes.”. *Journal of Computational Physics,* **43**, pp. 357–372.

[34] Baltadjiev, N. D., Lettieri, C., and Spakovszky, Z. S., 2015. “An investigation of real gas effects in supercritical co2 centrifugal compressors.”. *Journal of Turbomachinery,* **137**(9), p. 091003 (13 pages).

[35] Hoffren, J., Talonpoika, T., Larjola, J., and Siikonen, T., 2002. “Numerical simulation of real-gas flow in a supersonic turbine nozzle ring,”. *Journal of Engineering in Gas Turbines and Power,* **124**(2), April, pp. 395–403.

[36] Anand, N., and Eppinga, Q., 2020. “Personal communication”. *at premises of Triogen*, September.

3

Design guidelines for supersonic vanes operating with fluids made of complex molecules

The contents of this chapter appeared in:

N. Anand, P. Colonna and M. Pini. 2020.
Design guidelines for supersonic stators operating with fluids made of complex molecules.
Energy, **203**, p. 117698 (9 pages).

© Elsevier 2020 - Reprinted with permission

Abstract *Supersonic stator vanes account for two-thirds of the fluid-dynamic losses in high temperature mini-organic Rankine cycle (ORC) turbines. As a result, the overall performance of the turbo-expander mainly depends on the design of the stator. Currently, there is no established correlation for the optimal design of such cascades. This chapter concerns an investigation about the accuracy of the only design rule currently available for the design of supersonic stators operating with fluids made of complex molecules. A physics-based analytical model and a CFD-based model were developed to estimate the optimal post-expansion ratio and to compare their results with the Deych's model. The analysis shows that the Deych's method fails to accurately predict the optimum value of the post-expansion ratio. The study covers also the assessment of the optimum post-expansion ratio in relation to the solidity, the design flow angle and the total-to-static expansion ratio. The outcome demonstrates that there exists a unique optimum post-expansion ratio for a set of primary stator design parameters. In summary, vanes operating with a substance made of complex molecule as the working fluid, which is typical of high-temperature ORC turbines, feature a unique theoretical value of the optimum post-expansion ratio for a given total-to-static expansion ratio. New correlations are required to predict this value.*

3.1 Introduction

The high-expansion ratio is a defining feature of unconventional turbomachinery, i.e., turbomachinery operating with non-conventional working fluids like those treated for example in Ref. [1, 2]. Given that such working fluids are made of complex organic molecules for which the speed of sound is quite low, the stator often operates at highly supersonic flow conditions [3, 4]. As a result, new and ad hoc fluid dynamic design methods have been developed in recent times.

ORC power systems are becoming increasingly relevant because they can efficiently convert thermal energy from renewable and waste heat sources [3]. Regardless of its extremely wide application range, the full potential of ORC technology is not realized yet. Economic viability will increase if current technical challenges affecting system performance versus cost are overcome. One issue affecting turbine design and performance of high-temperature high-expansion ratio machine is the complex and non-ideal fluid dynamics within the stator [5]. It has been recently shown, see Ref. [6], that the fluid dynamic losses occurring in the stator of an existing high-temperature high-expansion ratio ORC turbine amount to approximately two-thirds of the total losses of the turbine. This is the case in such type of small-capacity turbines, which are always highly loaded in order to limit the number of stages to unity because of economic constraints. Therefore, the design of efficient stator cascades is critical.

The preliminary design of supersonic stationary vanes involves the choice of several parameters, e.g., the flow angle (ϕ_a), the expansion ratio (β_{t1}), the degree of divergence (DoD), the solidity (σ) etc., based on correlations. The blade profile is then obtained with the Method of Characteristics (MoC) and refined by means of computational fluid dynamics (CFD) simulations [1]. The mechanical verification of the fluid dynamic design completes the design iteration. Recent studies already dealt with the detailed fluid dynamic design of ORC stators [7, 8]. However, the optimal choice of preliminary design parameters dictating the subsequent detailed fluid dynamic design phase has not been treated in the literature yet. Currently, therefore, correlations which were developed to obtain preliminary design parameters for conventional gas turbines are adopted, and the optimal design of supersonic ORC blades can only be obtained by resorting to computationally expensive numerical optimization based on high-fidelity CFD, and starting from highly suboptimal configurations.

The degree of divergence is the preliminary design parameter that has the largest impact on the resulting fluid dynamic performance of supersonic ORC vanes [8]. To the authors' knowledge, the only model that can be currently employed to calculate the optimal degree of divergence is the one proposed by Deych [9]. This model provides an estimate of the optimum degree of nozzle divergence (DoD) as a function of the stator exit Mach number. The model was derived for the case of supersonic axial cascades operating with air as working fluid, therefore its application to the design of ORC stators affected by non-ideal compressible flow effects is arguably unjustifiable from a theoretical point of view. The objectives of the study documented in this chapter are (i) to discuss the accuracy and limitations of the Deych's model, henceforth referred to as *empirical method*, if applied to nozzles operating with fluids different than air, and (ii) to assess the variability of the optimal post-expansion ratio with respect to primary design variables, namely, the flow metal angle, the solidity and the expansion ratio.

To achieve these goals, a physics-based and a CFD-based loss estimation models, limited to perfect gas flows, were developed and these are referred to as *analytical method* and *CFD-based method* in the following. The analytical method estimates the boundary-layer and mixing losses for a typical supersonic axial vane configuration. The losses in the boundary-layer are evaluated according to the procedure described in Ref. [10]. The mixing loss is evaluated by applying the mass, momentum and energy conservation equations to the semi-bladed region of the stator vane, as explained in Ref. [11]. The CFD-based method comprises of a detail design procedure and a simulation. The vane geometry generation method is adapted to handle axial configurations from the method described in Ref. [8]. The fluid-dynamic performance of the blades is calculated using the open-source Reynolds averaged Navier Stokes (RANS) solver SU2 [12]. The flow equations are complemented by the one-equation Spalart-Allmaras turbulence model [13].

In order to investigate the accuracy of the empirical model, the optimum DoD (or alternatively, the optimum post-expansion ratio) obtained from this model is compared to the values calculated with the numerical and the analytical methods. Additionally, the analysis is extended to consider working fluids ranging from those made of simple molecules, to those made of complex organic molecules in order to study the effect of the fluid molecular complexity on the optimum post-expansion ratio. The variation of the optimum post-expansion ratio with the primary design variables is assessed by scanning the design space with the CFD-based method.

3.2 Methodology

The flow domain of a typical axial stator vane can be divided into three sections, see Figure 3.1(a): the converging section between station (t) and (o), the diverging section between station (o) and (a) and the semi-bladed section between station (a) and (1). The assessment of the empirical method is based on the comparison of the optimal DoD calculated with the empirical method with those obtained with the analytical and the CFD-based methods.

3.2.1 Empirical method

In 1965, Deych illustrated a method to estimate the preliminary DoD for a stator vane operating in transonic/supersonic flow conditions [9]. To date, this is the only method available and adopted in common practice. According to this method, the optimum DoD is defined by the relation

$$\mathrm{DoD}_{\mathrm{empirical}} = \frac{A_\mathrm{a}}{A_\mathrm{o}} = \begin{cases} 1, & \text{for } M_1 \leq 1.4, \\ 1 + (0.5\ M_1 - 0.4)\left[\dfrac{1}{\mathcal{A}_\mathrm{is}(M_1,\gamma)} - 1\right], & \text{for } M_1 > 1.4, \end{cases} \tag{3.1}$$

where M_1 is the stator design Mach number, A_o is nozzle throat width, A_a is nozzle outlet width, $\mathcal{A}_\mathrm{is}$ is the area ratio corresponding to an isentropic expansion and γ is the heat capacity ratio. The current design practice is thus that nozzles for which the design M_1 is lower than 1.4 (transonic) are made without the diverging section, because the semi-bladed section provides the flow with a sufficient degree of expansion without an excessive penalty in terms of efficiency. In contrast, supersonic nozzles ($M_1 > 1.4$) are always designed with a diverging section.

3.2.2 Analytical method

Two of the major dissipation mechanisms in supersonic axial vanes are due to mixing and viscosity in the boundary layer. The procedure to analytically estimate these losses is as follows:

(a) Mixing losses. The amount of kinetic energy that is dissipated due to mixing is estimated, as described in Ref. [11], by solving the mass, momentum and energy conservation equations in the control volume encompassing the semi-bladed section of the vane, see Figure 3.1(a). The flow deviation angle is

$$\Delta\phi = \tan^{-1}\left[\frac{\frac{\gamma}{1-\gamma}\beta_{1\mathrm{a}}\tan\phi_{\mathrm{a}} \pm \sqrt{(1-\beta_{1\mathrm{a}})\left(\frac{2\gamma}{\gamma-1}M_{\mathrm{a}}^2 - 1 - \frac{\gamma+2}{\gamma-1}\beta_{1\mathrm{a}}\right) + \left(\frac{\gamma\beta_{1\mathrm{a}}}{\gamma-1}\tan\phi_{\mathrm{a}}\right)^2}}{1+\gamma M_a^2 - \beta_{1\mathrm{a}}}\right], \tag{3.2}$$

where, M_{a} is the nozzle Mach number, ϕ_{a} is the design flow angle and $\beta_{1\mathrm{a}}^{-1} \equiv \beta_{\mathrm{a}1}$ is the post-expansion ratio. The only independent quantity in Eqn. (3.2) is $\beta_{1\mathrm{a}}$ which allows to evaluate M_1 at the exit of the vane. Thus, the amount of kinetic energy that is dissipated due to mixing can be estimated as

$$\xi_{\mathrm{mix}} = \frac{h_1 - h_{\mathrm{is},1}}{h_{\mathrm{is},1}}, \tag{3.3}$$

where, h is enthalpy, and subscript "is" stands for isentropic.

(b) Boundary layer losses. These losses are due to viscous dissipation within the nozzle boundary layer. Assuming turbulent flow on the blade surface, the kinetic energy dissipation can be calculated as

$$\xi_{\mathrm{bl}}\big|_0^X = \frac{\Delta h_{\mathrm{bl}}\big|_0^X}{h_{\mathrm{is},1}}, \tag{3.4}$$

where,

$$\Delta h_{\mathrm{bl}}\big|_0^X = T_1\dot{S} = T_1\frac{C_{\mathrm{d}}\,\rho_{\mathrm{t}}}{T_{\mathrm{t}}}\int_0^X \frac{\rho_{x\mathrm{t}}(M_x)}{T_{x\mathrm{t}}(M_x)}M_x^3 c_{x\mathrm{t}}^3\,dx \tag{3.5}$$

and

$$h_{\mathrm{is},1} = 0.5\cdot\dot{m}v_{\mathrm{is},1}^2. \tag{3.6}$$

In these equations, C_{d} is the dissipation coefficient, ρ is the density, T is the temperature, S is the entropy, $\dot{m}$ is the mass flow rate, v is the velocity, c is the speed of sound and subscript "xt" stands for isentropic ratio between properties at station "x" and "t". C_{d} is equal to 0.002 according to Ref. [10].

The only unknown in Eqn. (3.5) is the property distribution along the surface of the stator, for which the quasi-1D flow approximation is assumed valid. Since the boundary layer losses in the subsonic section are significantly lower than the boundary layer losses in the supersonic section (as boundary layer losses scale with the cube of the Mach number), only the diverging part of the nozzle and the semi-bladed section are modeled for simplicity. In the diverging section of the nozzle the flow accelerates, while in the

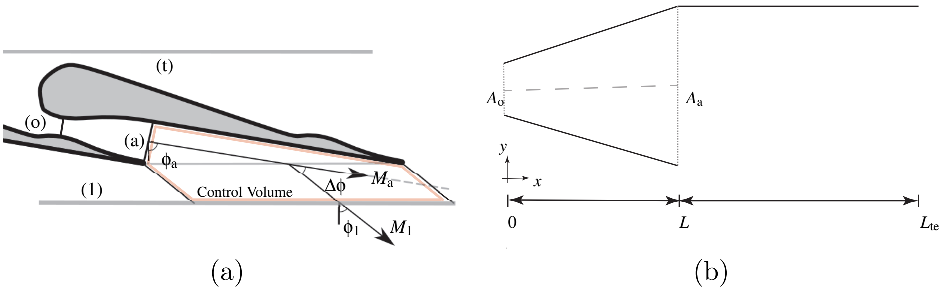

(a) (b)

Figure 3.1: Schematics of the nozzle geometries related to the analytical loss models: (a) geometry for the mixing loss model, showing Mach number, deviation angle and the different stations in the supersonic vane. The control volume is outlined in red. (b) illustration of the domain considered for the computation of the boundary layer losses.

semi-bladed section the linear suction side surface guides the flow to the outlet, see Figure 3.1(a). The Mach number distribution is computed according to the 1D flow approximation by assuming a linear variation from unity at the throat to M_a at the nozzle outlet section, see Figure 3.1(b). The suction side is modeled as a flat plate over which the fluid flows at constant Mach number M_a, see Figure 3.1(b). Eqn. (3.5) applied to the geometry depicted in Figure 3.1(b) allows to compute the boundary layer loss in the supersonic vane as

$$\xi_{bl} = 2\xi_{bl}|_0^L + \xi_{bl}|_L^{L_{te}}, \tag{3.7}$$

where, $\xi_{bl}|_0^L$ is the loss due to the nozzle surface and $\xi_{bl}|_L^{L_{te}}$ is the loss due to the linear suction side.

3.2.3 CFD-based method

The vane geometries with varying DoD are generated and analyzed by following a procedure which can be divided into two parts, namely, *geometry generation* and *CFD simulation*. The procedure is similar to that documented in Ref. [8] for radial vanes, however, it differs regarding the way the axial vane geometry is obtained.

3.2.3.1 Geometry Generation.

In order to design an axial supersonic stator, the nozzle geometry obtained by applying the MoC [14, 15] is adapted to the vane configuration and the geometry of the converging section is generated by means of Non-Uniform Rational Basis Splines (NURBs) [16]. Details of this MoC are provided also in Ref. [8], while the procedure to create the vane geometry starting from the nozzle obtained with the MoC is as follows.

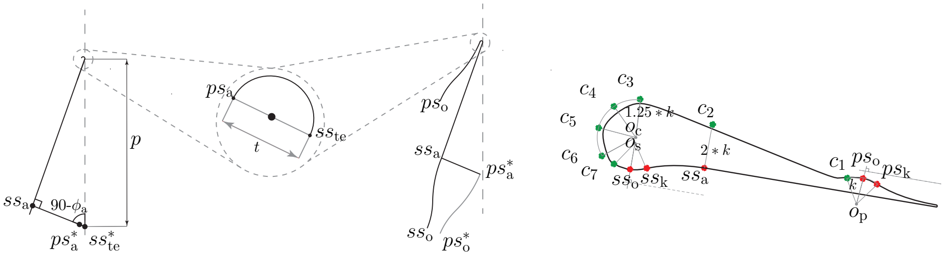

(a) (b) (c) (d)

Figure 3.2: Schematic representation of the graphic procedure to obtain the geometry of an axial supersonic vane. (a) semi-bladed region; (b) trailing edge; (c) diverging-nozzle section; (d) converging section.

1. *Scaling factor.* With reference to Figure 3.2, two points ss_{te} and ss_{te}^*, which are a pitch-distance (p) apart, are placed on the plane where the trailing edge of the stator is to end. Next, point ss_a is obtained by the intersecting the line originating from point ss_{te} at design flow angle ϕ_a and the line originating from ss_{te}^* at an angle $90° - \phi_a$. The line ss_a-ss_{te}, see Figure 3.2(a) can then be readily drawn. Point ps_a^* is positioned at a distance equal to the prescribed trailing edge thickness (t) from point ss_{te}^* along the line ss_{te}^*-ss_a.

   The diverging-nozzle geometry resulting from the application of the MoC is scaled such that the non dimensional width of the throat is unity, thus determining the value of the exit area of the diverging-nozzle $\mathcal{A}_{is}$ as a function of M_a. In order to complete the construction of the diverging part of the nozzle, the outlet cross-section width calculated with the MoC must be made the same as ss_a-ps_a^*, see Figure 3.2(c). This is accomplished by means of a scaling factor $\mathcal{S}$ determined by calculating the ratio of the distance between points ss_a and ps_a^* and $\mathcal{A}_{is}$, namely as

$$\mathcal{S} = \frac{l(ss_a, ps_a^*)}{\mathcal{A}_{is}(M_a)}, \tag{3.8}$$

   where, l is the length between ss_a and ps_a^*.

2. *Transformation of the nozzle geometry.* After the nozzle geometry obtained with the MoC is scaled to the factor $\mathcal{S}$, the scaled nozzle is then rotated by an angle ϕ_a about the center of the throat. The obtained geometry forms therefore the diverging section of the supersonic vane, see Figure 3.2(c).

3. *Translation of the pressure side (line ps^*).* In order to obtain a complete blade, thus a continuous line made of the pressure and of the suction side, the pressure side of the nozzle, section ps^* in Figure 3.2(c), is translated by a pitch-length to obtain curve ps.

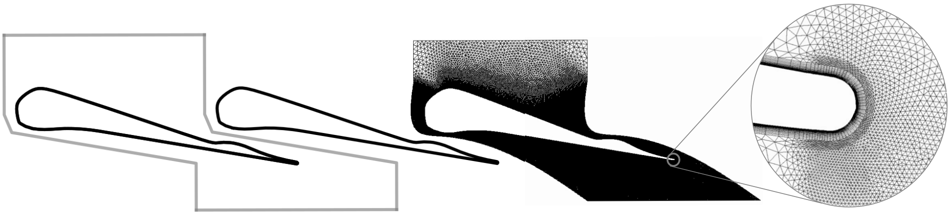

Figure 3.3: Representation of the axial vane geometry. The boundary of the computational flow domain is outlined in gray (left). The discretized computational domain is also reported (right), together with the zoomed-in view of the trailing edge.

4. *Converging section.* The converging section of the nozzle vane is generated by means of a single NURBs curve connecting the throat points ss_{o} and ps_{o} through points c_1-c_7, see Figure 3.2(d).

3.2.3.2 CFD simulation

The performance of the supersonic vanes is computed with the aid of simulations performed with the open-source CFD software tool SU2 [12, 17]. The computational domain encompassing one vane geometry is generated using UMG2, an in-house meshing program [18]. An exemplary geometry is depicted in Figure 3.3. The computational domain is discretized using clustered quadrilateral elements close to the wall, ensuring a $y^+ < 1$, and triangular elements in the rest of the flow domain. Following from a grid convergence study [19], a mesh of approximately 50,000 elements was chosen as the optimal compromise between accuracy and computational cost. The difference in the value of kinetic energy loss coefficient between the finest mesh and the one selected is 2%. The flow is simulated by solving the RANS equations and the turbulence equations are closed using the one-equation Spalart-Allmaras model [13]. The thermo-physical properties of the fluid are calculated using the polytropic perfect gas model.

The flow simulation is initialized by imposing a uniform state to the fluid everywhere in the domain, with properties corresponding to those of the total conditions at the inlet, and a value of the back pressure at the outlet. In addition, the non-reflective boundary condition, see Ref. [20], is also prescribed. The solution was obtained by using an Euler implicit time-marching scheme with a CFL of 10 while ensuring second-order spatial accuracy. Residual reduction of 4 orders of magnitude was achieved by running the simulations for a maximum of 4000 iterations.

The kinetic energy loss coefficient, accounting for both boundary-layer and mixing losses, is calculated numerically by obtaining mixed-out average quantities at the boundaries, resulting in

$$\xi_{\mathrm{CFD}} = \frac{\bar{h}_1 - h_{\mathrm{is},1}}{0.5 \cdot v_{\mathrm{is},1}^2}, \tag{3.9}$$

where, $\bar{h}_1$ is the averaged enthalpy at the outlet of the stator domain.

3.3 Case Studies

In order to identify the optimum value of the post-expansion ratio β_{a1} ($\beta_{\mathrm{opt,a1}}$), the fluid dynamic performance of the vanes with varying β_{a1} is plotted. β_{a1} is varied so as to capture the post-compression ($\beta_{\mathrm{a1}} < 1$) and post-expansion ($\beta_{\mathrm{a1}} > 1$) phenomena in the semi-bladed section of the stator vane.

The three methods are used to compute $\beta_{\mathrm{opt,a1}}$ for nozzles operating with different working fluids. The fluids under investigation range from fluids made of simple molecules to fluids made of complex molecules. This wide range of molecular complexity of the working fluids enables to capture the effect of its variation on $\beta_{\mathrm{opt,a1}}$. The selected fluids are therefore air, CO_2, toluene and siloxane MM with γ of 1.4, 1.3, 1.055 and 1.025, respectively. The stator design parameters, like, for example, the solidity (σ), the design flow angle (ϕ_{a}) and the total-to-static expansion ratio (β_{t1}), are kept constant. The stator vanes are designed for a ϕ_{a} of 70°. The solidity of the vane is constrained to unity in all cases. The test vanes are designed to operate with a β_{t1} of 6.0, and with a total temperature and pressure at the inlet of 580 K and 3.2 MPa.

In order to preliminarily assess the variation of $\beta_{\mathrm{opt,a1}}$ with the stator design parameters namely, solidity (σ), design flow angle (ϕ_{a}) and total-to-static expansion ratio (β_{t1}), vanes operating with toluene were selected. The fluid dynamic performance of the vanes was assessed by using the CFD-based method.

3.4 Results

Firstly, the accuracy of the empirical method is documented by means of a comparison of its results with the results of the analytical and the CFD-based methods for the considered working fluids. Next, the variation of $\beta_{\mathrm{opt,a1}}$ with design parameters is reported.

3.4.1 Comparison among the considered design methods

The three methods, namely the empirical, the analytical and the CFD-based methods, are employed to calculate the optimum degree of divergence (or alternatively optimum post-expansion ratio) which ensures the least amount of fluid-dynamic losses for the considered test cases.

Figure 3.4(a) illustrate the results obtained with the analytical method, that is, the trends of boundary-layer losses, mixing losses and total losses as a function of β_{a1}. As expected, the mixing losses are minimal for $\beta_{\mathrm{a1}} = 1$ and the boundary-layer losses increase with the nozzle exit Mach number, i.e., with decreasing β_{a1}. Moreover, the rate of change of the absolute value of the boundary-layer losses is much lower than that of mixing losses. Furthermore, both the boundary-layer and the mixing losses are larger for working fluids made of increasingly complex molecules, possibly because the flow Mach number is increasingly higher for the same operating conditions. The trend of the total loss ξ_{tot}, see Figure 3.4(a), suggests that different working fluids imply variations of $\beta_{\mathrm{opt,a1}}$ values, which is close to unity in all cases, as mixing-losses dominate the total loss in the stator.

The fluid-dynamic performance of the exemplary vanes are also calculated using the CFD-based method. The σ of the vanes is maintained within 1 ± 0.01 in accordance with the assumption made for the analytical method. Figure 3.4(b) reports the estimated vane performance as a function of β_{a1}. The dots represent the values obtained from numerical simulations by linearly varying the DoD while the dashed lines are trends obtained by cubic fitting, in order to identify a value of β_{a1} that can be used for design purposes. The cubic functional form was chosen somewhat arbitrarily after inspection of the trend of the total loss distribution computed with the analytical model.

As opposed to the previous findings, it can be observed that the total loss is inversely proportional to the fluid molecular complexity, i.e., the total loss is higher for flows of fluids made of simpler fluid molecules. This is attributed to shock wave losses and the dissipation due to the impingement of the shock wave on the suction side of the blade. Nonetheless, the increase in total losses from $\beta_{\mathrm{a1}} = \beta_{\mathrm{opt,a1}}$ to $\beta_{\mathrm{a1}} \neq \beta_{\mathrm{opt,a1}}$ is higher for fluids made of complex molecules. Finally, Figure 3.4(b) shows also that the value of $\beta_{\mathrm{opt,a1}}$ is different depending on the working fluid, and it increases with decreasing molecular complexity.

Additionally, it can be observed that the values of ξ_{CFD} is highly sensitive to small changes in the post-expansion ratio β_{a1}, and they become more scattered for β_{a1} away from unity. This is primarily due to the change in the position and strength of the shock wave emerging from the trailing edge of the stator vanes, which plays a key role regarding the adjustment of the flow field with respect to the imposed back pressure. Additionally, the interaction of these shock waves with wake and boundary layer influence substantially the overall performance.

Figure 3.5 depicts the Mach number contours for stator vanes operating with toluene as working fluid. The value of β_{t1} is prescribed equal to 6.0, the results of simulations are shown for decreasing β_{a1} (or increasing DoD) from left to right. Figure 3.5(b) shows the Mach contour corresponding to the vane with optimal post-expansion ratio. In all cases, a fishtail shock pattern originates at the trailing-edge of the vane. It can be seen that

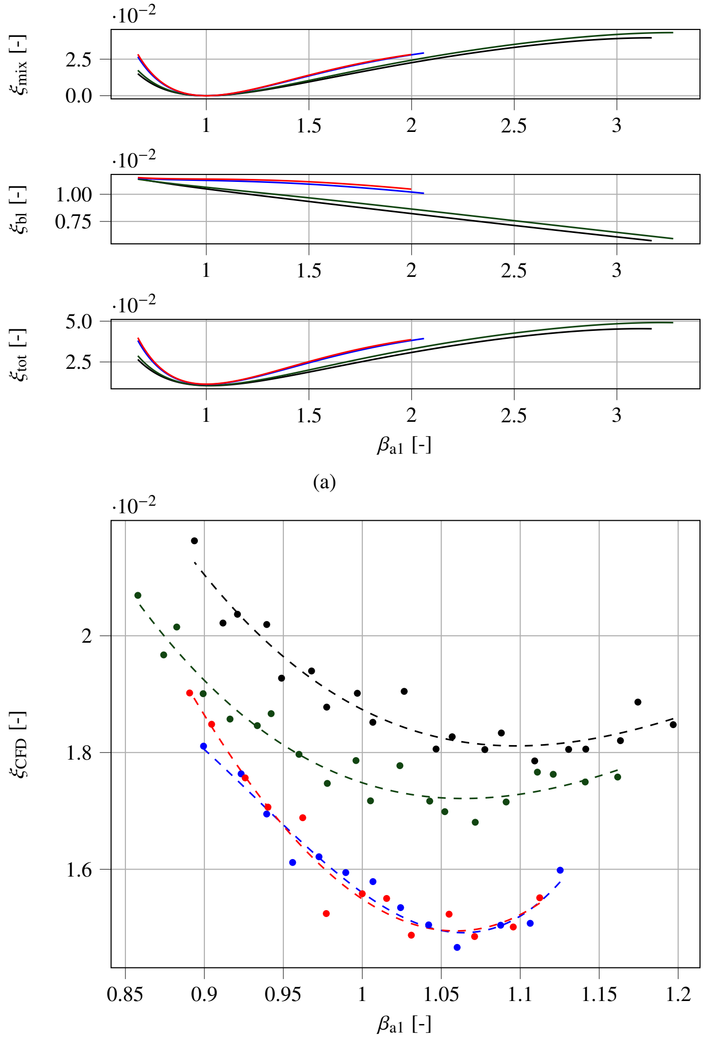

(a)

(b)

Figure 3.4: Variation of ξ with β_{a1} for stator vanes operating with β_{t1}=6.0 and ϕ_{a}=70° and with air (- - -), CO$_2$(- - -), toluene (- - -) and MM (- - -) as working fluid. (a) trend lines obtained with the analytical method, (b) trend lines obtained with the CFD-based method. The dots in (b) represent the values obtained from CFD simulations at discrete intervals of β_{a1} and the dashed lines are trend lines obtained by fitting the dots with a cubic functional form.

the strength of the pressure wave reflecting on the suction side increases with increasing DoD. This is because the flow exiting the nozzle in Figure 3.5(c) undergoes a compression

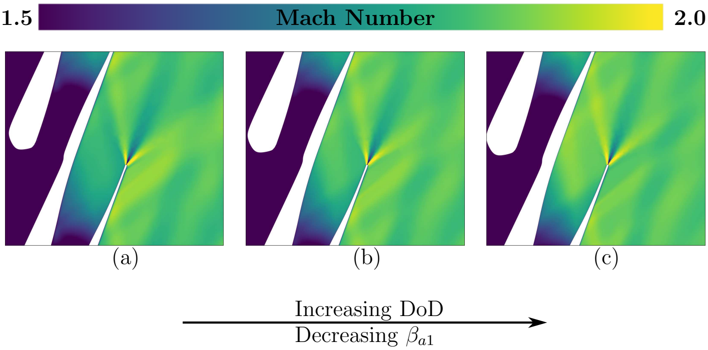

(a) (b) (c)

Figure 3.5: Mach number contours of the flow in stator vanes operating with Toluene as working fluid for β_{t1}=6.0 and ϕ_{a}=71°. From left to right: (a) β_{a1}>$\beta_{\mathrm{opt,a1}}$, (b) β_{a1}=$\beta_{\mathrm{opt,a1}}$ and (c) β_{a1}<$\beta_{\mathrm{opt,a1}}$.

($\beta_{\mathrm{a1}} < 1$), while in the case of Figure 3.5(a) and (b) the flow further expands ($\beta_{\mathrm{a1}} > 1$). The mixing of the two pressure waves downstream eventually dictates the magnitude of the deflection angle and the associated mixing-loss.

The values of $\beta_{\mathrm{opt,a1}}$ obtained with the three design methods are plotted against γ in Figure 3.6(a), which shows that the trends obtained with the three methods are similar and that flows of fluids made of complex molecules exhibit lower $\beta_{\mathrm{opt,a1}}$. Moreover, the value of $\beta_{\mathrm{opt,a1}}$ calculated using the empirical method is much higher than the value predicted by the other two methods for all the fluids.

The fluid dynamic performance of the vane operating with toluene at $\beta_{\mathrm{t1}} = 6.0$ calculated with the three methods is plotted against β_{a1} in Figure 3.6(b). From the outcomes of the analysis, it can be inferred that the use of loss models based on first principles allows one to predict values of post-expansion ratio and total loss in relatively good agreement with those predicted by more computationally expensive CFD-based methods.

3.4.2 Variation of the optimal post-expansion ratio with primary design variables

In order to assess the influence of design parameters on $\beta_{\mathrm{opt,a1}}$, the vane fluid dynamic performance was assessed with the CFD-based method without constraints on solidity, flow angle and total-to-static expansion ratio. The working fluid selected for this analysis is toluene.

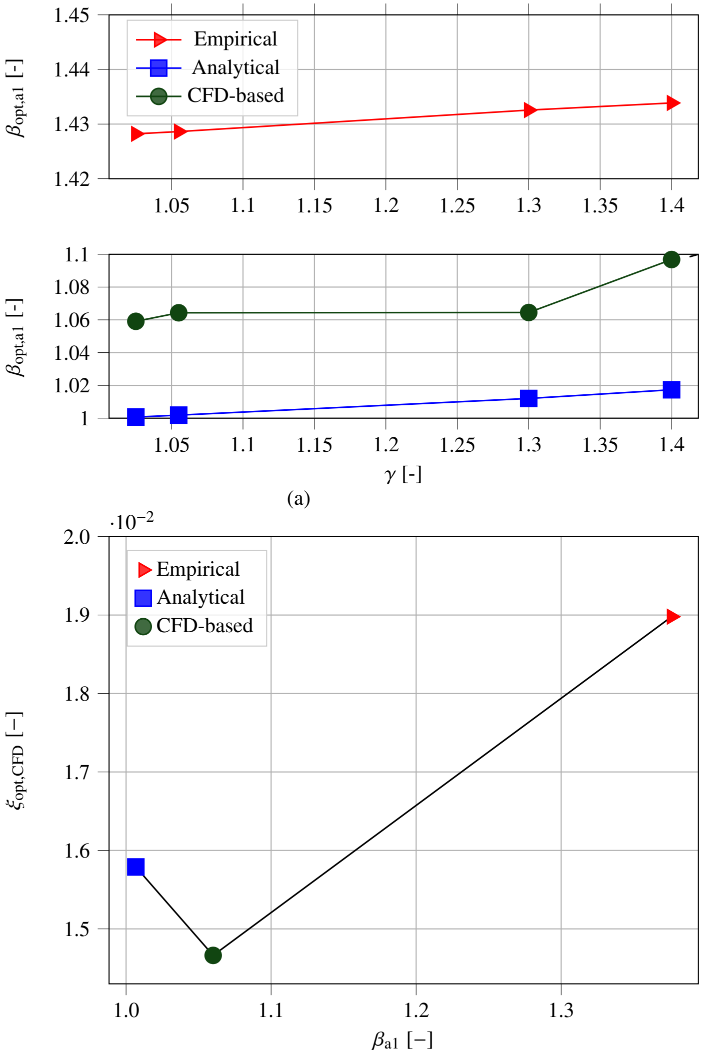

(a)

(b)

Figure 3.6: Comparison between values of $\beta_{\mathrm{opt,a1}}$ obtained with the three design methods. (a) Variation of $\beta_{\mathrm{opt,a1}}$ depending on the molecular complexity of the working fluid, and (b) ξ_{CFD} obtained by simulating the flow through the vane with the three methods, with $\beta_{\mathrm{opt,a1}}$ as expansion ratio, and with Toluene as the working fluid.

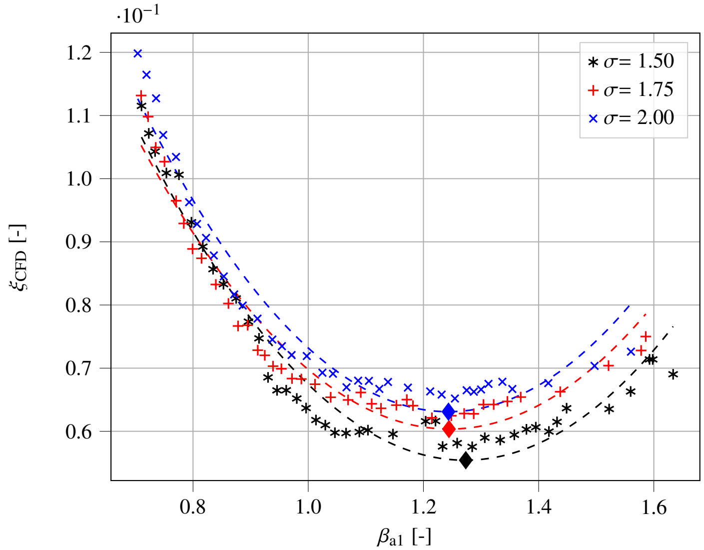

Figure 3.7: Variation of ξ_{CFD} with β_{a1} for several values of the solidity (σ) and for β_{t1}=6 and ϕ_{a}=71°. The values corresponding to the scattered points are calculated from the results of CFD simulations, while the dashed lines are trends obtained by fitting the points with a cubic functional form. The diamond on the dashed lines indicate the estimation of the value of β_{a1} that minimizes ξ_{CFD}.

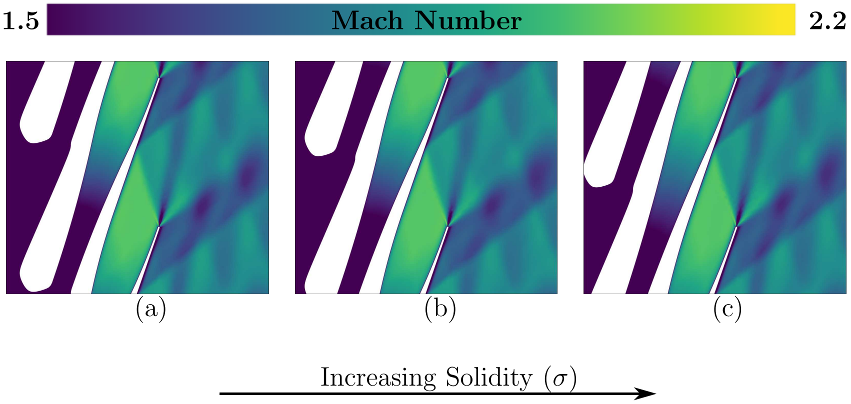

Figure 3.8: Mach number contours of the flow through stator vanes operating with Toluene as working fluid, for β_{t1}=6.0 and M_{a}=2.0, with increasing σ from left to right: (a) 1.50, (b) 1.75 and (c) 2.00.

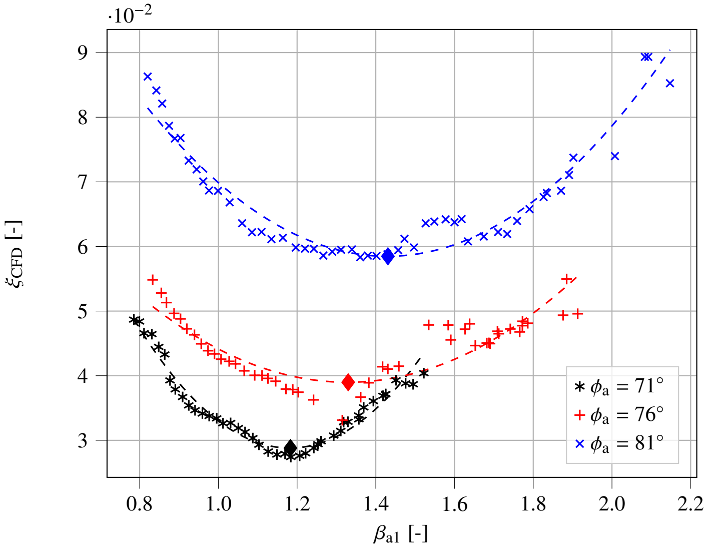

Figure 3.9: Variation of ξ_{CFD} with β_{a1} for several values of ϕ_{a}. The values corresponding to the scattered points are calculated from the results of CFD simulations, while the dashed lines are trends obtained by fitting the points with a cubic functional form. The diamonds on the dashed lines indicate the estimation of the optimal value of β_{a1}.

3.4.2.1 Influence of solidity (σ)

Figure 3.7 show the ξ_{CFD} variation related to the considered vanes as a function of β_{a1} for selected solidity values and for prescribed constant values of β_{t1} and ϕ_{a}. As expected, the losses in the vanes with higher solidity are higher compared to those with a lower solidity. This is due to the increase in the wetted surface area of the vane with increasing solidity, which increases boundary layer losses. Additionally, it can be observed that $\beta_{\mathrm{opt,a1}}$ does not change substantially for different values of solidity. In other words, the solidity parameter should not influence the choice of $\beta_{\mathrm{opt,a1}}$ (or DoD) however, for the considered cases, a lower values of solidity entails lower losses.

The Mach number contours of the vanes with varying solidity are illustrated in Figure 3.8. The overall flow characteristics, particularly the fish-tail shock pattern and shock wave boundary layer interaction remain identical across the three blades.

3.4.2.2 Influence of flow angle (ϕ_{a})

In this case, the flow angle is varied while the solidity and β_{t1} are kept constant. Figure 3.9 illustrates the variation of ξ_{CFD} with β_{a1} for three values of ϕ_{a}.

It can be observed that the losses in the vanes with higher ϕ_{a} are higher compared

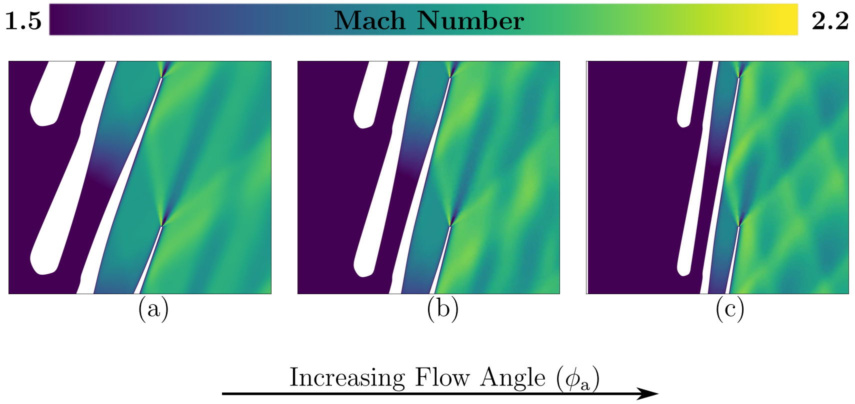

(a) (b) (c)

Figure 3.10: Mach number contours of the flow through stator vanes operating with Toluene as working fluid, for β_{t1} = 6.0 and with increasing design flow angle from left to right: (a) 71°, (b) 76° and (c) 81°.

to those of vanes with lower ϕ_a. The wetted surface area of the bladed region, see Figure 3.10, remains the same, and the nozzle geometry is unchanged as the solidity is constrained to a fixed value. However, the length of the straight section connecting the bladed region with the trailing edge increases with the flow angle, i.e., section ss_a-ss_{te} in Figure 3.2(c). Consequently, this leads to an increase of boundary layer losses for vanes with higher ϕ_a. Moreover, the boundary layer blockage effect increases with the increase of the flow angle, thus affecting the resulting boundary-layer and mixing losses. This was confirmed by the computation of the values of entropy production between the sections connecting the adjacent leading edge and the trailing edge of the vanes. These values of entropy production are 4.7, 5.23 and 9.14 $\mathrm{J{\cdot}K^{-1}}$ for ϕ_a of 71°, 76° and 81°, respectively.

From the results of Figure 3.9, it can also be inferred that the optimum post-expansion ratio increases for larger values of flow angles. This is connected to the fact that boundary-layer losses are higher for increasing ϕ_a, which can become excessively large in case the expansion ratio in the bladed region is kept at comparatively large values. This is due to the expansion ratio in the bladed region being inversely proportional to the post-expansion ratio.

Figure 3.10 reports the Mach number contours resulting from the simulation of the optimal vanes for three values of ϕ_a. It can be seen that the wakes in the vanes with higher ϕ_a, see Figure 3.10(c), are closer to each other compared to those with lower ϕ_a, see Figure 3.10(a), leading to higher mixing losses. Moreover, the trailing edge shock reflects on the suction-side surface more upstream in case of $\phi_a = 81°$ if compared to the case with $\phi_a = 71°$, see Figure 3.10(a) and (c). This explains the increase in the flow non-uniformity highlighted by the Mach contours from left to right in Figure 3.10.

It can thus be concluded that $\beta_{\mathrm{opt,a1}}$ is highly sensitive to ϕ_a.

3.4.2.3 Influence of total-to-static expansion ratio (β_{t1})

Figure 3.11 illustrates the variation of ξ_{CFD} with β_{a1} for two β_{t1} values. It can be seen that the cubic curve fitting is unsatisfactory for $\beta_{t1} = 6.0$. The choice of the cubic functional form for the fitting derived from the results obtained with the analytical method. The high-fidelity CFD simulations can predict more detailed flow features, therefore the resulting trend of the total losses can be different [11].

Additionally, the losses for higher value of β_{t1} are larger, since the Mach number in the flow channel increases with the pressure ratio. Moreover, it can be observed that for $\beta_{t1} = 8.0$ a single value of $\beta_{\text{opt,a1}}$ can be identified, while for $\beta_{t1} = 6.0$ the condition of minimum losses is achieved for a range of β_{a1} values. This is possibly a consequence of the stronger shock wave occurring at higher β_{t1} which leads to a higher sensitivity of the overall losses to the post-expansion ratio.

The Mach number contours resulting from the simulation of the optimal vanes for the two values of β_{t1} are illustrated in Figure 3.12. The overall flow characteristics, in particular the fishtail shocks and the shock wave boundary layer impingement, are similar despite the different Mach numbers. These results provide a physical justification regarding the reason why higher losses are computed for the vanes illustrated in Figure 3.11, where it can be seen that higher losses corresponds to the case with higher β_{t1}.

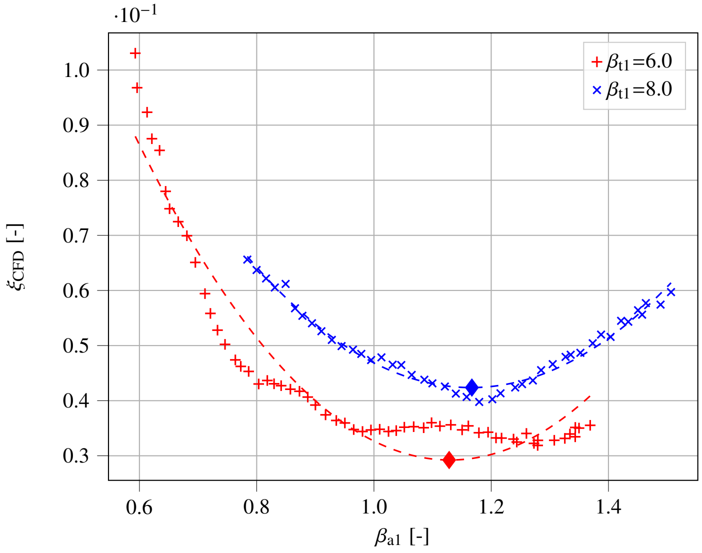

Figure 3.11: Variation of ξ_{CFD} with $\beta_{\text{opt,a1}}$, for β_{t1} of 6.0 and 8.0. The values corresponding to the scattered points are calculated from the results of CFD simulations, while the dashed lines are trends obtained by fitting the points with a cubic functional form. The diamonds on the dashed lines indicate the estimation of the optimal value of β_{a1}.

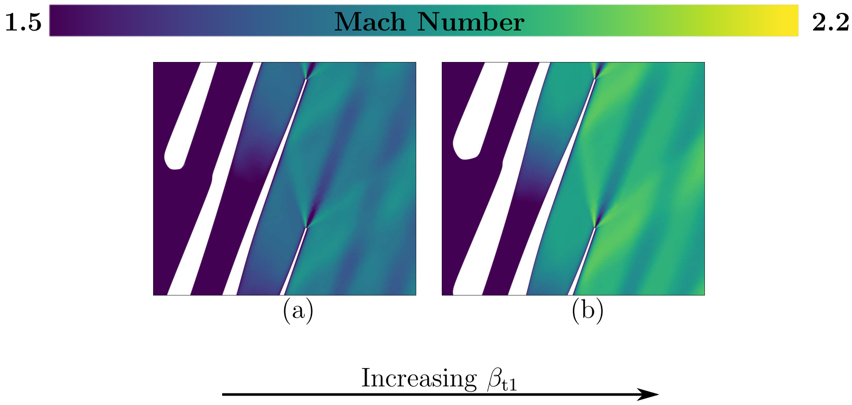

(a)

(b)

Figure 3.12: Mach number contours of the flow through vanes operating with Toluene as working fluid, for a ϕ_a=71° and σ=1.75 with increasing β_{t1} from left to right, (a) 6.0, (b) 8.0.

3.5 Conclusions

The objective of this chapter was to investigate the accuracy and thus the suitability of Deych's empirical model for the preliminary design and performance prediction of stator vanes in case the working fluid is made of complex molecules. Deych's method is currently the only one available and adopted in practice for this type of problem. Additionally, the investigation aimed at assessing the influence of primary design variables like, flow angle, expansion ratio and solidity, on the optimum post-expansion ratio of such nozzles.

To this end, the results obtained with the Deych's model were compared with the optimum post-expansion ratio calculated with a physics-based analytical method and that computed with a high-fidelity CFD-based method in some paradigmatic cases. Subsequently, the performance characteristics of a set of stator vanes with varying primary design variables was analysed by means of CFD simulations in order to assess its sensitivity to the degree of post-expansion.

The methods were applied to stator vanes operating with fluids ranging from a fluid made of simple molecules to a fluid made of complex molecules. The following conclusions can be drawn:

1. The optimal performance of axial vanes operating at supersonic flow conditions is characterized by a unique post-expansion ratio which depends on the molecular complexity of the working fluid and on the total to static pressure ratio and design flow angle.
2. The performance calculated with the Deych's method is independent of the design

flow angle and the method fails to accurately predict the optimum post-expansion ratio for a vane operating at a total to static pressure ratio of 6.0. Therefore, this method should not be used to design supersonic vanes of ORC turbines. A new method to predict the optimum post-expansion ratio of these vanes should be devised.

3. The analytical method described here, see Sec. 3.2.2, provides values of the optimal post-expansion ratio well in agreement with those given by the high-fidelity CFD-based method (Sec. 3.2.3) for the examined fluids and operating conditions. This method provided useful insights into the loss mechanisms affecting the expansion process, which, in turn, allowed to justify the unsuitability of the Deych's method for the design of ORC turbine stators.
4. The blade metal angle is found to be the design variable mostly affecting the optimum post-expansion ratio. The effect of the total-to-static expansion ratio of the cascade on the optimum post-expansion ratio requires further investigation.

Future work will be devoted to the development of simplified analytical models for the prediction of the optimum post-expansion ratio starting from data obtained from CFD simulations to be used in the conceptual design phase of supersonic ORC turbine.

Nomenclature

Symbols

$\mathcal{A}$	area ratio
A	area
C_d	dissipation coefficient
c	speed of sound
DoD	degree of divergence
h	enthalpy
L	length
l	length
M	Mach number
m	mass flow
$\mathcal{S}$	scaling factor
S	entropy
T	temperature
v	velocity
X	dimensionless chord length

Greek letters

β	expansion ratio
γ	heat capacity ratio

Δ	change in properties
ρ	density
σ	solidity
ϕ	flow angle
ξ	loss coefficient

Subscripts

1	vane outlet
a	nozzle outlet
bl	boundary layer
CFD	computational fluid dynamics
is	isentropic
mix	mixing
o	nozzle throat
opt	optimum
p	pitch distance
te	trailing edge
t	vane inlet
tot	total
x	location

Accents

$\bar{.}$	mixed-out average
$.^{*}$	symmetric equivalent
$\dot{.}$	rate of change
$\overset{\circ}{.}$	degree

References

[1] Harinck, J., Pasquale, D., Pecnik, R., van Buijtenen, J., and Colonna, P., 2013. “Performance improvement of a radial organic rankine cycle turbine by means of automated computational fluid dynamic design”. *Proceedings of the Institution of Mechanical Engineers, Part A: Journal of Power and Energy,* **227**(6), pp. 637–645.

[2] De Servi, C. M., Burigana, M., Pini, M., and Colonna, P., 2019. “Design method and performance prediction for radial-inflow turbines of high-temperature mini-organic rankine cycle power systems.”. *ASME Journal of Engineering in Gas Turbine and Power,* **141**(9), p. 091021 (12 pages).

[3] Colonna, P., Casati, E., Trapp, C., Mathijssen, T., Larjola, J., Turunen-Saaresti, T., and Uusitalo, A., 2015. “Organic Rankine Cycle Power Systems: From the Concept to Current Technology, Applications, and an Outlook to the Future”. *Journal of Engineering for Gas Turbine and Power,* **137**(10), p. 100801 (19 pages).

[4] White, M., and Sayma, A., 2016. “Improving the economy-of-scale of small organic Rankine cycle systems through appropriate working fluid selection”. *Applied Energy,* **183**, pp. 1227–1239.

[5] Colonna, P., Harinck, J., Rebay, S., and Guardone, A., 2008. “Real-gas effects in organic rankine cycle turbine nozzles”. *Journal of Propulsion and Power,* **24**(2), pp. 282–294.

[6] Rinaldi, E., Pecnik, R., and Colonna, P., 2016. “Unsteady operation of a highly Supersonic ORC Turbine”. *Journal Turbomachinery,* **138**(12), p. 121010 (9 pages).

[7] Guardone, A., Spinelli, A., and Dossena, V., 2013. “Influence of molecular complexity on nozzle design for an organic vapor wind tunnel”. *J. Eng. Gas Turb. Power,* **135**(4), p. 042307 (6 pages).

[8] Anand, N., Vitale, S., Pini, M., Otero, G. J., and Pecnik, R., 2018. “Design Methodology for Supersonic Radial Vanes Operating in Nonideal Flow Conditions”. *Journal of Engineering for Gas Turbines and Power,* **141**(2), p. 022601 (9 pages).

[9] Deych, M. E., Filippov, G. A., and Lazarev, L. Y., 1965. “Atlas of Axial Turbine Blade Characteristics”. *Mashinostroenie Publishing House*.

[10] Denton, J. D., 1993. “Loss mechanisms in turbomachines”. *Journal of Turbomachinery,* **115**(4), pp. 621–656.

[11] Osnaghi, C., 2013. *Teoria delle Turbomacchine*. Esculapio; 2nd edition.

[12] Economon, D. T., Palacios, F., Copeland, S. R., Lukaczyk, T. W., and Alonso, J. J., 2015. “SU2: An open-source suite for multiphysics simulation and design.”. *AIAA Journal,* **54**(3), pp. 828–846.

[13] Spalart, P. R., and Allmaras, S. R., 1992. “A one-equation turbulence model for aerodynamic flows”. *AIAA Journal,* **1**, pp. 5–21.

[14] Zucrow, M. J., and Hoffman, J. D., 1976. *Gas Dynamics Volume 1*, Vol. 1. John Wiley.

[15] Zucrow, M. J., and Hoffman, J. D., 1977. *Gas Dynamics Volume 2: Multidimensional Flow*, Vol. 2. John Wiley.

[16] Piegl, L., and Tiller, W., 1997. *The NURBS book*, second ed. Springer.

[17] Vitale, S., Albring, T. A., Pini, M., Gauger, N. R., and Colonna, P., 2017. “Fully turbulent discrete adjoint solver for non-ideal compressible flow applications”. *Journal of the Global Power and Propulsion Society,* **1**, pp. 252–270.

[18] Ghidoni, A., Pelizzari, E., Rebay, S., and Selmin, V., 2006. “3d anisotropic unstructured grid generation”. *International Journal for Numerical Methods in Fluids,* **51**, pp. 1097–1115.

[19] Various Authors, 2009. “Standard for Verification and Validation in Computational Fluid Dynamics and Heat Transfer”. *ASME*(ASME V&V 20), pp. 1–100.

[20] Giles, M. B., 1990. “Nonreflecting boundary condition for euler equation calculation”. *AIAA Journal,* **28**(12), pp. 2050–2058.

Part II

Adjoint-based shape optimization

The advancements in numerical methods and the availability of high-performance computational resources led to the development and evolution of automated turbomachinery design procedures. The objective function of the design method is the efficiency of the turbomachine and the variables define its geometry, namely the shape of the blades. One of the most effective mathematical approaches to automated optimization relies on obtaining objective function sensitivity information through adjoint equations. The method is effective because the computational cost of the adjoint-based optimization calculation is independent of the number of design variables. Thanks to this feature, the design space can be made very large and this is very attractive in case of unconventional turbomachinery for which the base-case is often highly sub-optimal, but also possibly in case of conventional machines in which the base-case is the result of a long history of incremental improvements, because these designs are constrained to initial choices.

Although extremely attractive for turbomachinery design problems, often simulation accuracy requires considering unsteady effects. In this case the robustness of the adjoint-based optimization framework and the cost per design step prohibitive. Stemming from these considerations, Part II of this dissertation presents two adjoint-based optimization frameworks, one for aerodynamic and another for aeroelastic design.

Chapter 4 reports about the synthesis of a robust adjoint-based aerodynamic design chain for three-dimensional turbomachinery problems. The method uses a CAD-based blade parametrisation tool developed for this purpose which provides a feasible blade geometry at each optimization design step. The blade geometry is defined and calculated with engineering parameters like blade metal angles and thickness distribution. To enable the use of deterministic optimization algorithms, the *complex-step* method is used to compute the blade surface sensitivity with respect to the design variables. The aim of this work was to couple the blade parametrisation tool to the aerodynamic design chain and demonstrate the advantages of this method in comparison to other parametrisation methods.

Chapter 5 treats the synthesis of a cost-effective and robust adjoint-based dynamic aeroelastic design chain for three-dimensional turbomachinery problems. The design chain employs the CAD-based method presented in Chapter 4 to parametrise the geometry and uses a multifrequency harmonic-balance solver to resolve the unsteady RANS equations. The aeroelastic objective is computed using the so-called *energy method.*

The capabilities of this newly developed design framework are showcased with the optimization of an exemplary fan test-case and the limitations and computational cost are discussed.

4

Development and assessment of a CAD-based parametrization method to enable adjoint-based turbomachinery optimization

The contents of this chapter appeared in:

R. Agromayor, N. Anand, J. Müller, M. Pini and L. O. Nord, 2021.
A Unified Geometry Parametrization Method for Turbomachinery Blades,
Computer-Aided Design, **133**, p. 102987 (13 pages).

N. Anand, S. Vitale, P. Colonna and M. Pini, 2018.
Assessment of FFD and CAD-Based shape parametrization methods for Adjoint-based turbomachinery shape optimization,
Proceedings of the Montreal 2018 GPPS Forum, GPPS-NA-2018-135, pp. 1–8.

© Elsevier 2021, GPPS 2018 -Reprinted with permission

Abstract *In automated design of turbomachinery, the method used to parametrize the blade shapes is key to ensure robustness and design flexibility of the entire optimization process. Currently, parametrization methods used for this purpose are often tailored to one particular type of turbomachinery blade and do not provide surface sensitivities required for gradient-based optimization. This chapter presents a parametrization method for blades of axial, radial, and mixed flow turbomachines based on typical design variables and NURBS curves and surfaces. The surface sensitivities are computed by means of the complex step method, enabling the integration of the parametrization into gradient-based shape optimization workflows. The capabilities of the method are demonstrated by optimizing a two- and a three-dimensional axial turbine test case. The results show that the developed design chain is accurate and the solution to optimization problems can be efficiently obtained.*

4.1 Introduction

In recent time, the application of shape optimization methods to turbomachinery design has arguably increased thanks to the unprecedented improvement of computer capabilities. Among the various optimization methods, the adjoint-based methods enable to find a solution to problems characterized by a large number of design variables in an efficient manner [1]. In addition, it provides the foundation to deal with multi-disciplinary and multi-physics design problems in turbomachinery [2].

One of the most critical, but often underestimated, aspects in automated design of turbomachinery is the choice of the blade shape parametrization method. Regardless of the adopted optimization method, the parametric description of the baseline geometry is key to ensure robustness of the optimization procedure without hindering the capability of the design method to provide disruptive shape configurations.

Shape parametrization methods can be classified into two categories, namely, constructive and deformation methods. Constructive methods can be used to generate the geometry of a new blade from scratch, by possibly using design variable values obtained from preliminary design models such as mean-line [3, 4] or through-flow models [5, 6]. In addition, constructive methods allow to impose geometric constraints such as minimum blade thickness in a non-intrusive way. On the other hand, deformation methods can be used to modify an existing geometry (a mesh or a CAD model). These methods include mesh point displacement [7, 8], CAD model control point displacement [9], superimposition of shape functions such as Hicks-Henne bumps [10, 11], and space morphing methods based on free form deformation (FFD) [12, 13] or on radial basis function (RBF) interpolation [14, 15]. Although these methods enable the exploration of large and varied design spaces, they are not suited for an effective handling of geometric constraints, making it difficult to obtain feasible shapes out of the optimization process.

Among these, two most popular shape parametrization methods for gradient based optimization are the FFD method and the CAD-based parametrization method. The FFD method was recently applied to turbomachinery and has gained popularity over the well-established CAD-based method, especially for gradient-based optimization [16, 17]. Although extremely flexible for exploring unconventional design solutions, the FFD method does not allow to directly control the blade geometrical characteristics (e.g., minimum thickness distribution, trailing-edge shape), leading often the optimizer to find blade shapes that are practically unfeasible. As a consequence thereof, successful optimization with FFD is usually the result of trial and error aimed at adapting the FFD box to indirectly satisfy prescribed geometrical constraints. By contrast, CAD-based methods parametrize, the blade geometry with NURBS curves, whose control points are defined by the geometrical characteristics of the blade, (e.g., the blade chord, the thickness distribution, the stagger angle). In this way, the attainment of feasible optimal shapes is automatically ensured by bounding the design variables. This, however, comes at the cost of reducing the design space.

Currently, most of the constructive CAD-based parametrization methods for turbomachinery blades described in the open literature are not suitable for automated design workflows. This is because they do not provide sensitivity information required by gradient-based optimization algorithms [18].

Stemming from this consideration, the objective of this work is to develop a unified general constructive parametrization method for axial, radial and mixed flow turbomachinery blades and to construct a gradient based shape optimization framework using the proposed method. This parametrization method exploits conventional engineering design variables (leading/trailing edge radius, metal angles, blade thickness, etc.). NURBS curves and surfaces to represent the blade geometry. The method is formulated in an explicit way such that it avoids the use of intersection and trimming operations to define the geometry of the blade and to produce blades satisfying G^2 continuity by construction. The sensitivity of the geometry with respect to the design variables is computed with machine accuracy by means of the complex step method [19, 20, 21]. The shape optimization framework results from the coupling of this parametrization method with the adjoint solver available within the open-source CFD-suite SU2 [22].

The flexibility, accuracy and the computational cost of the optimization framework here documented is demonstrated by parametrizing and optimizing a transonic axial two-dimensional and three-dimensional turbine cascade.

4.2 Methodology

4.2.1 CAD-Based shape parametrization method

The proposed blade parametrization method consists of a planar definition of the blade profile, which can be used for two-dimensional shape optimization. This method is then extended to three-dimensional cases by stacking multiple planar blades and allowing for the variation of the design variables in the span-wise direction.

Table 4.1: Two-dimensional design variables. Each design variable is provided as a scalar value, except for the upper and lower thickness that are given as sets of control points.

Variable name	Symbol
Leading edge abscissa and ordinate	$x_{\text{in}}, y_{\text{in}}$
Axial chord length	c_{ax}
Stagger angle	ξ
Inlet and exit metal angles	$\theta_{\text{in}},\ \theta_{\text{out}}$
Inlet and exit tangent proportions	$d_{\text{in}},\ d_{\text{out}}$
Inlet and exit radii of curvature	$r_{\text{in}},\ r_{\text{out}}$
Upper and lower thickness distributions	$t_{\text{upper}},\ t_{\text{lower}}$

4.2.1.1 Blade parametrization in two dimensions

The proposed two-dimensional blade parametrization is based on typical blade design variables which are listed in Table 4.1. The geometry of the blade is generated by defining a camber line and subsequently imposing on it two independent thickness distributions in a way that ensures G^2 continuity at the junction between the upper and the lower side.

The camber line $\mathbf{C}^{\text{c}}(u)$ is a cubic B-Spline curve defined by four control points as shown in Figure 4.1(a). The coordinates of the control points are given by

$$\mathbf{P}_0^{\text{c}} = \begin{bmatrix} x_{\text{in}} \\ y_{\text{in}} \end{bmatrix}, \tag{4.1}$$

$$\mathbf{P}_1^{\text{c}} = \mathbf{P}_0^{\text{c}} + d_{\text{in}} \begin{bmatrix} c\ \cos(\theta_{\text{in}}) \\ c\ \sin(\theta_{\text{in}}) \end{bmatrix}, \tag{4.2}$$

$$\mathbf{P}_2^{\text{c}} = \mathbf{P}_3^{\text{c}} - d_{\text{out}} \begin{bmatrix} c\ \cos(\theta_{\text{out}}) \\ c\ \sin(\theta_{\text{out}}) \end{bmatrix}, \tag{4.3}$$

$$\mathbf{P}_3^{\text{c}} = \mathbf{P}_0^{\text{c}} + c \begin{bmatrix} c\ \cos(\xi) \\ c\ \sin(\xi) \end{bmatrix}, \tag{4.4}$$

where ξ is the stagger angle, $c_{\text{ax}} = c\ \cdot \cos(\xi)$ is the axial chord length, θ_{in} and θ_{out} are the inlet and outlet metal angles, and d_{in} and d_{out} are the inlet and outlet tangent proportions. This construction of the camber line ensures that the slope at the leading and trailing edges conforms with the input metal angles by construction thanks to the endpoint tangency property of B-Spline curves [23, p. 97].

The upper and lower sides (alternatively, suction and the pressure side) of the blade, $\mathbf{C}^{l}(u)$ and $\mathbf{C}^{\text{u}}(u)$, are defined as quartic B-Spline curves with control points $\{\mathbf{P}_i^{l}\}$ and $\{\mathbf{P}_i^{\text{u}}\}$, see Figure 4.1(b). The coordinates of these control points are computed according to

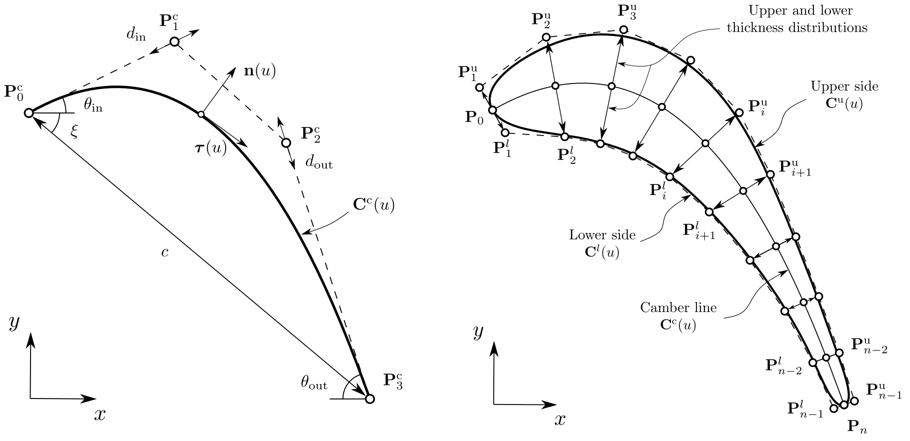

(a) Camber line construction.

(b) Blade profile construction.

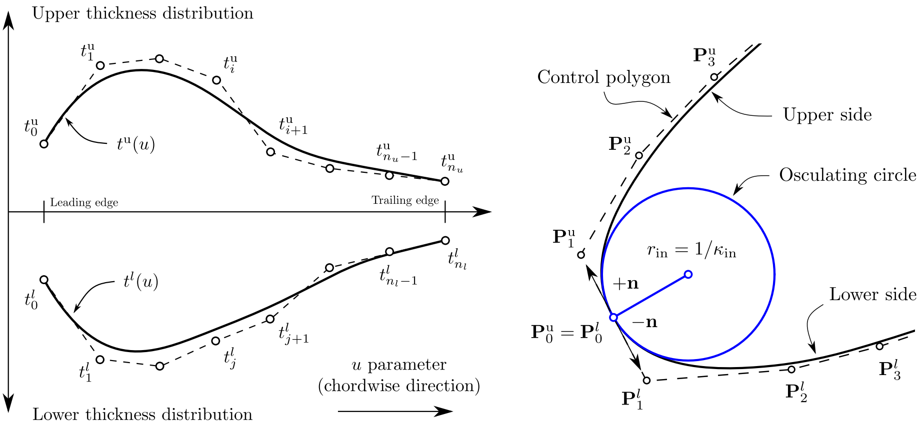

(c) Thickness distribution.

(d) Leading edge construction.

Figure 4.1: Construction of the blade geometry in two dimensions. The upper and lower thickness distributions (bottom-left) are defined in the direction normal to the camber line (top-left) to compute the location of the blade control points (top-right). The second and second-to-last control points are computed in a special way to define the radii of curvature at the leading and trailing edges and to ensure that the blade profile is G^2 continuous (bottom-right).

$$\mathbf{P}_i^l = \begin{cases} \mathbf{C}^{\mathrm{c}}(\hat{u}_i), & \text{for } i = 0 \\ \mathbf{C}^{\mathrm{c}}(\hat{u}_i) - \mathbf{n}(\hat{u}_i) \cdot f(r_{\mathrm{in}}), & \text{for } i = 1 \\ \mathbf{C}^{\mathrm{c}}(\hat{u}_i) - \mathbf{n}(\hat{u}_i) \cdot t^l(\hat{u}_i), & \text{for } i = 2, \ldots, n-2 \\ \mathbf{C}^{\mathrm{c}}(\hat{u}_i) - \mathbf{n}(\hat{u}_i) \cdot g(r_{\mathrm{out}}), & \text{for } i = n-1 \\ \mathbf{C}^{\mathrm{c}}(\hat{u}_i), & \text{for } i = n \end{cases} \tag{4.5}$$

and

$$\mathbf{P}_i^{\mathrm{u}} = \begin{cases} \mathbf{C}^{\mathrm{c}}(\hat{u}_i), & \text{for } i = 0 \\ \mathbf{C}^{\mathrm{c}}(\hat{u}_i) + \mathbf{n}(\hat{u}_i) \cdot f(r_{\mathrm{in}}), & \text{for } i = 1 \\ \mathbf{C}^{\mathrm{c}}(\hat{u}_i) + \mathbf{n}(\hat{u}_i) \cdot t^{\mathrm{u}}(\hat{u}_i), & \text{for } i = 2, \ldots, n-2 \\ \mathbf{C}^{\mathrm{c}}(\hat{u}_i) + \mathbf{n}(\hat{u}_i) \cdot g(r_{\mathrm{out}}), & \text{for } i = n-1 \\ \mathbf{C}^{\mathrm{c}}(\hat{u}_i), & \text{for } i = n. \end{cases} \tag{4.6}$$

The sampling values $\hat{u}_i$ in the above equations are given by

$$\hat{u}_i = \begin{cases} 0, & \text{for } i = 0 \\ \dfrac{i-1}{n-2}, & \text{for } i = 1, \ldots, n-1 \\ 1, & \text{for } i = n. \end{cases} \tag{4.7}$$

The upper and lower thickness distributions, $t^{\mathrm{u}}(u)$ and $t^l(u)$, are given by B-Spline polynomials of degree three with an arbitrary number of control points (n), $\{t_i^{\mathrm{u}}\}$ and $\{t_j^l\}$, specified by the user, see Figure 4.1(c).

The unitary vector normal to the camber line $\mathbf{n}(u)$ are computed from the unitary tangent vector $\boldsymbol{\tau}(u)$ according to

$$\boldsymbol{n}(u) = \begin{bmatrix} n_x \\ n_y \end{bmatrix} = \begin{bmatrix} -\tau_y \\ \tau_x \end{bmatrix}, \qquad \text{with} \qquad \boldsymbol{\tau}(u) = \frac{\dot{\mathbf{C}}^{\mathrm{c}}(u)}{\|\dot{\mathbf{C}}^{\mathrm{c}}(u)\|}, \tag{4.8}$$

where $\dot{\mathbf{C}}^{\mathrm{c}}(u)$ is computed using analytical derivative equations for B-Spline curves [23, pp. 91–100].

The functions $f(r)$ and $g(r)$ appearing in Eqn. (4.5) and (4.6) are used to impose the radii of curvature r_{in} and r_{out} at the leading and trailing edges, ensuring that the parametrization satisfies G^2 continuity by construction, see Figure 4.1(d).

Once that the upper and lower sides are defined, they can be combined into a single B-Spline curve $\mathbf{C}^{\mathrm{b}}(u) = \mathbf{C}^l \cup \mathbf{C}^{\mathrm{u}}$ that represents the entire blade profile.

Some of the exemplary blade profiles generated using this two-dimensional blade parametrization method are illustrated in Figure 4.2.

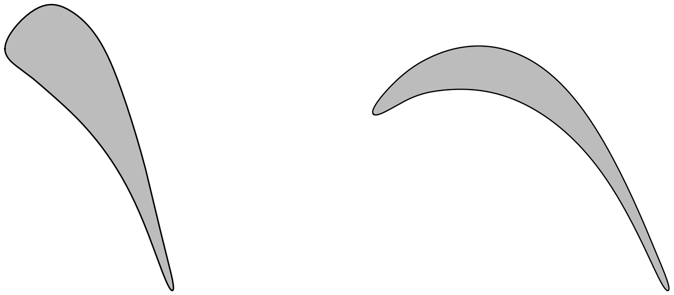

(a) LS89 [24, 25]

(b) T106A [26]

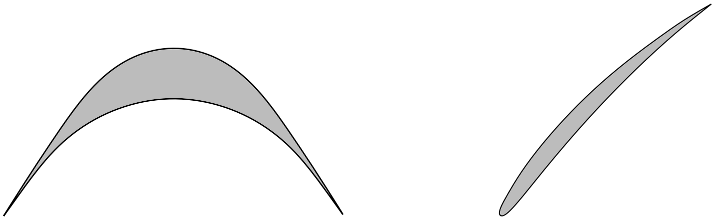

(c) SIRT [27]

(d) STD10 [28]

Figure 4.2: Example of two-dimensional blade geometries generated using the proposed blade parametrization method.

4.2.1.2 Blade parametrization in three dimensions

The proposed three-dimensional parametrization is formulated as an extension of the two-dimensional parametrization and makes use of the design variables listed in Table 4.2. Similarly to the two-dimensional case, the parametrization procedure starts from the definition of a camber surface and subsequently defining two independent thickness distributions perpendicular to the camber surface in a way that ensures G^2 continuity.

The camber surface is determined by the shape of the blade in the meridional plane and the spanwise variation of the design variables. The shape of the blade in the meridional plane is described by four curves, namely, leading edge, trailing edge, hub, and shroud, as illustrated in Figure 4.3. Each of these boundaries is defined as a B-Spline curve of, at most, degree three with an arbitrary number of control points (n), see Figure 4.4. Contrary to other parametrization methods that are limited to axial turbomachines [29, 30, 31, 32, 33], the proposed method allows to describe any kind of turbomachinery configuration, including axial, radial, and mixed flow machines. The number of control points required to describe the shape of the blade in the meridional plane depends on the complexity of the geometry. For instance, it is possible to define a purely axial turbine using only four control points, but it may be necessary to use 10–20 control points to describe the shape

Table 4.2: Three-dimensional design variables. Each design variable is provided as a set of control points that defines a continuous variation, except for the number of blades that is a scalar value.

Variable name	Symbol
Leading edge control points	x_1, z_1
Hub edge control points	x_2, z_2
Trailing edge control points	x_3, z_3
Shroud edge control points	x_4, z_4
Leading edge abscissa*	y_{in}
Stagger angle*	ξ
Inlet and exit metal angles*	θ_{in}, θ_{out}
Inlet and exit tangent proportions*	d_{in}, d_{out}
Inlet and exit radii of curvature*	r_{in}, r_{in}
Upper and lower thickness distributions	t^{u}, t^{l}

* Law of evolution in the spanwise direction.

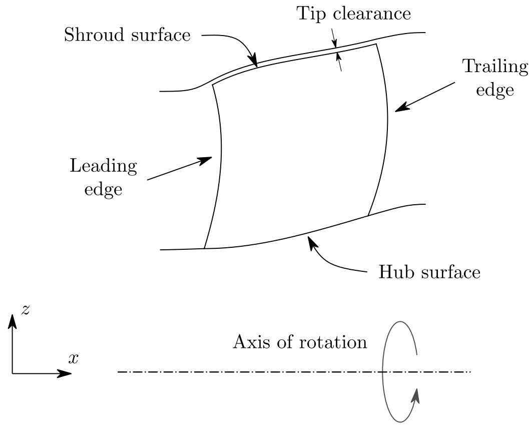

Figure 4.3: Geometry of the blade in the meridional plane.

of a mixed flow machine such as a centrifugal compressor.

The spanwise variation of the each design variable is defined as law of evolution through a B-Spline of, at most, degree three with an arbitrary number of control points as illustrated in Figure 4.5. The number of control points used for each design variable is specified by the user, and its selection is based on the complexity of the blade geometry. As an example, it is sufficient to use a single constant value to define a prismatic blade, but it might be necessary to use 3–6 control points to describe the geometry of a strongly twisted blade.

Using the meridional plane and the spanwise evolution of the design variables, the

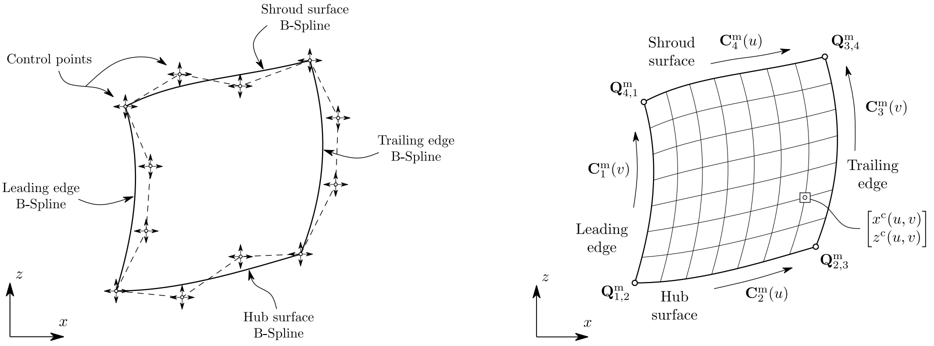

Figure 4.4: Construction of the four B-Splines which define the shape of the blade in the meridional plane (left) and point evaluation by transfinite interpolation (right). Note that the corner control points of the B-Splines are shared.

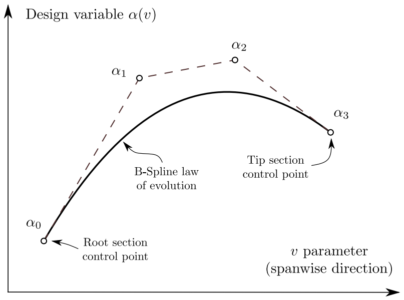

Figure 4.5: Spanwise variation of a design variable.

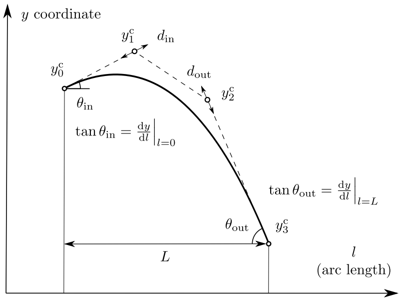

Figure 4.6: Tangential camber line coordinate.

camber surface $\mathbf{S}^{\mathrm{c}}(u,v)$ can be defined as a bi-quartic B-Spline surface with control points

$$\mathbf{P}_{i,j}^{\mathrm{c}} = \begin{bmatrix} x_{i,j}^{\mathrm{c}} \\ y_{i,j}^{\mathrm{c}} \\ z_{i,j}^{\mathrm{c}} \end{bmatrix}, \tag{4.9}$$

as illustrated in Figure 4.7(a). The (x,z) coordinates of the control points are computed by transfinite interpolation [34] of the four curves that define the meridional plane, see Figure 4.4, and are given by

$$\begin{aligned} \begin{bmatrix} x^{\mathrm{c}}(u,v) \\ z^{\mathrm{c}}(u,v) \end{bmatrix} &= (1-u)\cdot\mathbf{C}_1^{\mathrm{m}}(v) + u\cdot\mathbf{C}_3^{\mathrm{m}}(v) + (1-v)\cdot\mathbf{C}_2^{\mathrm{m}}(u) + v\cdot\mathbf{C}_4^{\mathrm{m}}(u) \\ &\quad - \left[(1-v)(1-u)\cdot\mathbf{Q}_{1,2}^{\mathrm{m}} + v\,u\cdot\mathbf{Q}_{3,4}^{\mathrm{m}} + v\,(1-u)\cdot\mathbf{Q}_{4,1}^{\mathrm{m}} + (1-v)\,u\cdot\mathbf{Q}_{2,3}^{\mathrm{m}}\right], \end{aligned} \tag{4.10}$$

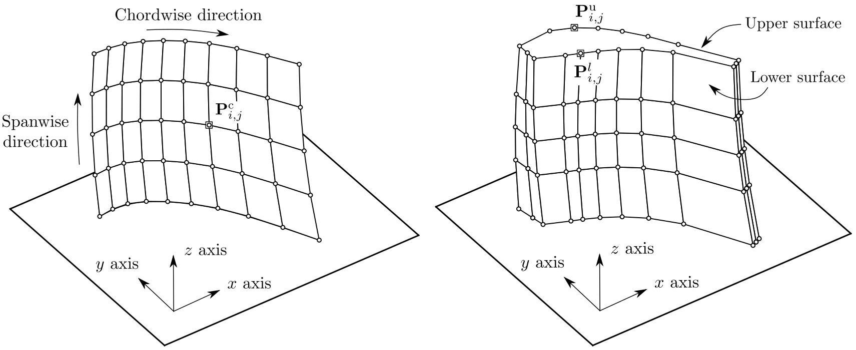

(a) Camber surface.

(b) Blade surface.

Figure 4.7: Lattice of control points that define the surfaces.

In addition, the y coordinates of the control points at each spanwise location v are given by a third order B-Spline curve $y^{\mathrm{c}}(u, v)$ with control points $\{y^{\mathrm{c}}_0, y^{\mathrm{c}}_1, y^{\mathrm{c}}_2, y^{\mathrm{c}}_3\}$ computed according to

$$y^{\mathrm{c}}_0(v) = y_{\mathrm{in}} \tag{4.11}$$

$$y^{\mathrm{c}}_1(v) = y^{\mathrm{c}}_0 + d_{\mathrm{in}} \cdot L \tan\theta_{\mathrm{in}} \tag{4.12}$$

$$y^{\mathrm{c}}_2(v) = y^{\mathrm{c}}_3 - d_{\mathrm{out}} \cdot L \tan\theta_{\mathrm{out}} \tag{4.13}$$

$$y^{\mathrm{c}}_3(v) = y_{\mathrm{in}} + L \tan\xi. \tag{4.14}$$

This formulation ensures that the metal angles at the leading and trailing edges, θ_{in} and θ_{out}, are respected, as illustrated in Figure 4.6. The arc length of the blade meridional plane at each span location $L(v)$ is defined as

$$L(v) = \int_{u=0}^{u=1} \sqrt{\left(\frac{\partial x^{\mathrm{c}}}{\partial u}\right)^2 + \left(\frac{\partial z^{\mathrm{c}}}{\partial u}\right)^2}\mathrm{d}u \tag{4.15}$$

and it is computed using 8th order Gaussian quadrature [35] because it provides a satisfactory trade-off between computational speed and accuracy.

The upper and lower sides of the blade, $\mathbf{S}^{l}(u, v)$ and $\mathbf{S}^{\mathrm{u}}(u, v)$, are defined as bi-quartic B-Spline surfaces with control points $\{\mathbf{P}^{l}_{i,j}\}$ and $\{\mathbf{P}^{\mathrm{u}}_{i,j}\}$ as illustrated in Figure 4.7(b). The coordinates of these control points are given by

$$\mathbf{P}^{l}_{i,j} = \begin{cases} \mathbf{S}^{\mathrm{c}}(\hat{u}_i, \hat{v}_j), & \text{for } i = 0 \\ \mathbf{S}^{\mathrm{c}}(\hat{u}_i, \hat{v}_j) - \mathbf{n}(\hat{u}_i, \hat{v}_j) \cdot f(r_{\mathrm{in}}(\hat{v}_j)), & \text{for } i = 1 \\ \mathbf{S}^{\mathrm{c}}(\hat{u}_i, \hat{v}_j) - \mathbf{n}(\hat{u}_i, \hat{v}_j) \cdot t^{l}(\hat{u}_i, \hat{v}_j), & \text{for } i = 2, \dots, n-2 \\ \mathbf{S}^{\mathrm{c}}(\hat{u}_i, \hat{v}_j) - \mathbf{n}(\hat{u}_i, \hat{v}_j) \cdot g(r_{\mathrm{out}}(\hat{v}_j)), & \text{for } i = n-1 \\ \mathbf{S}^{\mathrm{c}}(\hat{u}_i, \hat{v}_j), & \text{for } i = n \end{cases} \tag{4.16}$$

and

$$\mathbf{P}^{\mathrm{u}}_{i,j} = \begin{cases} \mathbf{S}^{\mathrm{c}}(\hat{u}_i, \hat{v}_j), & \text{for } i = 0 \\ \mathbf{S}^{\mathrm{c}}(\hat{u}_i, \hat{v}_j) + \mathbf{n}(\hat{u}_i, \hat{v}_j) \cdot f(r_{\mathrm{in}}(\hat{v}_j)), & \text{for } i = 1 \\ \mathbf{S}^{\mathrm{c}}(\hat{u}_i, \hat{v}_j) + \mathbf{n}(\hat{u}_i, \hat{v}_j) \cdot t^{\mathrm{u}}(\hat{u}_i, \hat{v}_j), & \text{for } i = 2, \dots, n-2 \\ \mathbf{S}^{\mathrm{c}}(\hat{u}_i, \hat{v}_j) + \mathbf{n}(\hat{u}_i, \hat{v}_j) \cdot g(r_{\mathrm{out}}(\hat{v}_j)), & \text{for } i = n-1 \\ \mathbf{S}^{\mathrm{c}}(\hat{u}_i, \hat{v}_j), & \text{for } i = n \end{cases} \tag{4.17}$$

where the sampling values $(\hat{u}_i, \hat{v}_j)$ are given by

$$\hat{u}_i = \begin{cases} 0, & \text{for } i = 0 \\ \dfrac{i-1}{n-2}, & \text{for } i = 1, \dots, n-1 \\ 1, & \text{for } i = n \end{cases} \quad \text{and} \quad \hat{v}_j = \frac{j}{m}, \quad \text{for } j = 0, \dots, m. \tag{4.18}$$

The upper and lower thickness distributions, $t^{\mathrm{u}}(u, v)$ and $t^{l}(u, v)$, are given by bi-variate B-Spline polynomials of degree three with an arbitrary number of control points $\{t^{\mathrm{u}}_{i,j}\}$ and $\{t^{l}_{i,j}\}$, specified by the user. The unitary vectors normal to the camber surface $\mathbf{n}(u, v)$ are computed from the tangent vectors $\boldsymbol{\tau}_u$ and $\boldsymbol{\tau}_v$ according to

$$\mathbf{n} = -\frac{\boldsymbol{\tau}_u \times \boldsymbol{\tau}_v}{\|\boldsymbol{\tau}_u \times \boldsymbol{\tau}_v\|}, \quad \text{with} \quad \boldsymbol{\tau}_u = \frac{\partial \mathbf{S}^{\mathrm{c}}}{\partial u} \quad \text{and} \quad \boldsymbol{\tau}_v = \frac{\partial \mathbf{S}^{\mathrm{c}}}{\partial v}. \tag{4.19}$$

The partial derivatives of the camber surface with respect to u and v are computed analytically using B-Spline surface derivative formulas [23, pp. 110–115].

The upper and lower sides of the blade are defined as bi-quartic B-Spline surfaces so as to obtain a smooth curvature distribution. This feature is important to avoid spikes and dips in the surface-pressure distribution, which may lead to flow separation and deteriorate the fluid dynamic performance of the blade [36]. In addition, the functions $f(r)$ and $g(r)$ appearing in Eqns. (4.16) and (4.17) are used to impose the radius of curvature at the leading and trailing edges, ensuring that the upper and lower surfaces of the blade are smoothly joined with G^2 continuity. Once the upper and lower sides are defined, they can be combined into a single B-Spline surface $\mathbf{S}^{\mathrm{b}}(u, v) = \mathbf{S}^{l} \cup \mathbf{S}^{\mathrm{u}}$ that represents the entire blade.

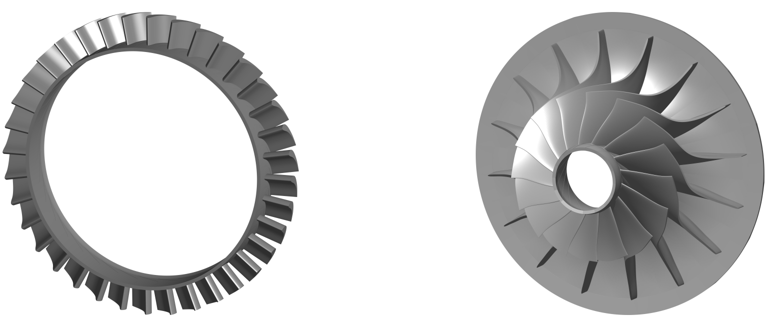

(a) AACHEN stator [37].

(b) APU rotor [38, 39].

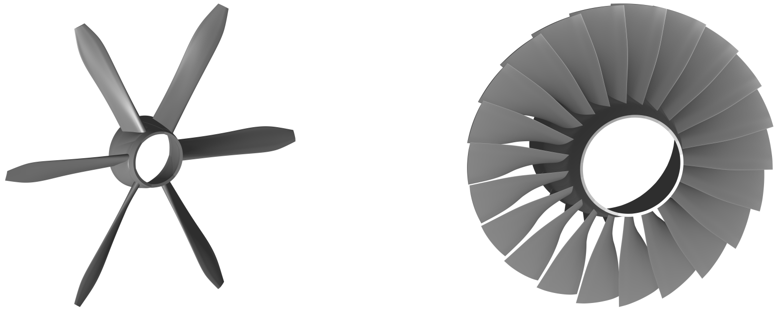

(c) XPROP propeller [40].

(d) NASA Rotor 67 [41, 42].

Figure 4.8: Three-dimensional blade geometries generated using the proposed blade parametrization method.

This parametrization method is suitable to model linear cascades, which are commonly used for wind tunnel tests. However, in actual turbomachines, the blades are arranged in an axisymmetric way forming an annular cascade. In order to parametrize axisymmetric blade cascade, a linear blade configuration is transformed into an annular cascade by applying the transformation $\mathcal{H} : \mathbb{R}^3 \to \mathbb{R}^3$ given by

$$\mathbf{P}^{\mathrm{b}}_{\mathrm{annular}} = \mathcal{H}\left\{\mathbf{P}^{\mathrm{b}}_{\mathrm{linear}}\right\} = \mathcal{H}\left\{[x,\, y,\, z]\right\} = \left[x,\, z \cdot \sin(y/z),\, z \cdot \cos(y/z)\right]. \tag{4.20}$$

The rationale behind this mapping is that the Cartesian coordinates (x, y, z) of a linear cascade can be mathematically associated with the cylindrical coordinates $(x, r\theta, r)$ of an annular cascade.

Some exemplary annular blade cascades generated using the three-dimensional blade parametrization method are illustrated in Figure 4.8.

To enable use of gradient based optimization algorithms during the autoamted CFD-based design process, sensitivity of the blade co-ordinates with respect to the design variables (listed in Table 4.1 and 4.2) is essential. In the current implementation, this sensitivity information is computed with machine accuracy by means of complex-step derivative

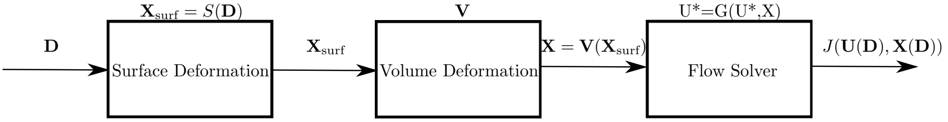

Figure 4.9: Schematic representation of fluid-dynamic design chain [16].

approximation method [21].

4.2.2 Aerodynamic optimization framework

The shape optimization design chain encompassing the proposed CAD-based parametrization method is schematically illustrated in Figure 4.9. In this design chain, a change of the position the design variables, denoted as $\mathbf{D}$, causes a variation of the blade shape, $\mathbf{X}_{\text{surf}}$, which in turn requires a continuous deformation of the volume mesh $\mathbf{X}$. The deformed mesh is then given as an input to the flow solver to compute the flow solution $\mathbf{U}$ and to estimate the objective function $J(\mathbf{U}(\mathbf{D}), \mathbf{X}(\mathbf{D}))$.

4.2.2.1 Surface Deformation (S)

The surface deformation is performed using the proposed CAD-based blade parametrization method. The CAD-representation of the surface coordinates can be written as

$$\mathbf{X}_{\text{CAD}}(\mathbf{D}) = \mathbf{B}(\mathbf{D}, u), \tag{4.21}$$

where, $\mathbf{B}$ is the blade parametrization algorithm, $\mathbf{D}$ is the vector of the design variables tabulated in Table 4.1 and Table 4.2, and u is the vector of the B-Spline parametric coordinates.

In order to implement a procedure that is independent of the mesh-generation algorithm, it is generally assumed that the blade representation within the mesh domain is mathematically different from the one constructed with the CAD-based model, i.e.

$$\mathbf{X}_{\text{surf}} \neq \mathbf{X}_{\text{CAD}}, \tag{4.22}$$

where, $\mathbf{X}_{\text{surf}}$ is the coordinates of the blade surface on the mesh. However, if $\mathbf{X}_{\text{CAD}}$ is constructed so that

$$\sqrt{\frac{\sum_{n=1}^{N} \left[\mathbf{X}_{\text{surf},n} - \mathbf{B}(\mathbf{D}, u_n)\right]^2}{N}} << 1, \tag{4.23}$$

it can be assumed that for each n-th point of the surface mesh

$$\Delta \mathbf{X}^k_{\text{surf},n} = \mathbf{X}^k_{\text{CAD},n}(\mathbf{D}^k) - \mathbf{X}^{k-1}_{\text{CAD},n}(\mathbf{D}^{k-1}) = \mathbf{B}(\mathbf{D}^k, u_n) - \mathbf{B}(\mathbf{D}^{k-1}, u_n) \tag{4.24}$$

where u_n represents the B-Splines local parameter that maps the n-th point of $\mathbf{X}_{\text{surf}}$ into $\mathbf{X}_{\text{CAD}}$ using a minimum distance algorithm, N is the total number of points of $\mathbf{X}_{\text{surf}}$ and k represents the optimization step.

4.2.2.2 Volume Deformation (V)

Since re-meshing the computational grid after each design step can be relatively CPU-intensive and could lead to different mesh densities at each design step, the mesh deformation method presented in Ref. [43] is applied. In this approach, the mesh is modeled as an elastic solid using the linear elasticity equations. Hence, if a surface deformation $\Delta\mathbf{X}_{\text{surf}}$ is imposed as Dirichlet condition, the mesh deformation $\Delta\mathbf{X}$ can be computed by solving the following linear system:

$$\mathbf{K}\Delta\mathbf{X} = \mathbf{T}\Delta\mathbf{X}_{\text{surf}}, \tag{4.25}$$

where, $\mathbf{K}$ is a stiffness matrix defined by a user defined constant and $\mathbf{T}$ is a projection matrix which re-orders $\Delta\mathbf{X}_{\text{surf}}$ in accordance with $\mathbf{X}$. The mesh corresponding to the next iterations k is then given by:

$$\mathbf{X}^k = \mathbf{X}^{k-1} + \Delta\mathbf{X}^k. \tag{4.26}$$

4.2.2.3 Flow Solver

The compressible RANS equations are commonly discretized using the conservative formulation

$$\partial_t \mathbf{U} + \nabla \cdot \mathbf{F}^c - \nabla \cdot \mathbf{F}^v = \mathbf{Q} \quad \text{in } \Omega, t > 0. \tag{4.27}$$

Equation (4.27) represents the mass, momentum and energy balance equations in a control volume. In this equation, $\mathbf{U}$ is the vector of the conservative equations variables, $\mathbf{F}^c$ is the vector of convective fluxes, $\mathbf{F}^v$ is the vector of viscous fluxes and $\mathbf{Q}$ is a generic source term. The integral form of this equation can be expressed as

$$\int_{\Omega_i} \frac{\partial \mathbf{U}}{\partial t} d\Omega + \sum_{j \in \mathcal{N}(i)} (F^c_{i,j} + F^v_{i,j}) \Delta S_{i,j} - \mathbf{Q}|\Omega_i| = 0, \tag{4.28}$$

$$\int_{\Omega_i} \frac{\partial \mathbf{U}}{\partial t} d\Omega + \mathbf{R}_i(\mathbf{U}) = 0, \tag{4.29}$$

where, $\Delta S_{i,j}$ is the area of the face associated with the edge ij, Ω_i is the control volume associated with the node i, $\mathcal{N}(i)$ are the neighbouring j-th nodes to the node volume associated with the node i, and $\mathbf{R}_i$ is the residual obtained by balancing the conservative equation across the control volume. The resulting time integration with an implicit Euler scheme can be written as the following linear system

$$\left(\frac{\Omega\mathbf{I}}{\Delta t} + \mathbf{J}\right)\Delta\mathbf{U}_n = -\mathbf{R}_i(\mathbf{U}_n). \tag{4.30}$$

As shown in Ref. [16], $\mathbf{G}(\mathbf{U}, \mathbf{X})$ is the *fixed point* operator representing the time integration of the RANS equations according to an implicit Euler method, i.e.,

$$\mathbf{U}^{n+1} = \mathbf{G}(\mathbf{U}^n, \mathbf{X}). \tag{4.31}$$

It is assumed that $\mathbf{G}$ is stationary only at point $\mathbf{U}^*$:

$$\mathbf{R}(\mathbf{U}^*, \mathbf{X}) = 0 \Leftrightarrow \mathbf{U}^* = \mathbf{G}(\mathbf{U}^*, \mathbf{X}) \tag{4.32}$$

where $\mathbf{R}$ is the residual vector obtained from the spatial integration of the flow equations.

4.2.2.4 Sensitivities Computation

The optimization problem of the design chain described above can be expressed as

$$\min_D \quad J(\mathbf{U}(\mathbf{D}), \mathbf{X}(\mathbf{D})), \tag{4.33}$$

$$\text{s.t.} \quad \mathbf{U} = \mathbf{G}(\mathbf{U}, \mathbf{X}), \tag{4.34}$$

$$\mathbf{X} = \mathbf{M}(\mathbf{D}) = \mathbf{V}(\mathbf{S}(\mathbf{D})). \tag{4.35}$$

The adjoint derivation by means of Lagrangian multipliers allows to write the adjoint equation and the mesh sensitivity equation as

$$\bar{\mathbf{U}} = \frac{\partial}{\partial \mathbf{U}} J^T(\mathbf{U}, \mathbf{X}) + \frac{\partial}{\partial \mathbf{U}} \mathbf{G}^T(\mathbf{U}, \mathbf{X})\bar{\mathbf{U}}, \tag{4.36}$$

$$\bar{\mathbf{X}} = \frac{\partial}{\partial \mathbf{X}} J^T(\mathbf{U}, \mathbf{X}) + \frac{\partial}{\partial \mathbf{X}} \mathbf{G}^T(\mathbf{U}, \mathbf{X})\bar{\mathbf{U}}. \tag{4.37}$$

Once a numerical solution for the adjoint variables $\bar{\mathbf{U}}$ is found through an iterative procedure, the mesh node sensitivity $\bar{\mathbf{X}}$ is computed from its explicit definition, see Eq. (4.37). The total derivative of J with respect to the design variables is therefore given by

$$\frac{\mathrm{d}J}{\mathrm{d}\mathbf{D}}^T = \frac{\mathrm{d}}{\mathrm{d}\mathbf{D}} \mathbf{M}^T(\mathbf{D})\bar{\mathbf{X}}, \tag{4.38}$$

where, **M** represents the mesh operator consisting of surface deformation operator (**S**) defined in section 4.2.2.1 and volume deformation operator (**V**) defined in section 4.2.2.2. In order to compute the sensitivity $\frac{\mathrm{d}J}{\mathrm{d}\mathbf{D}}$, the volume deformation and the surface deformation routines must be differentiated yielding

$$\frac{\mathrm{d}\mathbf{M}}{\mathrm{d}\mathbf{D}} = \frac{\mathrm{d}\mathbf{X}}{\mathrm{d}\mathbf{X}_{\mathrm{surf}}} \cdot \frac{\mathrm{d}\mathbf{X}_{\mathrm{surf}}}{\mathrm{d}\mathbf{D}}, \tag{4.39}$$

where, the term $\frac{\mathrm{d}\mathbf{X}}{\mathrm{d}\mathbf{X}_{\mathrm{surf}}}$ is obtained using CodiPack [44], an algorithmic differentiation tool, while the term $\frac{\mathrm{d}\mathbf{X}_{\mathrm{surf}}}{\mathrm{d}\mathbf{D}}$ is computed using the complex-step method implemented within the blade parametrization tool.

The cost of computing surface sensitivity using complex-step method is negligible if compared to the cost of one CFD run.

4.3 Case Study: Transonic stator blade

The capability of the shape optimization framework is assessed by applying the numerical procedure to the blade of a subsonic turbine stator, first to a two-dimensional section of the blade and then to the entire three-dimensional blade. The selected stator cascade geometry is taken from the first stator of the one and half experimental axial turbine stage commonly referred to as the Aachen turbine [45], see Figure 4.10. The flow equations were solved using the Reynolds averaged Navier-Stokes solver available within the open-source CFD-solver SU2 [22, 46]. The turbulent equations were closed with the one-equation Spalart-Allmaras turbulence model [47], ensuring wall $y+$ below unity along the blade surface. The boundary conditions used for the simulation are summarized in Table 4.3. The stator

Table 4.3: Boundary conditions for the simulation of the axial turbine stator test case.

Property	Value	Units
Fluid	Air	-
$T_{\mathrm{tot,in}}$	305.7	K
$p_{\mathrm{tot,in}}$	0.149	MPa
θ_{in}	0.0	°
p_{out}	0.09	MPa
$I_{\mathrm{tur,in}}$	0.03	-
$\left(\frac{\mu_{\mathrm{tur}}}{\mu_{\mathrm{lam}}}\right)_{\mathrm{in}}$	100.0	-

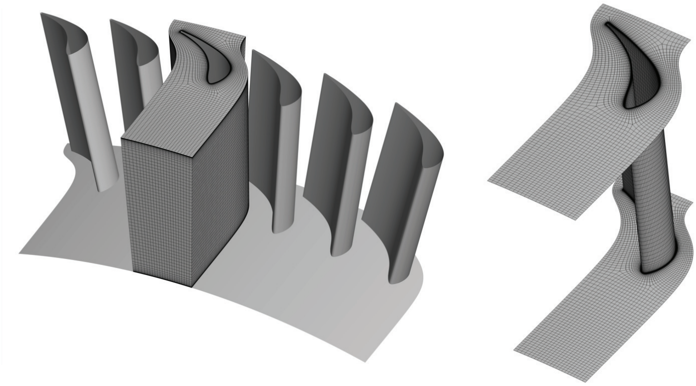

Figure 4.10: Grid generated for the axial turbine stator test case.

geometry was redesigned by solving the optimization problem:

$$\min_{\mathbf{D}} \quad s_{\mathrm{gen}}, \tag{4.40}$$

$$\text{s.t.} \quad \theta_{\mathrm{out}} > \theta_{\mathrm{baseline}}, \tag{4.41}$$

$$r_{\mathrm{out}} = r_{\mathrm{out,baseline}}. \tag{4.42}$$

The entropy generation, s_{gen}, and the flow outlet angle, θ_{out}, were computed using a mixed-out average [48] of the flow quantities at the inlet and outlet boundaries, specifically,

$$s_{\mathrm{gen}} = \frac{s_{\mathrm{out}} - s_{\mathrm{in}}}{\frac{v^2_{\mathrm{spout}}}{T_{\mathrm{tot,in}}}}, \tag{4.43}$$

$$\theta_{\mathrm{out}} = \arctan\left(\frac{v_{\mathrm{tang}}}{v_{\mathrm{ax}}}\right)_{\mathrm{out}}. \tag{4.44}$$

The trailing edge equality constrain was achieved by excluding from optimization the r_{out} design variable, namely the radius of curvature of trailing edge. The selected optimization method is the SLSQP algorithm [49], a gradient based optimizer available in the python SciPy library [50]. To guarantee a smooth convergence, the step size of the SLSPQ optimizer was under-relaxed with a value equal to 0.0005 for both the objective function sensitivity and the constraint sensitivity.

4.3.1 Optimization based on two-dimensional flow simulation

The mid-span of the prismatic stator geometry was used as the baseline geometry for the two-dimensional optimization. The flow domain was discretized using an in-house mesh-

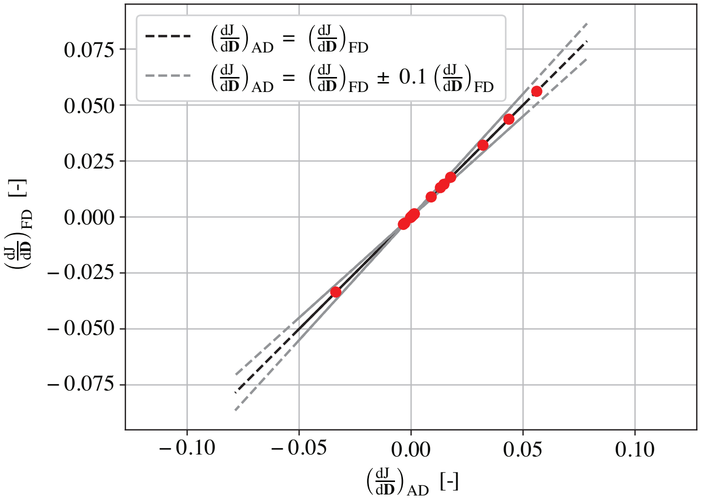

Figure 4.11: Gradient validation plot for two-dimensional design variables.

ing tool, resulting in an unstructured grid composed of 28000 elements, with hexahedral elements close to the wall surface and triangular in rest of the flow domain.

A maximum number of 7000 iterations was set to guarantee 3 order of magnitude of residual reduction for both the flow and the adjoint solver. The solutions were obtained by using an Euler implicit time-marching scheme with a CFL of 10 without resorting to the multi-grid acceleration technique.

The gradient of the objective function with respect to the design variables were validated using the forward finite-difference method, with a step size of 0.001. Figure 4.11 shows the gradient validation plot for the design variables required by the two-dimensional geometry. It can be observed that the magnitude of gradients obtained from finite-difference is very close to that obtained from adjoint, and the RMS error is less than 1e-6. This confirms that the coupling of adjoint with the CAD geometrical sensitivity is accurate and the adjoint equations have sufficiently converged to provide accurate sensitivity.

The cost of one direct simulation was 10 minutes of CPU-time, while that of the adjoint simulation was 13 minutes of CPU-time on a 6 core *Intel(R) Xeon (R) CPU E5-2670v2* CPU with 2.2 GHz clockspeed. The direct simulation required approximately 2 GB of RAM while the adjoint simulation required approximately 3 GB of RAM.

The normalized optimization history, see Figure. 4.12, shows that the optimum was achieved within 15 iterations. The entropy generation coefficient is reduced by approximately 10% and the inequality constraint on the outlet flow angle is satisfied. Figure 4.13 displays the obtained baseline and optimal blade profiles. As can be observed, the optimization process leads to a more straight rear suction side and to a higher blade curvature

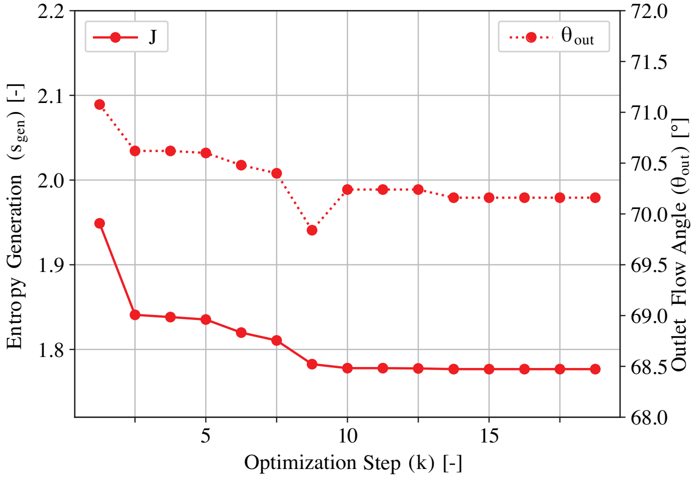

Figure 4.12: Optimization history of the two-dimensional problem.

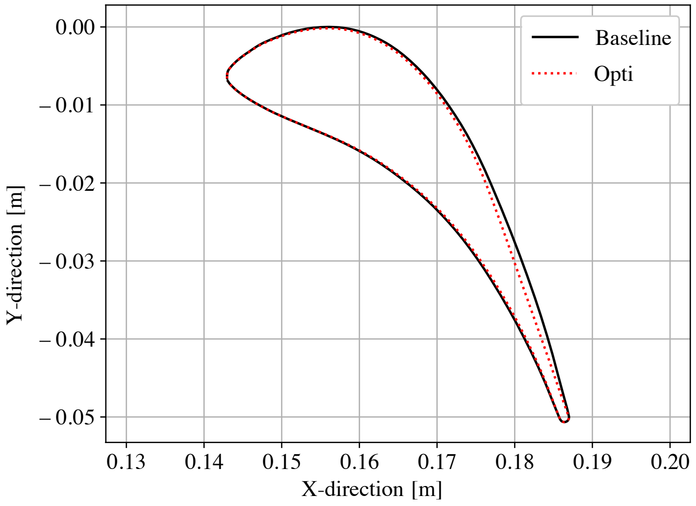

Figure 4.13: Baseline and the optimized blade geometry.

in the front part of the suction side. The consequence thereof is a more pronounced flow acceleration in the vicinity of the cascade throat and a smoother deceleration towards the trailing-edge, which is highly beneficial to reduce boundary layer and trailing-edge losses. This is clearly visible in both the Mach contour and in the isentropic Mach number distribution along the blade surface, see Figure. 4.14 and 4.15.

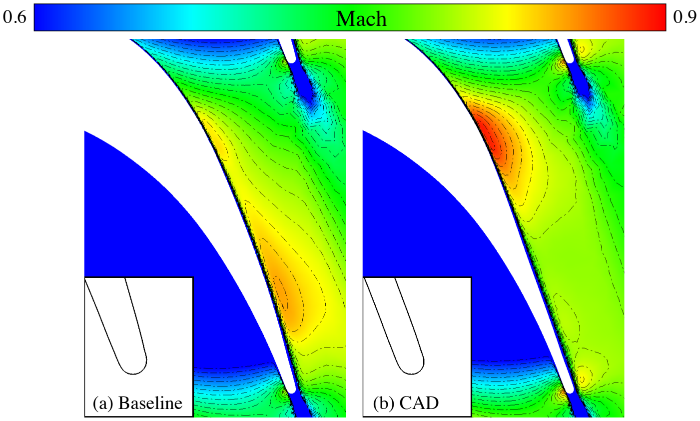

Figure 4.14: Mach contour of the baseline and the optimized geometry.

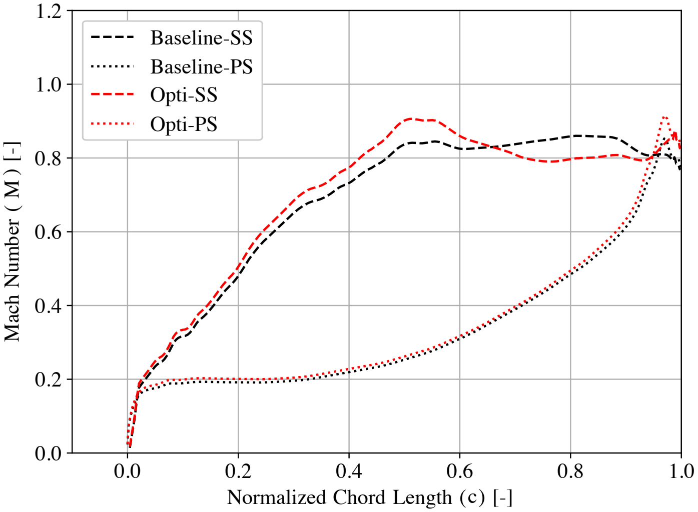

Figure 4.15: Isentropic Mach number distribution on the surface of baseline, CAD and FFD blade.

The advantage of adopting an optimization where the objective function is based on mixed-out averaging is apparent from Figure 4.16, which shows the pitch-wise Mach number distribution downstream of the cascade. The optimal geometry provides increased flow uniformity which allows to reduce the associated mixing-losses.

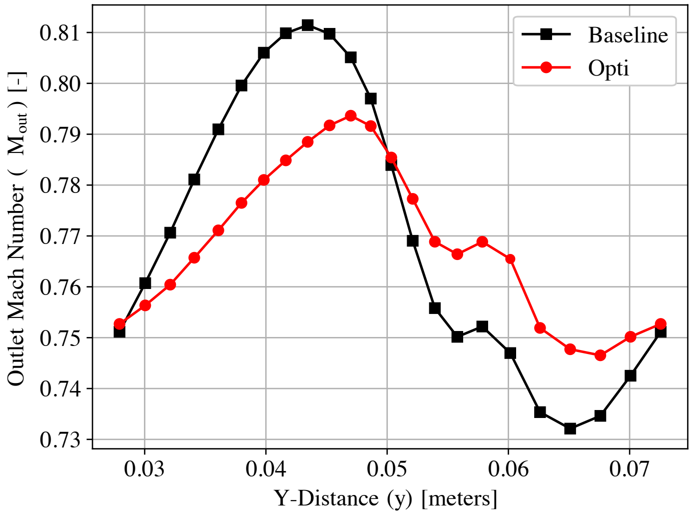

Figure 4.16: Pitch-wise Mach number distribution downstream of the cascade.

4.3.2 Optimization based on three-dimensional flow simulation

The flow domain was discretized using hexahedral elements where an expansion rate of the inflation layer is maintained between 1.1 and 1.5. The grid consists of approximately 500,000 elements with 90 span-wise sections and was generated using a commercial mesh generator [51]. The mesh elements close to the wall, i.e. the hub, the shroud and the blade, are clustered so as to maintain a y^+ of unity. The blade geometry and the discretized flow domain are illustrated in Figure 4.10.

A maximum number of 45,000 iterations was set for both the flow and the adjoint solver in order to guarantee a reduction of the value of the residual of at least 4 orders of magnitude. The convective fluxes are discritized using a central second-order Jameson-Schmidt-Turkel (JST) scheme [52]. Both solvers make use of an Euler implicit time-marching scheme with a CFL of 1.0, and 1D characteristics-based non-reflective boundary conditions [53] are used at both the inlet and the outlet of the flow channel.

The gradient validation was performed on the 47 design variables, see Table 4.2, using a first-order forward-difference scheme with a step size of 0.001. Figure 4.17 illustrates the gradient validation plot for the 47 design variables used to represent the prismatic blade geometry. For most design variables, the maximum root mean square difference between the gradient calculated as finite differences and those computed by the adjoing solver was 0.003. However, for few of the variables, the mismatch may be explained by the insufficient convergence obtained during the adjoint computation and the extremely low absolute value of the sensitivities.

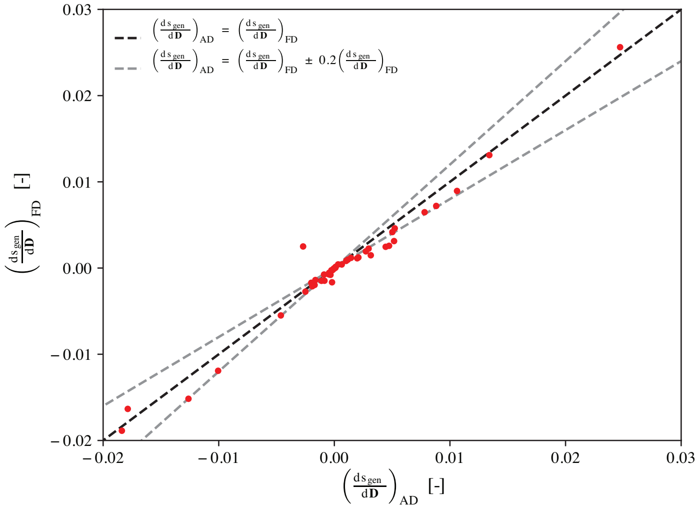

Figure 4.17: Adjoint against finite differences.

Simulations were run on a 20 core *Intel(R) Xeon (R) CPU E5-2670v2* CPU with 2.5 GHz clockspeed. The computational cost of one direct simulation was, on average, 609 minutes of CPU-time, while that of the adjoint simulation was 949 minutes of CPU-time. The direct simulation required approximately 17.3 GB of RAM while the adjoint simulation approximately 89.9 GB. However, the most memory demanding process was the gradient projection step, requiring approximately 140 GB of RAM.

The optimization history for both the objective function and the constraint is illustrated in Figure 4.18 and the corresponding baseline and optimized blade geometries in Figure 4.19. It can be observed that the entropy generation is reduced by 7.6%. The outlet flow angle value was reduced by 1.3% while maintaining the inequality constrain of $\theta_{\mathrm{out}} \geq 69.03°$.

Given the poor mesh quality obtained at the hub and at the shroud after the 7th design step, it was necessary to re-mesh the computational domain. The effect of generating a new mesh during the optimization process can be observed in Figure 4.18. Both the values of the objective function and the constrain considerably decrease as a result of the better mesh quality.

Figure 4.20 shows a comparison between the baseline and the optimized blade section at the hub, mid-span and shroud. It can be observed that majority of the geometrical changes are related to the stagger angles and opposite trends are featured between the hub and the shroud. The optimization procedure therefore leads to a twisted blade. In addition, it can be observed that the blade thickness changes along the chordline. More specifically, the blade tends to becomes slender towards the hub section. Furthermore, the

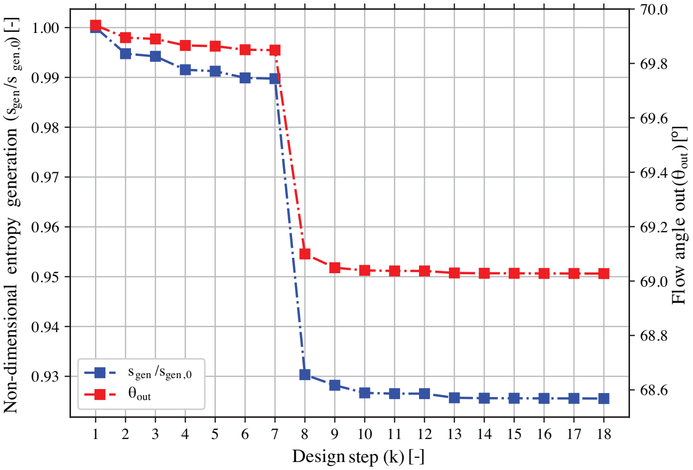

Figure 4.18: Optimization history and final optimized blade shape for the Aachen turbine stator test case.

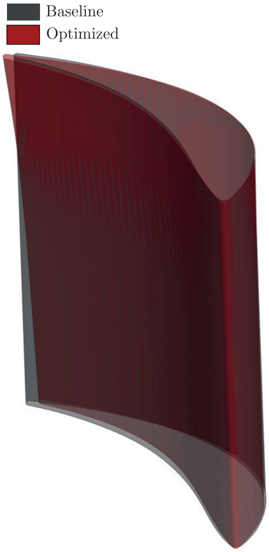

Figure 4.19: Visualization of overlapping blade surfaces of baseline (black) and optimized geometry (red).

trailing edge thickness of the baseline geometry remains unchanged by the optimization process. This is because the r_{out} variable controlling the thickness of the trailing edge is

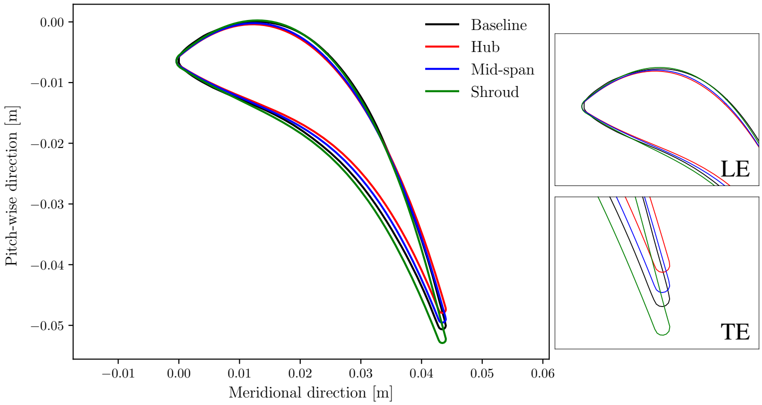

Figure 4.20: Detailed comparison between the optimized and baseline (prismatic) Aachen turbine stator shape for three different sections.

not prescribed as a design variable.

Figure 4.21 illustrates the flow Mach number contours around the blade sections corresponding to hub, mid-span and shroud of both the baseline and the optimized geometry. The plot of the simulated flow through the baseline cascade geometry shows that the fluid acceleration up to the throat is non-uniform. This is primarily due to the prismatic shape of the blade, which results in a larger flow passage area at the shroud than that at the hub. The different flow accelerations in the streamwise direction is made more evident in the boxed illustration of Figure 4.21, displaying the Mach number spatial distribution. The more uniform flow acceleration resulting from the optimization of the blade geometry yields also to a more even loading along the blade.

Figure 4.22 illustrates the computed outlet flow angle for the baseline and the optimized geometry. The flow angle caused by the baseline blade decreases from the hub to the shroud, while the turning of the flow generated by the optimized blade is rather uniform from the hub to the tip.

4.4 Conclusions

This chapter describes an innovative method for the parametrization of turbomachinery blades, which has the following main features 1) the mathematical description of the geometry depends on blade parameters that are univesally adopted for the design and manufacturing of actual turbines and compressors, and 2) the method is especially suited for a design optimization chain based on the adjoint approach. More specifically, and different from other blade parametrization methods, the sensitivity of the geometry is computed by means of the complex step method, which allows the integration of the parametrization

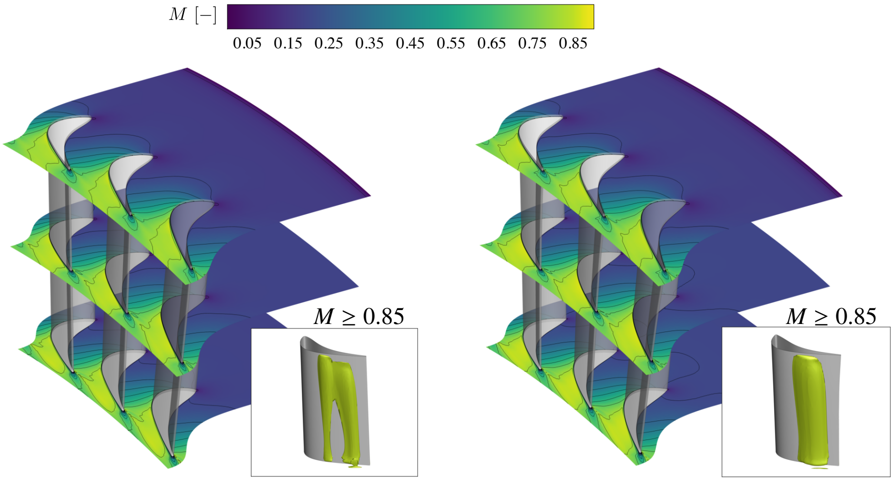

(a) Baseline.

(b) Optimized.

Figure 4.21: Flow Mach number contours resulting from RANS simulations (a) baseline and (b) optimized geometry.

method into the automated, gradient-based shape-optimization workflows.

The two-dimensional test case used to demonstrate the capability od the developed design chain showcased accurate validation of the sensitivity information obtained from the adjoint. The potential of the entire optimal design chain was successfully tested using a canonical axial turbine stator as base case and a relevant decrease of the related entropy generation coefficient was obtained, thanks to a resulting twisted geometry causing a more uniform flow distribution.

Nomenclature

Symbols

$\mathbf{B}$	blade parametrization algorithm
$\mathbf{C}$	curve values
c	chord length
$\mathbf{D}$	design variables
d	distance
$\mathbf{F}$	flow fluxes
$\mathbf{G}$	fixed point operator
f, g	endpoint curvature function
$\mathcal{H}$	transformation matrix
$\mathbf{I}$	identity matrix

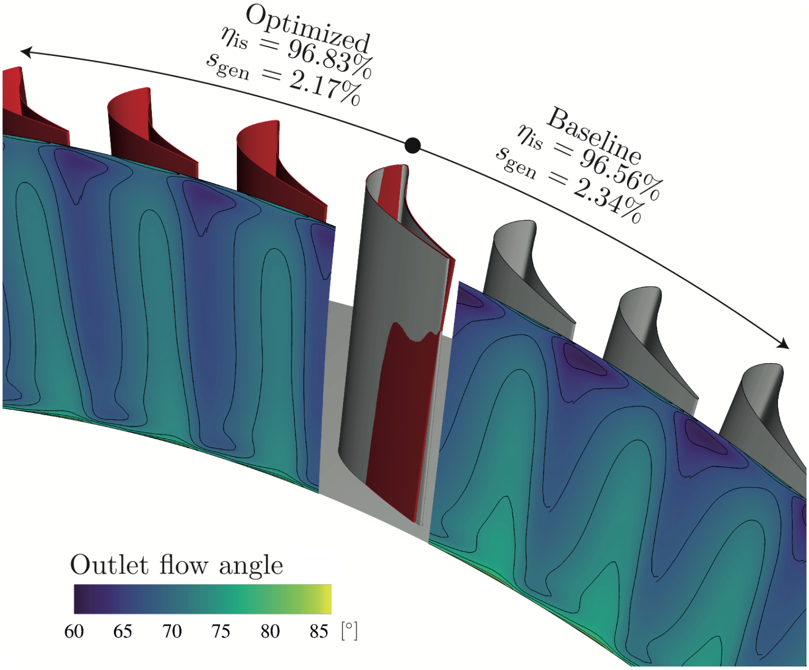

Figure 4.22: Outlet flow angle contour of the baseline and the optimized geometry.

$\mathbf{J}$	objective function
i, j	index
k	optimization step
L	arc length
$\mathbf{M}$	mesh deformation algorithm
M	Mach number
$\mathbf{n}$	unitary normal vector
n	number of control points
$\mathbf{P}$	control points
$\mathbf{Q}$	prescribed points
$\mathbf{R}$	residual
r	radius
$\mathbf{S}$	surface deformation algorithm
S	area
s	entropy
$\mathbf{T}$	projection matrix
t	thickness
$\mathbf{U}$	flow variables
$\mathbf{V}$	volume deformation algorithm

u, v	parametric cordinates
$\mathbf{X}$	points
x, y, z	cartesian cordinates

Greek letters

Δ	change in properties
η	efficiency
θ	metal angles
κ	curvature
ξ	stagger angle
τ	unitary tangent vector
Ω	element volume
∇	divergence

Superscripts

b	blade
c	camber
c	convective
l	lower
m	meridional
u	upper
v	viscous
*	converged solution

Subscripts

is	isentropic
in	inlet
out	outlet
i,j	index
0...3	index
surf	surface
CAD	computer aided design
AD	adjoint
FD	finite difference
tang	tangential
ax	axial
gen	generation

Accents

$\hat{\cdot}$	unit vector
$\bar{\cdot}$	adjoint variable

References

[1] Pini, M., Persico, G., Pasquale, D., and Rebay, S., 2014. "Adjoint Method for Shape Optimization in Real-Gas Flow Applications". *Journal of Engineering for Gas Turbines and Power,* **137**(3), p. 032604 (13 pages).

[2] Martins, J. R., Alonso, J. J., and Reuther, J. J., 2015. "A Coupled-Adjoint Sensitivity Analysis Method for High-Fidelity Aero-Structural Design". *Optimisation and Engineering,* **6**, pp. 33–62.

[3] Bahamonde, S., Pini, M., De Servi, C., Rubino, A., and Colonna, P., 2017. "Method for the Preliminary Fluid Dynamic Design of High-Temperature Mini-Organic Rankine Cycle Turbines". *Journal of Engineering for Gas Turbines and Power,* **139**(8), p. 082606 (14 pages).

[4] Agromayor, R., and Nord, L. O., 2019. "Preliminary Design and Optimization of Axial Turbines Accounting for Diffuser Performance". *International Journal of Turbomachinery, Propulsion and Power,* **4**(3), pp. 1–32.

[5] Damle, S. V., Dang, T. Q., and Reddy, D. R., 1997. "Throughflow Method for Turbomachines Applicable for All Flow Regimes". *Journal of Turbomachinery,* **119**(2), pp. 256–262.

[6] Persico, G., and Rebay, S., 2012. "A Penalty Formulation for the Throughflow Modeling of Turbomachinery". *Computers & Fluids,* **60**, pp. 86–98.

[7] Wu, H.-Y., Liu, F., and Tsai, H.-M., 2005. "Aerodynamic Design of Turbine Blades Using an Adjoint Equation Method". In Proceeding of 43rd AIAA Aerospace Sciences Meeting and Exhibit, pp. 1–13.

[8] Walther, B., and Nadarajah, S., 2012. "Constrained Adjoint-Based Aerodynamic Shape Optimization of a Single-Stage Transonic Compressor". *Journal of Turbomachinery,* **135**(2), pp. 1–10.

[9] Xu, S., Radford, D., Meyer, M., and Müller, J.-D., 2015. "CAD-Based Adjoint Shape Optimisation of a One-Stage Turbine With Geometric Constraints". In Proceeding of ASME Turbo Expo: Power for Land, Sea, and Air, pp. 1–14.

[10] Luo, J., Zhou, C., and Liu, F., 2013. "Multipoint Design Optimization of a Transonic Compressor Blade by Using an Adjoint Method". *Journal of Turbomachinery,* **136**(5), pp. 1–10.

[11] Walther, B., and Nadarajah, S., 2015. "Optimum Shape Design for Multirow Turbomachinery Configurations Using a Discrete Adjoint Approach and an Efficient Radial Basis Function Deformation Scheme for Complex Multiblock Grids". *Journal of Turbomachinery,* **137**(8), pp. 1–20.

[12] Vitale, S., Albring, T. A., Pini, M., Gauger, N. R., and Colonna, P., 2017. “Fully turbulent discrete adjoint solver for non-ideal compressible flow applications”. *Journal of the Global Power and Propulsion Society,* **1**, pp. 252–270.

[13] John, A., Shahpar, S., and Qin, N., 2017. “Novel Compressor Blade Shaping Through a Free-Form Method”. *Journal of Turbomachinery,* **139**(8), pp. 1–11.

[14] Tang, X., Luo, J., and Liu, F., 2018. “Adjoint Aerodynamic Optimization of a Transonic Fan Rotor Blade with a Localized Two-Level Mesh Deformation Method”. *Aerospace Science and Technology,* **72**, pp. 267–277.

[15] Gagliardi, F., and Giannakoglou, K. C., 2019. “RBF-Based Morphing of B-Rep models for Use in Aerodynamic Shape Optimization”. *Advances in Engineering Software,* **138**, pp. 1–17.

[16] Vitale, S., Albring, T. A., Pini, M., Gauger, N. R., and Colonna, P., 2017. “Fully turbulent discrete adjoint solver for non-ideal compressible flow applications”. *Journal of the Global Power and Propulsion Society,* **1**, pp. 252–270.

[17] Verstraete, T., Müller, L., and Müller, J.-D., 2017. “CAD-Based adjoint optimization of the stresses in a radial turbine”. In Proceeding of ASME Turbo Expo 2017, no. GT2017-65005, pp. 1–8.

[18] Banović, M., Mykhaskiv, O., Auriemma, S., Walther, A., Legrand, H., and Müller, J.-D., 2018. “Algorithmic Differentiation of the Open CASCADE Technology CAD Kernel and its Coupling with an Adjoint CFD Solver”. *Optimization Methods and Software,* **33**(4-6), pp. 813–828.

[19] Lyness, J. N., and Moler, C. B., 1967. “Numerical differentiation of analytic functions”. *SIAM Journal on Numerical Analysis,* **4**(2), pp. 202–210.

[20] Squire, W., and Trapp, G., 1998. “Using complex variables to estimate derivatives of real functions”. *SIAM Review,* **40**(1), pp. 110–112.

[21] Martins, J. R. R. A., Sturdza, P., and Alonso, J. J., 2003. “The Complex-Step Derivative Approximation”. *ACM Transactions on Mathematical Software (TOMS),* **29**(3), pp. 245–262.

[22] Economon, D. T., Palacios, F., Copeland, S. R., Lukaczyk, T. W., and Alonso, J. J., 2015. “SU2: An open-source suite for multiphysics simulation and design.”. *AIAA Journal,* **54**(3), pp. 828–846.

[23] Piegl, L., and Tiller, W., 2012. *The NURBS Book*, 2nd ed. Springer Science & Business Media.

[24] Arts, T., Lambert de Rouvroit, M., and Rutherford, A. W., 1990. Aero-Thermal Investigation of a Highly Loaded Transonic Linear Turbine Guide Vane Cascade: a Test Case for Inviscid and Viscous Flow Computations. Tech. Rep. 174, VKI Training Center for Experimental Aerodynamics.

[25] Arts, T., and Lambert de Rouvroit, M., 1992. “Aero-Thermal Performance of a Two-Dimensional Highly Loaded Transonic Turbine Nozzle Guide Vane: A Test Case for Inviscid and Viscous Flow Computations”. *Journal of Turbomachinery,* **114**(1), pp. 147–154.

[26] Stadtmüller, P., and Fottner, L., 2001. “A Test Case for the Numerical Investigation of Wake Passing Effects on a Highly Loaded LP Turbine Cascade Blade”. In ASME Turbo Expo: Power for Land, Sea, and Air, American Society of Mechanical Engineers Digital Collection, pp. 1–8.

[27] Anand, N., Rubino, A., Colonna, P., and Pini, M., 2020. “Adjoint-Based Aeroelastic Design Optimization Using a Harmonic Balance Method”. In ASME Turbo Expo: Turbomachinery Technical Conference and Exposition, no. GT2020-16208, American Society of Mechanical Engineers Digital Collection, pp. 1–12.

[28] Fransson, T. H., and Verdon, J. M., 1993. “Panel Discussion on Standard Configurations for Unsteady Flow Through Vibrating Axial-Flow Turbomachine-Cascades”. In *Unsteady Aerodynamics, Aeroacoustics, and Aeroelasticity of Turbomachines and Propellers*. pp. 859–889.

[29] Crouse, J. E., and Gorrell, W. T., 1981. Computer Program for Aerodynamic and Blading Design of Multistage Axial-Flow Compressors. Tech. Rep. TP 1946, NASA Lewis Research Center; Cleveland, OH, United States.

[30] Engeli, M., Zollinger, H. J., and Allemann, J. C., 1974. “A Computer Program for the Design of Turbomachinery Blades”. In Proceeding of ASME Turbo Expo, pp. 1–10.

[31] Goel, S., Cofer, John I., I., and Singh, H., 1996. “Turbine Airfoil Design Optimization”. In Proceedings of ASME Turbo Expo, pp. 1–10.

[32] Pierret, S., Demeulenaere, A., Gouverneur, B., and Van den Braembussche, R., 2000. “Designing Turbomachinery Blades with the Function Approximation Concept and the Navier-Stokes Equations”. In Proceeding of 8th Symposium on Multidisciplinary Analysis and Optimization, pp. 1–11.

[33] Oyama, A., Liou, M.-S., and Obayashi, S., 2004. “Transonic Axial-Flow Blade Optimization: Evolutionary Algorithms/Three-Dimensional Navier-Stokes Solver”. *Journal of Propulsion and Power,* **20**(4), pp. 612–619.

[34] Gordon, W. J., and Hall, C. A., 1973. “Construction of Curvilinear Coordinate Systems and Applications to Mesh Generation”. *International Journal for Numerical Methods in Engineering,* **7**(4), pp. 461–477.

[35] Golub, G. H., and Welsch, J. H., 1969. “Calculation of Gauss Quadrature Rules”. *Mathematics of Computation,* **23**(106), pp. 221–230.

[36] Korakianitis, T., and Papagiannidis, P., 1993. "Surface-Curvature-Distribution Effects on Turbine-Cascade Performance". *Journal of Turbomachinery,* **115**(2), pp. 334–341.

[37] Stephan, B., Gallus, H. E., and Niehuis, R., 2001. "Experimental Investigations of Tip Clearance Flow and Its Influence on Secondary Flows in a 1-1/2 Stage Axial Turbine". In Proceedings of ASME Turbo Expo, American Society of Mechanical Engineers Digital Collection, pp. 1–12.

[38] Jones, A. C., 1996. "Design and Test of a Small, High Pressure Ratio Radial Turbine". *Journal of Turbomachinery,* **118**(2), pp. 362–370.

[39] Keep, J. A., Vitale, S., Pini, M., and Burigana, M., 2017. "Preliminary Verification of the Open-Source CFD Solver SU2 for Radial-Inflow Turbine Applications". *Energy Procedia,* **129**, pp. 1071–1077.

[40] van Arnhem, N., de Vries, R., Sinnige, T., Vos, R., Eitelberg, G., and Veldhuis, L. L. M., 2020. "Engineering Method to Estimate the Blade Loading of Propellers in Nonuniform Flow". *AIAA Journal,* **58**(12), pp. 5332–5346.

[41] Pierzga, M. J., and Wood, J. R., 1985. "Investigation of the Three-Dimensional Flow Field Within a Transonic Fan Rotor: Experiment and Analysis". *Journal of Engineering for Gas Turbines and Power,* **107**(2), pp. 436–448.

[42] Pierzga, M. J., and Wood, J. R., 1989. Laser Anemometer Measurements in a Transonic Axial-Flow Fan Rotor. Tech. Rep. TP 2879, NASA Lewis Research Center; Cleveland, OH, United States.

[43] Dwight, R. P., 2006. "Robust mesh deformation using the linear elasticity equations.". In book Computational Fluid Dynamics, Springer, pp. 401–406.

[44] M. Sagebaum, T. Albring, N. G., 2019. "High-performance derivative computations using codipack". *ACM Transactions on Mathematical Software (TOMS),* **45**(4), pp. 1–26.

[45] Stephan, B., Gallus, H. E., and Neihuis, R., 2000. "Experimental Investigation of Tip Clearance flow and its influence on secondary flow in a 1-1/2 stage axial turbine". In Proceedings of ASME TurboExpo 2000, no. 2000-GT-0613.

[46] Albring, T. A., Sagebaum, M., , and Gauger, N. R., 2016. "Efficient aerodynamic design using the discrete adjoint method in SU2.". In Proceedings of 17th AIAA/ISSMO Multidisciplinary Analysis and Optimization Conference, no. AIAA 2016-3518, pp. 1–15.

[47] Spalart, P. R., and Allmaras, S. R., 1992. "A one-equation turbulence model for aerodynamic flows". *AIAA Journal,* **1**, pp. 5–21.

[48] Saxer, A. P., 1992. A numerical analysis of 3-D inviscid stator/rotor interactions using non-reflecting boundary conditions. Tech. rep., Cambridge, Mass.: Gas Turbine Laboratory, Massachusetts Institute of Technology.

[49] Kraft, D., 1988. “A software package for sequential quadratic programming.”. *Forschungsbericht - Deutsche Forschungs- and Versuchsanstaly fur Luft- and Raumfahrt*.

[50] Jones, E., Oliphant, T., Peterson, P., et al., 2001. SciPy: Open source scientific tools for Python. [Online; accessed 5th January 2021].

[51] Ansys, 2019. Turbo grid. Release 18.1.

[52] Jameson, A., 2017. “The origins and further development of the Jameson-Schmidt-Turkel scheme”. *AIAA Journal,* **55**(5), pp. 1487–1510.

[53] Giles, M. B., 1990. “Nonreflecting boundary conditions for euler equation calculations”. *AIAA Journal,* **28**(12), pp. 2050–2058.

5

Adjoint-based aeroelastic optimization using a Harmonic Balance method

The contents of this chapter appeared in:

N. Anand, A. Rubino, P. Colonna and M. Pini, 2020.
Adjoint-based aeroelastic design optimization using a harmonic balance method.
In Proceedings of the ASME Turbo Expo 2020, GT2020-16208, pages 1-12, September 2020.
An extended version of the article is in preparation and will be submitted to the
Journal of Turbomachinery.

© ASME 2020 - Reprinted with permission

Abstract. *Turbomachinery blades characterized by highly loaded, slender profiles and operating under unsteady flow may suffer from aeroelastic shortcomings, like forced response and flutter. One of the ways to mitigate these aeroelastic effects is to redesign the blade profiles, so as to increase aero-damping and decrease aero-forcing. Design optimization based on high-fidelity aeroelastic analysis methods is a formidable task due to the inherent computational cost. This chapter presents an adjoint-based aeroelastic shape-optimization framework based on reduced order methods for flow analysis and forced response computation. The flow analysis is carried out through a multi-frequency fully-turbulent harmonic balance method, while the forced response is computed by means of the energy method. The capability of the design framework is demonstrated by optimizing three candidate cascades, namely, i) a transonic compressor cascade, ii) a supersonic impulse turbine rotor operating with toluene as working fluid, initially designed by means of the method of waves and, iii) a three-dimensional transonic fan test case. The outcomes of the optimization show significant improvements in terms of forced-response in all the cases as a consequence of aero-damping enhancement.*

5.1 Introduction

Forced response and flutter are recurrent aero-elastic limiting factors for turbomachinery blades with slender profiles, high-aspect ratio, and markedly unsteady loading. Blades of this type are increasingly adopted in turbomachines of modern aero-engines [1], as a consequence of the effort to abate emissions by simultaneously increasing efficiency and reducing engine weight. Forced response phenomena are of particular concern in rotors of rocket engines and of supersonic turbines for organic Rankine cycle (ORC) power systems [2], due to the very high Mach number and associated strong shock waves, which may induce blade excitations deriving from stator-rotor interaction.

From a physical standpoint, both flutter and forced response occur if the blade structure absorbs energy from the fluid and reaches high vibration levels [1]. To mitigate this issue, one of the solutions is to re-design the blade by increasing the aero-damping, while maintaining aerodynamic performance. Usually, these design adjustments are performed downstream of the detailed fluid dynamic design, if potential structural issues are identified through comprehensive transient aero-mechanical calculations. This process is computationally expensive and predominantly based on designers' experience and, as such, it can arguably lead to final blade designs that are sub-optimal with respect to both aerodynamic and aeroelastic performance. Efficient automated design optimization procedures which can concurrently deal with the fluid-dynamic and the structural design problem can therefore aid the development of new blade concepts.

Adjoint-based design methods are suited for this purpose, due to the possibility to perform gradient-based optimization efficiently. However, the cost of performing a single time-accurate aero-elastic computation is still excessive, making adjoint optimization a very demanding task. In the attempt to circumvent this issue, reduced order models for

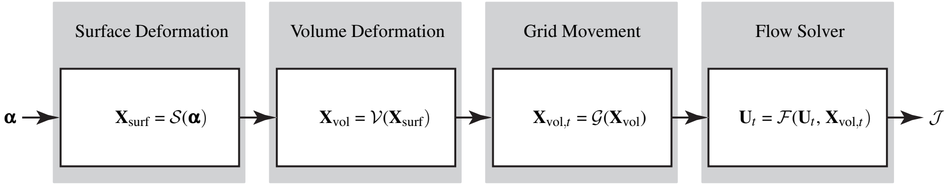

Figure 5.1: Simplified block scheme of the implementation of the fluid dynamic design chain (direct solver).

aero-elastic turbomachinery computations have been proposed [3, 4, 5, 6, 7], the vast majority of them being based on the so-called *energy method* [8]. This method enables flutter and forced response analysis with engineering accuracy by means of unsteady fluid-dynamic simulations. The method is based on the principle of energy conservation: the energy added by the flow-unsteadiness is equal to that dissipated by the vibrating blade [4, 9]. It is an alternative to the *modal reduction method* [10]. The *energy method* can be used as an efficient adjoint-based aero-elastic design optimization procedure, if the cost involved in performing unsteady flow computations can be greatly decreased. This can be accomplished with a time spectral or harmonic-balance method [11]. This approach has already been documented in the literature. Reference [5], for instance, documents the use of adjoint-based optimization to concurrently improve the aero-elastic and aero-dynamic performance of a transonic fan blade. Reference [6] presents the validation of sensitivities for an aero-elastic objective function calculated with the adjoint method and related to a 3D turbine test case.

The harmonic balance implementations currently documented in the literature are based on a single-frequency transformation for computational efficiency. As a result, flutter cannot be studied because it is inherently a multi-frequency flow problem [12]. Another limitation is the assumption of frozen viscosity, which implies that the turbulence sensitivities are not resolved during the adjoint computations.

This chapter documents a cost-effective adjoint-based optimization method and its application to aero-elastic design problems. The method is based on a multi-frequency harmonic balance solver for fully-turbulent flows [13, 14]. The method is capable of treating flows of fluids in both ideal and non-ideal thermodynamic states [15] and is implemented in the open-source software SU2. In works which preceded the development documented here, the FFD-box method was adopted for blade parametrization [13, 14], while a CAD-based surface method was conceived and implemented subsequently and it has been employed in this research [16, 17].

The capability of the method is demonstrated by performing the forced response minimization of three exemplary test cases, i.e., i) a transonic compressor cascade, namely the tenth standard configuration taken from Ref. [18], ii) a supersonic impulse turbine rotor operating with an organic working fluid, which is of interest because this type of turbine is employed in ORC power systems, and iii) a three-dimensional transonic fan test case commonly known as NASA rotor 67. These three test cases are characterized by slender blade profiles and strong shock-waves in the flow-domain, hence, are susceptible to aero-elastic effects.

5.2 Methodology

The methodology which was developed for this study can be described in three parts, namely, the part related to the direct solver, that related to the adjoint solver, and that related to the optimization. The algorithm implemented in the direct solver computes the solution of the flow equations and also morphs the mesh, in order to obtain the objective function. The adjoint solver provides the gradient of the objective function with respect to the design variables. The optimization algorithm utilizes the solutions and sensitivity values to obtain the result corresponding to the optimum design of the blade shape.

5.2.1 Direct solver

The computational procedure implementing the design chain illustrated in Figure 5.1 uses the design variables vector $\boldsymbol{\alpha}$ as input and returns the objective function $\mathcal{J}$. It consists of four main functions, namely, surface deformation, volume deformation, grid movement and flow solver.

5.2.1.1 Surface deformation ($\mathcal{S}$)

In order to deform the blade surface uniformly, a CAD-based parametrization method is used and the details of the method can be found in Ref. [17]. The parametrization algorithm is represented by the function $\mathcal{S}_{\text{CAD}}$ which operates on $\boldsymbol{\alpha}$, which is a vector made of blade design parameters like metal angles, chord and thickness distribution.

Using the surface parametrizer, the change in the surface grid ($\Delta\mathbf{X}_{\text{surf}}$) for the k^{th} design step is computed as

$$\Delta\mathbf{X}^k_{\text{surf}} \quad = \quad \mathcal{S}_{\text{CAD}}\left(\boldsymbol{\alpha}^k\right) - \mathcal{S}_{\text{CAD}}\left(\boldsymbol{\alpha}^{k-1}\right). \tag{5.1}$$

Subsequently, the surface coordinates ($\mathbf{X}_{\text{surf}}$) in the volumetric mesh for the k^{th} design step is calculated as

$$\mathbf{X}^k_{\text{surf}} \quad = \quad \mathcal{S}\left(\boldsymbol{\alpha}^k\right) = \mathbf{X}^{k-1}_{\text{surf}} + \Delta\mathbf{X}^k_{\text{surf}}. \tag{5.2}$$

5.2.1.2 Volume deformation ($\mathcal{V}$)

A mesh-deformation algorithm manipulates the volumetric grid by means of a linear elasticity method implemented in SU2. The linear system of equations to be solved at optimization step k is given by

$$\mathbf{K}\Delta\mathbf{X}^k_{\text{vol}} = \mathbf{T}\Delta\mathbf{X}^k_{\text{surf}}, \tag{5.3}$$

where $\mathbf{K}$ is the stiffness matrix, $\mathbf{T}$ is the transformation matrix and $\Delta\mathbf{X}_{\text{vol}}$ is the change in the volume mesh. The vector $\Delta\mathbf{X}_{\text{surf}}$ is used as a Dirichelet boundary condition for the linear-elasticity solver. The mesh coordinates ($\mathbf{X}_{\text{vol}}$) corresponding to the k^{th} optimization step can be represented as

$$\mathbf{X}^k_{\text{vol}} = \mathcal{V}\left(\mathbf{X}^k_{\text{surf}}\right) = \mathbf{X}^{k-1}_{\text{vol}} + \Delta\mathbf{X}^k_{\text{vol}}. \tag{5.4}$$

5.2.1.3 Grid movement ($\mathcal{G}$)

In order to simulate the unsteady motion of the blade due to vibrations, a deforming grid movement algorithm displaces the surface and the volume grid. The algorithm is the same as the one utilized for volume deformation. However, the change in surface mesh is provided by the grid movement procedure. More specifically, it is prescribed with a surface pitching subroutine in the simulations performed for this study. As a result, the linear system at time t for the k^{th} design step becomes

$$\mathbf{K}\Delta\mathbf{X}^k_{\text{vol},t} = \mathbf{T}\Delta\mathbf{X}^k_{\text{surf,pitch},t}, \tag{5.5}$$

and the volumetric mesh

$$\mathbf{X}^k_{\text{vol},t} = \mathcal{G}\left(\mathbf{X}_{\text{vol}}\right) = \mathbf{X}^k_{\text{vol}} + \Delta\mathbf{X}^k_{\text{vol},t}. \tag{5.6}$$

5.2.1.4 Flow solver

The unsteady flow solution is computed by using a time-domain Harmonic Balance (HB) solver. The final form of the RANS equations, discretized using the HB method described in Ref. [13], can be written as

$$\left(\frac{\Omega I}{\Delta t} + \mathbf{J}\right)\Delta\mathbf{U}_n = -\tilde{\mathcal{R}}_n\left(\mathbf{U}^q, \mathbf{U}^{q-1}\right), \qquad n = 0, 1, ..., N-1, \tag{5.7}$$

in which Ω is the computational cell volume, Δt is the pseudo-time step [11], $\mathbf{J}$ is the flow Jacobian, q is the physical time index, variable N is the number of resolved time instances, and $\tilde{\mathcal{R}}$ is the residual operator defined as

$$\tilde{\mathcal{R}}_n\left(\mathbf{U}^q, \mathbf{U}^{q-1}\right) = \mathcal{R}_n\left(\mathbf{U}^q\right) + \Omega \sum_{\mathrm{i}=0}^{N-1} H_{n,i} \Delta \mathbf{U}_i + \Omega \sum_{\mathrm{i}=0}^{N-1} H_{n,i} \mathbf{U}_i^q . \tag{5.8}$$

In Eqn. (5.8), $\boldsymbol{H}$ is the harmonic balance operator, calculated for a known set of k input frequencies corresponding to $N = 2k + 1$ time instances. $\mathbf{U}$ is the vector of conservative variables and it includes both laminar and turbulent quantities and $\Delta\mathbf{U} = \mathbf{U}^q - \mathbf{U}^{q-1}$.

Equation (5.7) is reformulated in terms of a fixed-point iteration as

$$\mathbf{U}_n^{q+1} = \mathcal{F}_n\left(\mathbf{U}^q\right), \tag{5.9}$$

where $\mathcal{F}$ is a fixed point iteration operator. According to the Banach fixed-point theorem, Eqn. (5.9) admits a unique fixed-point solution $\mathbf{U}^*$ such that

$$\tilde{\mathcal{R}}_n\left(\mathbf{U}^*, \mathbf{U}^{*-1}\right) = 0 \iff \mathbf{U}^* = \mathcal{F}_n(\mathbf{U}^*, \mathbf{X}). \tag{5.10}$$

5.2.2 Adjoint solver

The design chain whose implementation is illustrated in Figure 5.1 corresponds to the minimization problem

$$\min_{\alpha} \quad \mathcal{J}\left(\mathbf{U}_n(\alpha), \mathbf{X}_{\mathrm{vol},n}(\alpha)\right), \tag{5.11}$$

$$\text{s.t.} \quad \mathbf{U}_n(\alpha) = \mathcal{F}_n\left(\mathbf{U}(\alpha), \mathbf{X}_{\mathrm{vol}}(\alpha)\right), \tag{5.12}$$

$$\mathbf{X}_{\mathrm{vol},n}(\alpha) = \mathcal{M}_n(\alpha) = \mathcal{G}(\mathcal{V}(\mathcal{S}(\alpha))), \tag{5.13}$$

where, $\mathcal{M}$ is a differentiable function [14] which includes surface deformation ($\mathcal{S}$), volume deformation ($\mathcal{V}$) and grid movement ($\mathcal{G}$). The application of the *Lagrange multipliers* method to derive the adjoint equations gives the flow and mesh adjoint equations in the form

$$\bar{\mathbf{U}}_n = \frac{\partial \mathcal{J}}{\partial \mathbf{U}_n}^{\mathrm{T}} + \sum_{\mathrm{i}=0}^{\mathrm{N}-1} \frac{\partial \mathcal{F}_i}{\partial \mathbf{U}_n}^{\mathrm{T}} \bar{\mathbf{U}}_i, \tag{5.14}$$

$$\bar{\mathbf{X}}_n = \frac{\partial \mathcal{J}}{\partial \mathbf{X}_n}^{\mathrm{T}} + \frac{\partial \mathcal{F}_n}{\partial \mathbf{X}_n}^{\mathrm{T}} \bar{\mathbf{U}}_n, \tag{5.15}$$

where $\bar{\mathbf{U}}_n$ and $\bar{\mathbf{X}}_n$ are the flow and mesh adjoint variables. After solving the adjoint equations, the sensitivity of the objective function with respect to the volume mesh can be written as

$$\frac{\mathrm{d}\mathcal{J}}{\mathrm{d}\alpha} = \left[\frac{\mathrm{d}}{\mathrm{d}\alpha} \mathcal{M}_n^{\mathrm{T}}(\alpha)\, \bar{\mathbf{X}}_n\right]. \tag{5.16}$$

Subsequently, the sensitivity of the volume mesh with respect to $\boldsymbol{\alpha}$ can be computed as

$$\frac{\mathrm{d}\mathcal{M}_n}{\mathrm{d}\boldsymbol{\alpha}} = \frac{\mathrm{d}\mathbf{X}_{\mathrm{vol},n}}{\mathrm{d}\mathbf{X}_{\mathrm{vol}}} \frac{\mathrm{d}\mathbf{X}_{\mathrm{vol}}}{\mathrm{d}\mathbf{X}_{\mathrm{surf}}} \frac{\mathrm{d}\mathbf{X}_{\mathrm{surf}}}{\mathrm{d}\boldsymbol{\alpha}}, \tag{5.17}$$

where, the term $\frac{\mathrm{d}\mathbf{X}_{\mathrm{vol},n}}{\mathrm{d}\mathbf{X}_{\mathrm{vol}}}$ and $\frac{\mathrm{d}\mathbf{X}_{\mathrm{vol}}}{\mathrm{d}\mathbf{X}_{\mathrm{surf}}}$ is obtained by means of algorithmic differentiation, and $\frac{\mathrm{d}\mathbf{X}_{\mathrm{surf}}}{\mathrm{d}\boldsymbol{\alpha}}$ is obtained with the complex-step method within the CAD-based surface parametrizer.

5.2.3 Optimization

The forced response amplitude is calculated with the energy method, which must be supplied with the value of work-per-cycle obtained with two unsteady simulations, namely, the one corresponding to aero-forcing and the one corresponding to aero-damping.

The aerodynamic work is computed as

$$W = \int_t \oint_S -p \left(\hat{n} \cdot v_{\mathrm{grid}}\right) \mathrm{d}S \ \mathrm{d}t, \tag{5.18}$$

where, p is pressure, $\hat{n}$ is the normal vector and v_{grid} is the grid velocity.

The unsteady aerodynamic forcing calculation is performed on a non-vibrating blade under the influence of unsteady pressure at the blades natural frequency (necessary condition for resonance), while the aerodynamic damping calculation is carried out on a blade vibrating at its natural frequency with a modal amplitude of x_{CFD} in a uniform flow. In this study, a realistic value of x_{CFD} is used to simulate the vibrating blade at an inter blade phase angle of 0.

The resulting solution from the two unsteady simulations are used to compute the work-per-cycle using equation (5.18). The work associated with aerodynamic forcing (W_{f}) is the energy transferred to the blade structure due to the flow unsteadiness, while the aerodynamic damping work (W_{d}) is the energy dissipated by the vibrating blade. The forced response (x_{FR}) of a vibrating blade is defined, according to the energy method, as

$$x_{\mathrm{FR}} = \frac{W_{\mathrm{f}}}{-W_{\mathrm{d}}} \cdot x_{\mathrm{CFD}} \tag{5.19}$$

where, x_{CFD} is the modal amplitude imposed on the CFD mesh during damping calculation [4].

Table 5.1: Unsteady variables and boundary conditions for the three test cases.

Test Case	ω[rads/sec]	A_f[-]	A_d [-]	ϕ_in[°]	$p_\mathrm{tot,in}$[Pa]	$T_\mathrm{tot,in}$[K]	p_out[Pa]
Transonic Compressor	6.28	0.01	2.0	45	1e6	288.1	0.8e5
Supersonic Impulse Turbine	62.83	0.001	1.0	60	3e6	580.0	0.8e5
Transonic Fan	16686.26	0.015	1e-5	0	1e5	288.1	1.18e5

The forced response minimization problem can be written as

$$\min_{\alpha} \quad \mathcal{J}_\mathrm{FR} = x_\mathrm{FR}, \tag{5.20}$$

$$\text{s.t.} \quad W_\mathrm{f} > 0, \tag{5.21}$$

$$W_\mathrm{d} < 0, \tag{5.22}$$

where, $\mathcal{J}_\mathrm{FR}$ is the displacement amplitude computed with equation (5.19). The inequality constraints are imposed to prevent the inversion of signs during the optimization, which would change the physics of the problem.

The sensitivity of the objective function is computed by differentiating $\mathcal{J}_\mathrm{FR}$ with respect to the design variables $\boldsymbol{\alpha}$ and its expanded form is

$$\frac{\mathrm{d}\mathcal{J}_\mathrm{FR}}{\mathrm{d}\boldsymbol{\alpha}} = \left[\frac{\mathrm{d}\mathcal{J}_\mathrm{FR}}{\mathrm{d}\mathbf{X}_\mathrm{surf}}\right]_\mathrm{CFD} \cdot \left[\frac{\mathrm{d}\mathbf{X}_\mathrm{surf}}{\mathrm{d}\boldsymbol{\alpha}}\right]_\mathrm{CAD}, \tag{5.23}$$

which symbolize (5.16). The sensitivity of the objective function with respect to the surface $\frac{\mathrm{d}\mathcal{J}_\mathrm{FR}}{\mathrm{d}\mathbf{X}_\mathrm{surf}}$ can be further expanded as

$$\left[\frac{\mathrm{d}\mathcal{J}_\mathrm{FR}}{\mathrm{d}\mathbf{X}_\mathrm{surf}}\right]_\mathrm{CFD} = \left[-\frac{1}{W_\mathrm{d}}\frac{\partial W_\mathrm{f}}{\partial \mathbf{X}_\mathrm{surf}} + \frac{W_\mathrm{f}}{W_\mathrm{d}^2}\frac{\partial W_\mathrm{d}}{\partial \mathbf{X}_\mathrm{surf}}\right] \cdot x_\mathrm{CFD}. \tag{5.24}$$

The right-hand side of equation (5.24) can be calculated once the the direct and the adjoint solutions have been obtained.

5.3 Case Studies

The described optimization framework is applied to three exemplary test cases: a *transonic compressor cascade*, commonly known as the tenth standard configuration of the AGARD Manual [18], *supersonic impulse turbine rotor* designed with the method of waves [19] and operating with toluene as the working fluid, and a *transonic fan cascade*, commonly referred to as *NASA rotor 67* [20].

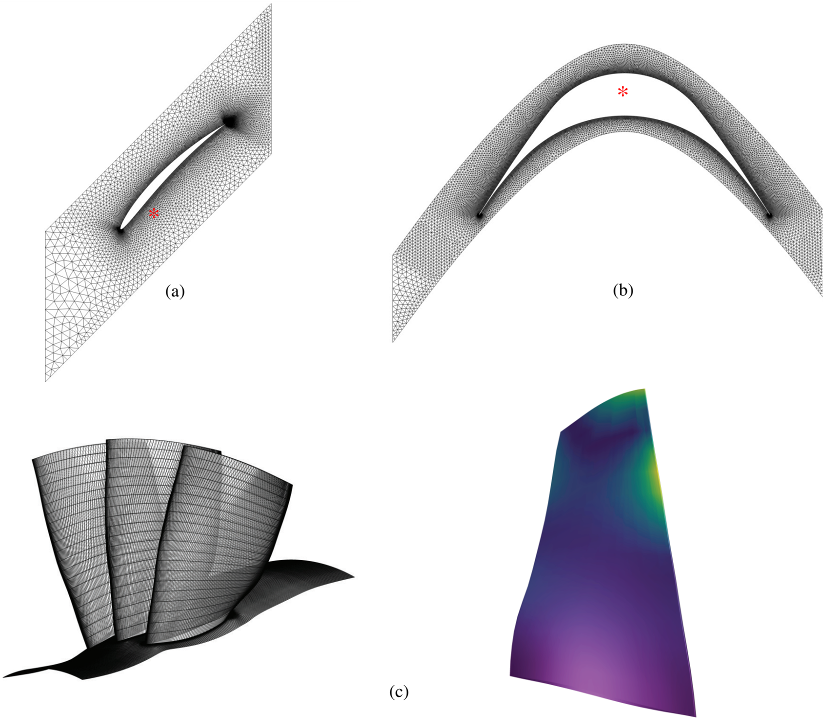

Figure 5.2: Discretization of the flow domain. (a) Transonic compressor blade, (b) Supersonic impulse turbine rotor, The red asterisk indicates the intersection of the pitching axis with the flow domain. (c) Transonic fan cascade, and vibration mode of the blade (right).

In the three cases, the aero-forcing calculation was performed by providing as input to the simulation the inlet total pressure according to the equation

$$p_{\mathrm{tot,in},t} = p_{\mathrm{tot,in}}\ \left[1 + A_{\mathrm{f}}\ \sin(\omega t)\right], \tag{5.25}$$

where, A_{f} is the amplitude of the pressure perturbation, ω is the angular velocity corresponding to the natural frequency of the blade and t is the time instance. Additionally, the aero-damping calculation for two-dimensional cases was performed by imposing a pitch angle to the blade surface about the defined axis, therefore the surface coordinates and the pitch angle are given by

$$\begin{aligned} \mathbf{X}_{\mathrm{surf},t} &= \mathbf{X}_{\mathrm{surf}}\ \mathbf{R}\left(\theta_{\mathrm{pitch},t}\right), && (5.26) \\ \theta_{\mathrm{pitch},t} &= A_{\mathrm{d}}\ \sin\left(\omega t\right). && (5.27) \end{aligned}$$

where, $\mathbf{R}$ is the rotation matrix and A_{d} is the modal amplitude. The pitching axis chosen for the two test cases is indicated with an asterisk in Figure 5.2. The vibrational motion of the three-dimensional case, the transonic fan cascade, was obtained by moving the surface nodes of the blade through the modal shape calculated with a commercial finite-element modal solver.

To perform CFD calculations, the flow domain of the two-dimensional cases was discritized using quadrilateral elements close to the blade surface so as to maintain $y^+ < 1$ and triangular elements in the rest of the flow domain [21]. The discretized flow domain, consists of 27,040 and 36,306 elements for the transonic compressor and the supersonic impulse turbine respectively. Similarly, for the three-dimensional case, a structured grid with approximately 100,000 hexahedral elements was used. The flow was modeled with the Reynolds Averaged Navier-Stokes (RANS) equations and the Spalart Allmaras turbulence model was selected to solve the transport equation for the kinematic eddy turbulent viscosity [22]. The unsteady flow term was solved using the HB method treated in Ref. [13].

The unsteady settings related to aero-forcing and -damping calculations like, angular velocity (ω), amplitude of inlet unsteadiness (A_f) and amplitude of modal displacement (A_d), along with the boundary conditions, are tabulated in Table 5.1. A maximum of 10,000 iterations was set for both the two-dimensional simulations and 25,000 for the three-dimensional simulation to assure a convergence of three orders of magnitude. For smooth convergence, mandatory for adjoint computations, the Euler semi-implicit time marching scheme with a CFL of 1.0 was used. The CFD simulations were performed with workstation equipped with an *Intel Xeon Processor E5-2687W v3* (3.1 GHz, 20 cores).

5.4 Results

The minimization problem defined by Eqn. (5.20) was solved for the three test cases using the SLSQP optimization algorithm [23] available in the Python SciPy library [24]. In order to enable smooth convergence, both the objective and the constrain sensitivities were under-relaxed by a factor of 0.005 and for simplicity only the thickness distribution was used as design variable.

5.4.1 Transonic compressor cascade

The work-per-cycle sensitivity of eight design variables, consisting of thickness distribution, from the aero-forcing and aero-damping simulations were validated against gradients calculated with forward-finite-differences, using a step size of 0.1%. The simulations correspnd to a reduced frequency of 0.002 and the unsteady variables used for the simulations is tabulated in Table 5.1. Figure 5.3 illustrates the gradient validation: it can therefore be inferred that the differentiation of the flow solver was performed correctly and that the adjoint-solver reached sufficient convergence. The direct solver computed a converged solution in 93 minutes and employed 15 GB of RAM, while the adjoint solver required 366 minutes and 18 GB of RAM for one design step.

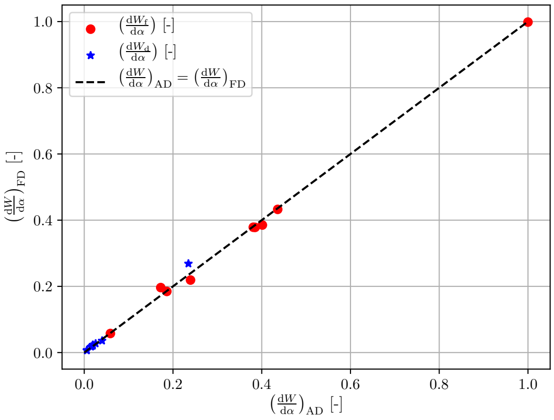

Figure 5.3: Gradient validation plot of work-per-cycle for the transonic compressor cascade. The horizontal axis represents the sensitivities obtained from the adjoint calculation and, the vertical axis represents that obtained from the finite-difference method. Where, ★ indicates the damping work and ● indicates the forcing work.

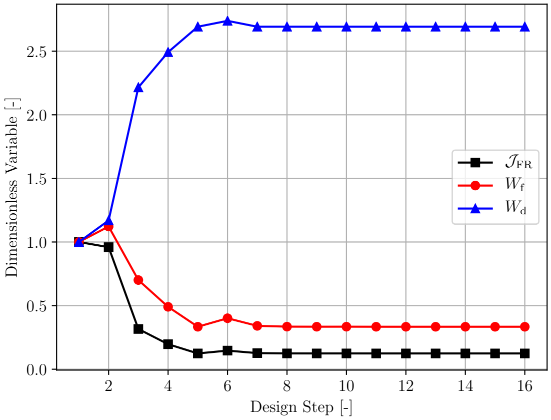

Figure 5.4: Optimization history of the forced response minimization calculation related to the transonic compressor cascade. Where, ▲ indicates the damping work, ● indicates the forcing work and ■ indicates the forced response displacement.

Figure 5.4 illustrates the optimization history of the forced response minimization problem. The value of the objective function $\mathcal{J}_\mathrm{FR}$ was reduced by 70% in 16 design steps, as a consequence of a reduction of the aero-forcing work by more than 50% and an increase of the aero-damping work by a factor of ~2.5.

The Mach number contours related to the flow around the baseline geometry and to

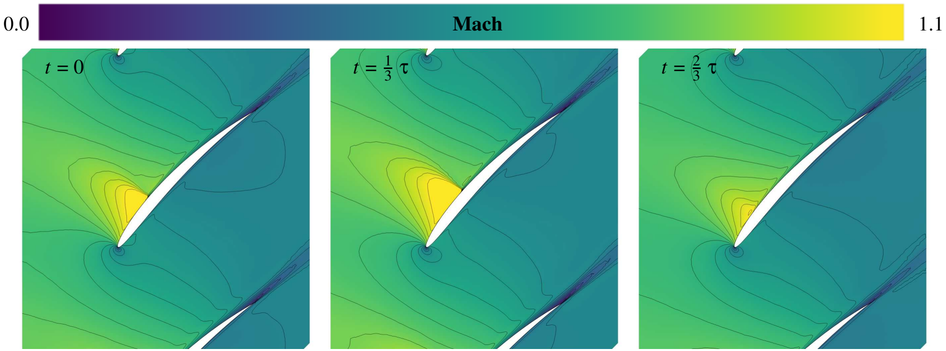

(a) Aero-forcing

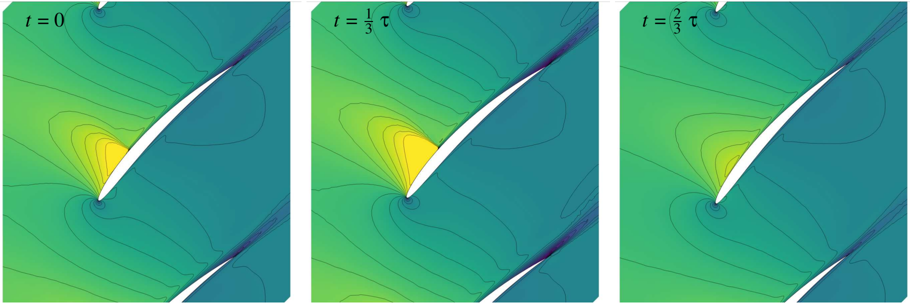

(b) Aero-damping

Figure 5.5: Mach number contours resulting from the simulation of the flow through the exemplary transonic compressor cascade at three time instances $t = 0$, $\tau/3$ and $2\tau/3$. (a) Aero-forcing, (b) Aero-damping.

aero-forcing and -damping simulations are illustrated in Figure 5.5. The flow accelerates from Mach 0.8, close to the leading edge, to a maximum of 1.1 on the suction side, triggering the formation of a shock in the fore part of the blade. It can be seen that the position and the strength of the shock varies in time as a consequence of the aero-forcing: the inflow velocity changes as a result of the fluctuating total pressure, see Figure 5.5(a).

Similar flow features can be observed in relation to the results of the aero-damping simulations, see Figure 5.5(b). However, in this case the change in the shock strength and position is due to the change in the angle of attack induced by the pitching motion.

Figure 5.6 illustrates the baseline blade geometry and the optimized geometry. The blade thickness of the optimized blade increases along the chord and the majority of the shape changes are located close to the pitching axis, between chord-length 0.2 and 0.4.

Figure 5.7 shows the mean and the alternating surface pressure, for the two aerodynamic simulations using the baseline and the optimized geometry. The sudden change in pressure at chord length ~0.25 is caused by the suction side shock-wave, as depicted in Figure 5.5. Due to the unsteadiness deriving from the pitching motion as well as from the

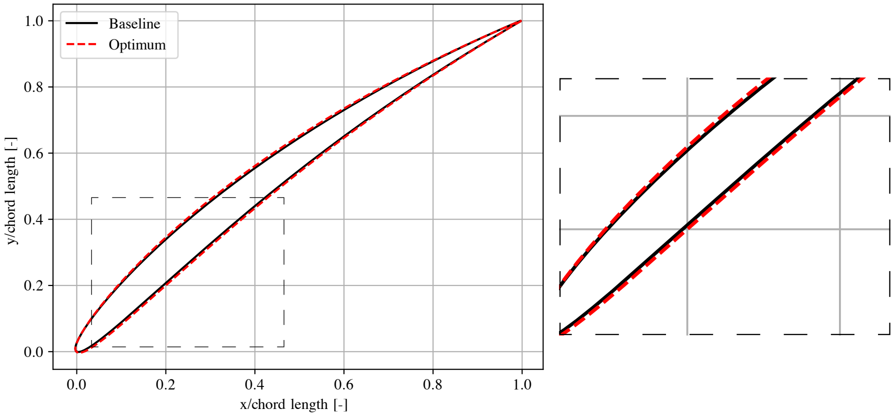

Figure 5.6: Baseline (solid) and optimum (dashed) blade geometry of the transonic compressor cascade.

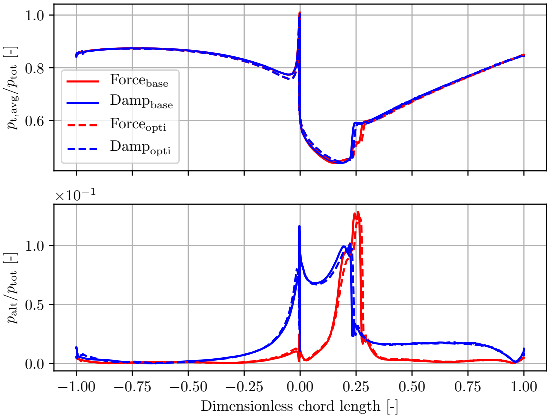

Figure 5.7: Time averaged (top) and alternating surface pressure (bottom) related to aero-forcing (red) and -damping (blue) simulations, for the baseline (solid) and the optimized (dashed) geometries related to the transonic compressor cascade. Negative and positive values of the chord length refer to the pressure and the suction side, respectively.

total pressure variation, the shock-wave induces a relatively high value of the alternating pressure (Figure 5.7, bottom).

The largest variations of the mean and alternating pressure affecting the optimized geometry for the aero-forcing and -damping are confined between the leading edge and one-quarter of the chord (see Figure 5.7). Additionally, it can be observed that in the baseline geometry a shock appears at a location corresponding to approximately 0.25 of

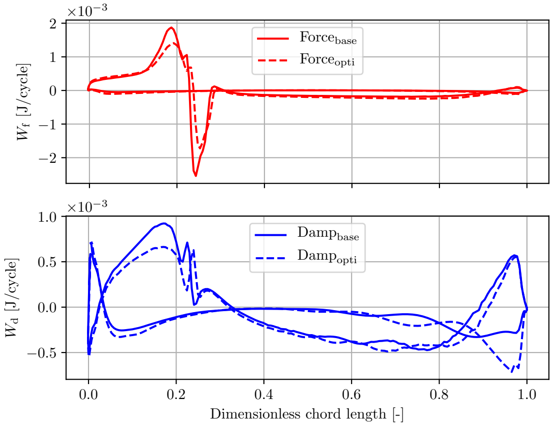

Figure 5.8: Local work for aero-forcing and -damping aerodynamic computations related to the transonic compressor cascade test case.

the chord length, while in the optimized geometry the shock appears at a location which is further downstream the blade profile. This is due to the larger blade thickness of the optimized geometry, see Figure 5.6, which leads to a smoother acceleration of the flow on the suction side. Furthermore, the optimization process causes an attenuation of the simulated flow unsteadiness, which can be inferred from the reduction of the alternating pressure, as depicted in Figure 5.7.

Figure 5.8 shows the comparison related to the work distribution along the blade profile between the baseline and the optimized geometry. It can be seen that the shockwave causes significant change in the work distribution in the front part of the blade. Moreover, the optimization tends to bring the aero-forcing work close to zero (see Figure 5.8, top), while making the local aero-damping work lower than that in baseline geometry (see Figure 5.8, bottom). This is eventually beneficial for the aero-elastic behaviour of the blade, as the aero-forcing work is in the numerator and the aero-damping work in the denominator of the objective function, see Eqn. (5.19).

5.4.2 Supersonic impulse turbine rotor

The validation of the adjoint-based gradients was not repeated for this test case because the results related to the compressor test case gave sufficient confidence about the accuracy of the method implementation. The unsteady simulations correspond to a reduced frequency of 0.034 and the values of the unsteady variable used for the simulations is tabulated in Table 5.1. In this case the direct solver computes a converged solution in 66 minutes and employed 14 GB of RAM, while the adjoint solver required 216 minutes to converge and 18 GB of RAM for one design step.

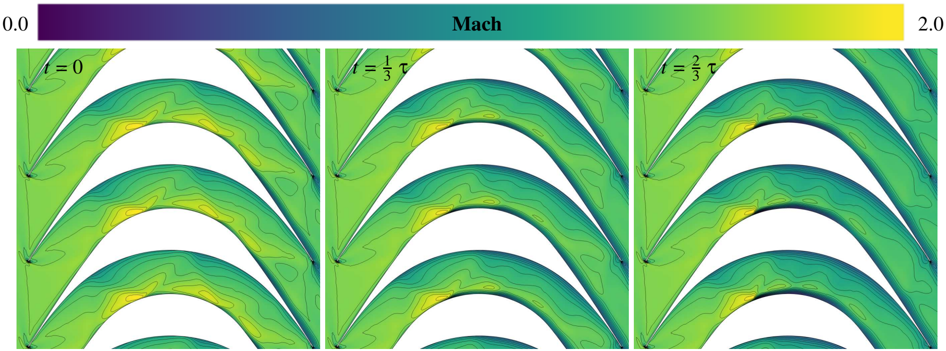

(a) Aero-forcing

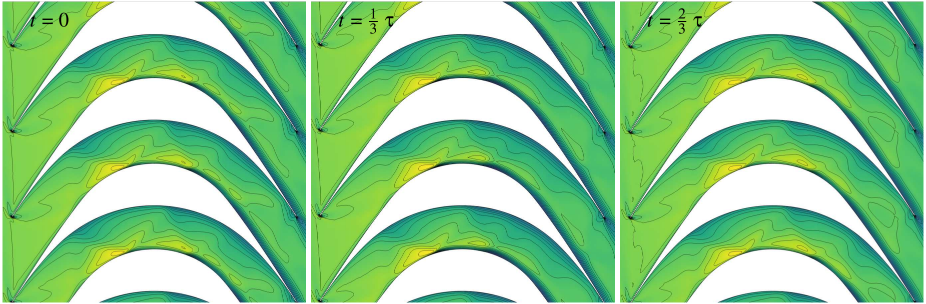

(b) Aero-damping

Figure 5.9: Mach number contours resulting from the simulation of the flow through the exemplary supersonic impulse turbine rotor at three time instances $t = 0$, $\tau/3$ and $2\tau/3$. (a) Aero-forcing, (b) Aero-damping.

The Mach number contours related to the flow around the blade obtained with the aero-forcing and -damping simulations for three time-instances are illustrated in Figure 5.9. The flow pattern indicates that the cascade is operating in the started flow regime [25], which is characterized by a shock-wave originating at the leading edge. The shock wave is then reflected multiple times along the flow passage. In the aero-forcing simulation, the variation of the total inlet pressure leads to a change in shockwave strength, angle and Mach contour. The same can be observed in relation to the flow field computed with the aero-damping simulation illustrated in Figure 5.9(b), as a result of the change in the incidence angle due to the pitching motion.

Figure 5.10 shows the optimization history of the forced response minimization problem. The value of the objective function $\mathcal{J}_{\mathrm{FR}}$ was reduced by 60% in 10 design steps, as a consequence of an increase of aero-damping work by a factor of 4, which counterbalances the increase of aero-forcing work by 1.5 times.

The mean and the alternating surface pressure distribution related to the two unsteady simulations is illustrated in Figure 5.11. In the mean pressure plot, Figure 5.11(top), the

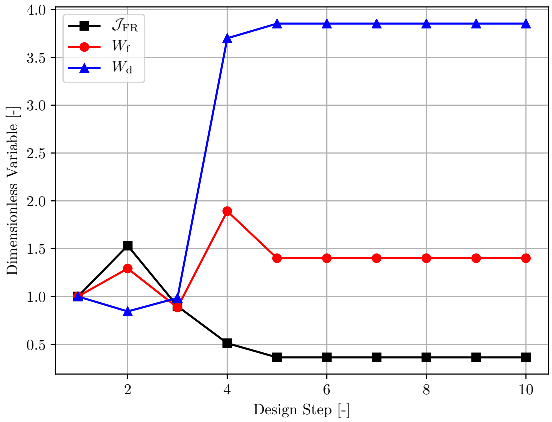

Figure 5.10: Optimization history of forced response minimization for the supersonic impulse turbine rotor. Where, ▲ indicates the damping work, ● indicates the forcing work and ■ indicates the forced response displacement.

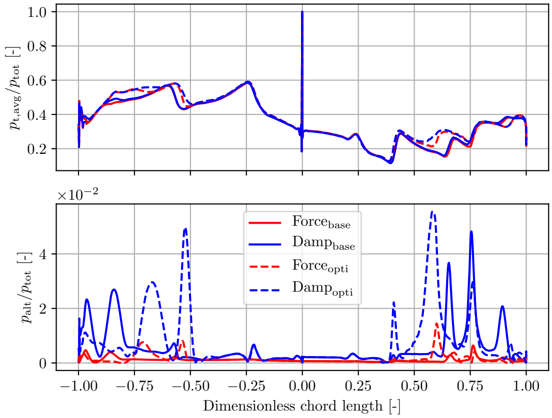

Figure 5.11: Time averaged (top) and alternating surface pressure (bottom) for the aero-forcing (red) and -damping (blue) calculation, for baseline (solid) and optimized (dashed) geometry. Negative and positive values of chord-length represent pressure and suction side.

abrupt pressure changes are due to the shockwave reflection. The alternating pressure values are negligible close to leading edge, see Figure 5.11(bottom), primarily due to the absence of unsteady effects prior to the first shock-wave impingement. In contrast, the flow field and the alternating pressure distribution in the rear part of the blade changes remarkably if compared to the baseline case. Moreover, the amplitude of the alternating pressure is much smaller for aero-forcing calculations if compared to that resulting from

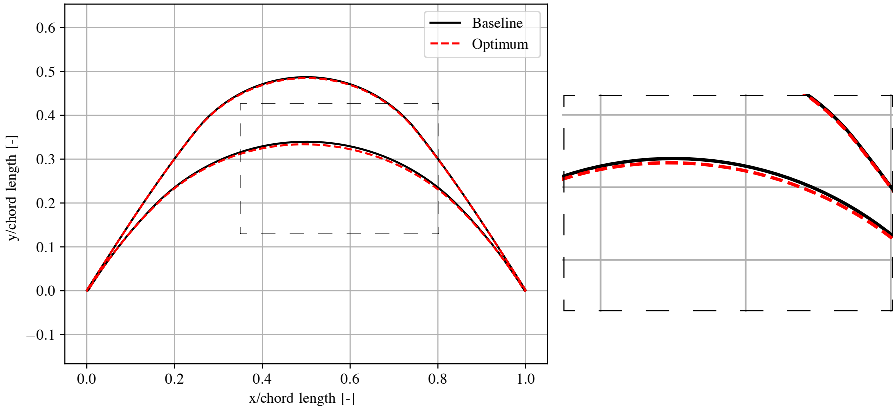

Figure 5.12: Baseline (solid) and optimized (dashed) geometry of supersonic impulse turbine rotor.

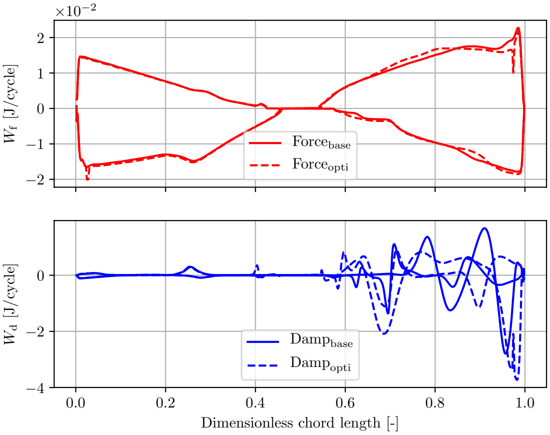

Figure 5.13: Local work plot for aero-forcing (top) and -damping (bottom) computation for baseline (solid) and optimized geometry (dashed).

the aero-damping calculations. This is due to the choice of a rather conservative value of A_f used for simulation.

The mean pressure distribution of the optimized blade geometry indicates that the majority of the shape changes are located between chord length of 0.4 and 0.8, see Figure 5.11(top). This can also be confirmed by looking at the baseline and optimized blade geometry plotted in Figure 5.12. The net result is the change in the shockwave pattern along the flow passage, which also influences the alternating pressure distribution.

Additionally, it can be noticed that the peaks of alternating pressure shift upstream and increase in magnitude for the optimized geometry. This can be deemed contradictory at first. However, the work calculation is also a function of the grid velocity, which becomes lower close to the axis of rotation. Consequently, a positive effect on the objective function can be achieved at the expense of an increase in the unsteady loading.

Figure 5.13 illustrates the comparison related to the work distribution along the blade profile between the baseline and the optimized geometry. It can be seen that the forcing work in the optimized geometry increases slightly, see Figure 5.13(top). Nevertheless, such an increase is more than compensated by a significant increase of the damping work within the chord-length of 0.5-0.8, which has a net stabilizing effect on the blade vibrations, eventually making the impulse airfoil less prone to aero-elastic failure.

5.4.3 Transonic fan

This test case is used to assess the capability of the aero-elastic design method to provide accurate sensitivities and performance improvements for more complex turbomachinery applications and to evaluate its scalability in terms of computational time and memory requirement. To simplify the problem, the calculations are performed by assuming shrouded blades, with free-slip boundary conditions applied to the hub and shroud.

In this case, 3rd bending mode of the blade vibration is simulated in the aero-damping simulation. This mode was selected in accordance with the previous forced-response study by Ref. [26], wherein, 3rd bending mode at frequency 2655.70 Hz cross the 11th engine order at 90% of the design rotational speed.

The direct solver computed a converged solution in 720 minutes and required 20 GB of RAM, while the adjoint solver required 1300 minutes and 90 GB of RAM for one design step. As opposed to the previous cases, the simulation was performed with a first-order spacial accuracy. This was necessary so as to achieve a smooth convergence of both the direct and the adjoint solver.

In spite full convergence of the flow and adjoint equations, the optimization was stopped after two design iterations. This was, on average, the poor mesh quality obtained after deforming the grid in the third design step. The geometry obtained after the second design step was however considered sufficient for the purpose of the investigation. This geometry is therefore termed as *optimized* hereinafter.

The optimization led to 0.2% reduction of the forced response objective as a consequence of 0.25% increase of the aero-damping work. Conversely, the change of the aero-forcing work resulted negligible. In addition, the aerodynamic performance of the blades remain unaffected by the optimization when compared to the baseline aerodynamic performance.

Figure 5.14 illustrates the contour of the surface displacement after the first design step. It can be observed that the overall deformation of the blade surface is 4e-5 times the tip radius, which is a result similar to that obtained for the two-dimensional test cases. In addition, it can be observed that the majority of the deformation occurs at the root of the pressure side.

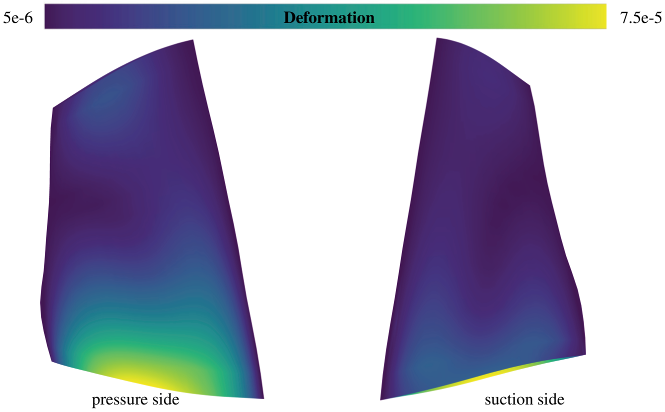

Figure 5.14: Contour of the magnitude of surface deformation imposed after the first design iteration.

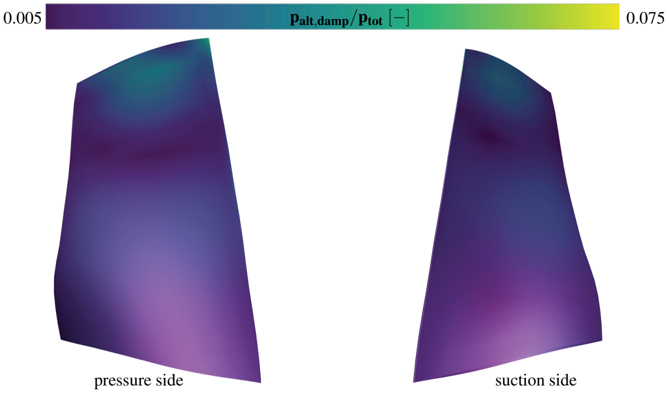

Figure 5.15: Contour of the dimensionless alternating surface pressure obtained by performing the aero-damping simulation of the baseline geometry.

Figure 5.15 illustrates the dimensionless alternating pressure obtained from the aero-damping simulation using the baseline geometry. It can be observed that the trend of the alternating pressure follows that of the vibration mode illustrated in Figure 5.2(c). This indicates that the alternating pressure resulting from the aero-damping simulation is primarily dictated by the vibrational motion of the blade. Besides, it also indicates that the pressure fluctuations due to the blade motion are of higher intensity than those induced by the shockwave.

Figure 5.16 displays, the dimensionless alternating surface pressure contour obtained

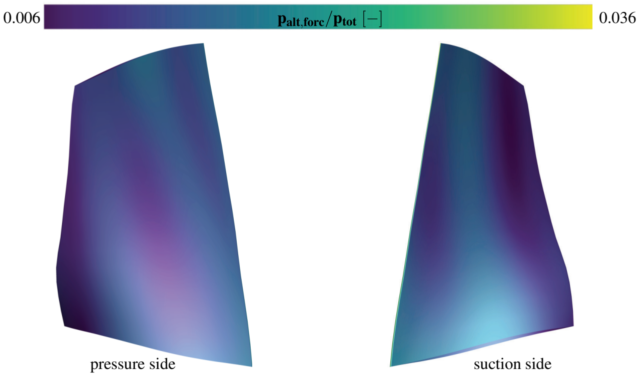

Figure 5.16: Contour of the dimensionless alternating surface pressure obtained by performing the aero-forcing simulation of the baseline geometry.

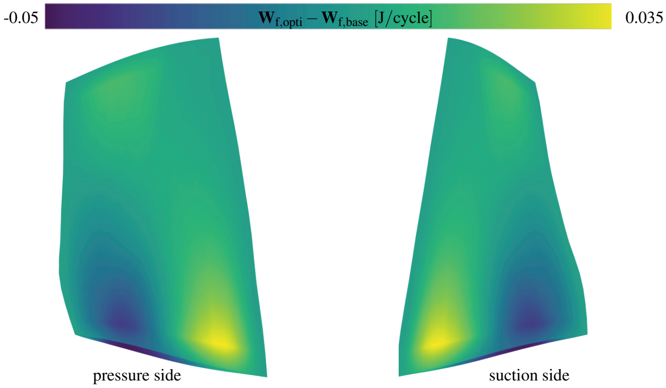

Figure 5.17: Difference between the local forcing work for the baseline and the optimal fan geometry.

from the aero-forcing simulation of the baseline geometry. It can be observed that high values of the alternating pressure are present on both the suction and the pressure side. This can be attributed to the change of the location of the shockwave impinging on both sides of the blade as result of the unsteady variation of the inlet total-pressure.

Figure 5.17 shows the surface contour of the difference between the aero-forcing work calculated for the baseline and the optimized geometry. It can be observed that the highest values are found close to the root of the blade. The difference ultimately tends to zero at the root as the grid velocity becomes null. When integrated over the blade surface, the overall change of the aero-forcing work becomes negligible, which is a confirmation of the negligible change of the aero-forcing work-per-cycle during the optimization process.

Figure 5.18 depicts the surface contour of the difference between the aero-damping

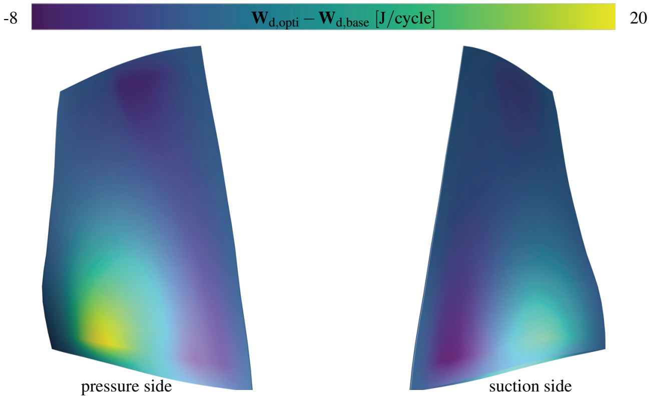

Figure 5.18: Contour of difference between the local damping work for the baseline and the optimal fan geometry.

work calculated for the baseline and the optimized geometry. It can be seen that the values of the aero-damping work of the optimized blade are lower than those of the baseline one. This has a stabilizing effect on the blade vibration, when subjected to forced response. From inspection of Figure 5.18 it can be also inferred that displacement of the blade surface geometry of 4e-5 times the tip radius are sufficient to considerably attenuate forced response effects, and this result demonstrates the potential of adjoint-based automated design for turbomachinery aero-elastic problems.

5.5 Conclusions

The objective of this work was the development and preliminary validation of a cost-effective adjoint-based forced response optimization framework for turbomachinery. The developed framework implements an uncoupled aero-elastic analysis procedure based on the energy method, in conjunction with a multi-frequency harmonic-balance method for fully-turbulent quasi periodic unsteady flows.

The capability of the method was assessed by performing the numerical optimization of two exemplary turbomachinery blades, namely, that of a transonic compressor cascade and that of a supersonic impulse turbine rotor operating with toluene as working fluid. The following conclusions can be drawn from the outcomes of the study:

1. The forced response is inherently dependent on both aero-forcing and aero-damping. Therefore, performing an optimization based only on one of the two phenomena does not guarantee the attainment of an optimized blade shape with superior aero-elastic performance.

2. Substantial improvements relates to forced response were obtained for both the considered two-dimensional test cases. In particular, for the transonic compressor case, a 70% improvement in forced response was attained as a consequence of more than 50% reduction in aero-forcing and $\sim$2.5 times increase in aero-damping. For the supersonic impulse turbine, the optimization led to a reduction of the forced response by 60% as a result of a 1.5 times increase in aero-forcing and a 4 times increase in aero-damping. In additions, for the three-dimensional transonic fan case, a 0.2% improvement in the forced response objective was obtained as a consequence of a 0.25% increase in aero-damping work and negligible change in the aero-forcing work.

3. In spite of the aeroelastic performance improvement, the entropy loss coefficient increases by 2% and 0.2% for compressor and the turbine case. Meanwhile, it remain unchanged for the transonic fan test case.

4. The computational time of a single aero-elastic design iteration was of the order of 7 hours for the transonic compressor cascade test case (the computational cost of the adjoint solver being three times that of the flow solver) and required $\sim$17 GB of RAM. Conversely, the time required by one design step for the supersonic impulse turbine rotor case was approximately 6 hours and required $\sim$15 GB of RAM. Additionally, the time required by one design step for the three-dimensional transonic fan case is approximately 33 hours and requires $\sim$90 GB of RAM.

Future work will deal with the application of the proposed method to realistic three-dimensional stage geometries and the extension of the current framework to multi-disciplinary design optimization problems.

Nomenclature

Symbols

A	amplitude
$\mathcal{F}$	fixed point iteration operator
$\mathcal{G}$	grid movement operator
H	harmonic-balance operator
I	identity matrix
$\mathcal{J}$	objective function
J	Jacobian
K	stiffness matrix
k	number of frequency
$\mathcal{M}$	mesh operator
N	total number of instances
$\hat{n}$	normal
p	pressure

$\mathcal{R}$	residual operator
R	rotation matrix
$\mathcal{S}$	surface operator
S	surface
T	transformation matrix
t	time
U	conservative variables
$\mathcal{V}$	volume operator
v	velocity
W	work-per-cycle
X	mesh coordinates
x	modal amplitude

Greek symbols

α	design variable vector
Δ	change in quantity
θ	rotation degree
ϕ	flow angle
τ	time period
Ω	cell volume
ω	angular velocity

Subscripts

alt	alternating
avg	average
base	baseline
CAD	computer aided design
CFD	computational fluid dynamics
d	damping
FR	forced response
f	forcing
grid	mesh grid
i	index
in	inlet
n	time instance index
opti	optimum
out	outlet
pitch	pitching
surf	surface
t	time
tot	total conditions
vol	volume

Superscripts

$*$	converged solution
$+$	plus
q	physical time index
T	transpose

References

[1] Srinivasan, A. V., 1997. “Flutter and resonant vibration characteristics of engine blades: An igti scholar paper”. *Journal of Engineering in Gas Turbines and Power,* **119**(4), June, pp. 742–775.

[2] Rinaldi, E., Pecnik, R., and Colonna, P., 2016. “Unsteady operation of a highly supersonic ORC turbine”. *Journal of Turbomachinery,* **138**(12), June, p. 121010 (9 pages).

[3] Chahine, C., Vestraete, T., and He, L., 2019. “A comparative study of coupled and decoupled fan flutter prediction methods under variation of mass ratio and blade stiffness.”. *Journal of Fluids and Structures,* **85**, pp. 110–125.

[4] Moffatt, S., and He, L., 2003. “Blade forced response prediction for industrial gas turbines part1: Methodologies”. In Proceedings of ASME Turbo Expo, no. 38640, ASME, pp. 407–414.

[5] He, L., and Wang, D. X., 2011. “Concurrent blade aerodynamic-aero-elastic deisgn optimization using adjoint method”. *Journal of Turbomachinery,* **133**(1), p. 011021 (10 pages).

[6] Engels-Putzka, A., Backhaus, J., and Frey, C., 2019. “Forced response sensitivity analysis using a adjoint harmonic balance solver”. *Journal of Turbomachinery,* **141**(3), p. 031014 (8 pages).

[7] Mayorca, M. A., Vogt, D. M., Fransson, T. H., and Martensson, H., 2012. “A new reduced order modeling for stability and forced response analysis of aero-coupled blades considering various mode families”. *Journal of Turbomachinery,* **5**(135), September, p. 051008 (10 pages).

[8] Carta, F. O., 1967. “Coupled blade-disk-shroud flutter instabilities i turbojet engine rotors”. *Journal of Engineering for Gas Turbine and Power,* **89**(3), July, pp. 419–426.

[9] Ning, W., Moffatt, S., Li, Y., and Wells, R. G., 2003. “Blade forced response prediction and industrial gas turbines part 2: Verification and application”. In Proceedings of ASME Turbo Expo, no. 38642, pp. 407–414.

[10] Mayorca, M. A., 2012. “Numerical methods for turbomachinery aeromechanical predictions”. PhD thesis, KTH, School of Industrial Engineering and Management (ITM), Energy Technology, Heat and Power Technology.

[11] Gopinath, A., van der Weide, E., Alonso, J., Jameson, A., Ekici, K., and Hall, K., 2012. “Three-dimensional unsteady multi-stage turbomachinery simulations using the harmonic balance technique”. In Proceedings of 45th AIAA Aerospace Sciences Meeting and Exhibit, pp. 1–20.

[12] Yao, W., and Marques, S., 2018. “A harmonic balance method for nonlinear fluid structure interaction problems”. *Computers & Structures,* **201**, May, pp. 26–36.

[13] Rubino, A., Pini, M., Colonna, P., Albring, T., Nimmagadda, S., Economon, T., and Alonso., J., 2018. “Adjoint-based fluid dynamic design optimization in quasi-periodic unsteady flow problems using a harmonic balance method.”. *Journal of Computational Physics,* **372**, pp. 220–235.

[14] Vitale, S., Albring, T. A., Pini, M., Gauger, N. R., and Colonna, P., 2017. “Fully turbulent discrete adjoint solver for non-ideal compressible flow applications”. *Journal of the Global Power and Propulsion Society,* **1**, pp. 252–270.

[15] Colonna, P., and Rebay, S., 2004. “Numerical simulation of dense gas flows on unstructured grids with an implicit high resolution upwind Euler solver”. *International Journal for Numerical Methods in Fluids,* **46**(7), pp. 735–765.

[16] Anand, N., Vitale, S., Colonna, P., and Pini, M., 2018. “Assessment of FFD and CAD-based shape parametrization methods for adjoint-based turbomachinery shape optimization.”. *Proceedings of Montreal, Global Power and Propulsion Forum.*(GPPS-NA-2018-135), pp. 1–8.

[17] Agromayor, R., Anand, N., Müller, J.-D., Pini, M., and Nord, L. O., 2021. “A unified geometry parametrization method for turbomachinery blades”. *Computer-Aided Journal,* **133**, p. 102987 (16 pages).

[18] Fransson, T. H., and Verdon, J. M., 1991. *Updated report on Standard Configurations for unsteady flow through vibration axial-flow turbomachinery-cascades*. July.

[19] Goldman, L. J., 1968. Analytical investigation of supersonic turbomachinery blade, ii-analysis of impulse turbine-blade sections. Tech. Rep. NASA TN-4422.

[20] Strazisar, A. J., Wood, J. R., Hathaway, M. D., and Suder, K. L., 1989. Laser anemometer measurements in a transnic axial-flow fan rotor. Tech. Rep. NASA-TP-2379.

[21] Ghidoni, A., Pelizzari, E., Rebay, S., and Selmin, V., 2006. “3D anisotropic unstructured grid generation”. *International Journal for Numerical Methods in Fluids,* **51**, pp. 1097–1115.

[22] Spalart, P. R., and Allmaras, S. R., 1992. “A one-equation turbulence model for aerodynamic flows”. *AIAA Journal,* **1**, pp. 5–21.

[23] Kraft, D., 1988. “A software package for sequential quadratic programming”. *Forschungsbericht-Deutsche Forschungs- and Versuchsanstaly fur Left- and Raumfahrt.*

[24] Virtanen, P., Gommers, R., Oliphant, T. E., Haberland, M., Reddy, T., Cournapeau, D., Burovski, E., Peterson, P., Weckesser, W., Bright, J., van der Walt, S. J., Brett, M., Wilson, J., Jarrod Millman, K., Mayorov, N., Nelson, A. R. J., Jones, E., Kern, R., Larson, E., Carey, C., Polat, İ., Feng, Y., Moore, E. W., Vand erPlas, J., Laxalde, D., Perktold, J., Cimrman, R., Henriksen, I., Quintero, E. A., Harris, C. R., Archibald, A. M., Ribeiro, A. H., Pedregosa, F., van Mulbregt, P., and Contributors, 2019. "SciPy 1.0–Fundamental Algorithms for Scientific Computing in Python". *arXiv e-prints*, Jul, p. arXiv:1907.10121.

[25] Paniagua, G., Iorio, M., Vinha, N., and Sousa, J., 2014. "Design and analysis of pioneering high supersonic axial turbines". *International Journal of Mechanical Sciences,* **89**, pp. 65 – 77.

[26] Oliveira, R., 2020. "Assessment and impact of aeroelastic effects in highly supersonic organic Rankine cycle turbines". Master's thesis, Delft University of Technology, the Netherlands.

6

Conclusions and Perspectives

Turbomachines operating under the influence of strong non-uniform flow often suffer from large fluid-dynamic penalties and are susceptible to premature structural failure. In order to reduce the negative impact of strong non-uniform flow on performance, two strategies can be undertaken. First, non-uniform aerodynamic loads can be reduced by means of advanced design methods, and, second, the blades can be made suitable to withstand the high load, by means of aero-elastic optimization.

This dissertation presents two automated methods which can reduce the negative impact of non-uniform flows on turbomachinery performance. One pertains to the detail design of stator vanes of supersonic turbines, while the other regards a cost-effective adjoint-based aero-structural shape optimization framework.

Based on the results presented in this dissertation, the following conclusions can be drawn:

Part I: Supersonic vane design

- The computed performance of the vane obtained by following the proposed design method is better than the considered baseline, which was obtained through automated CFD optimization. A radial vane geometry was tested by assembling it in a commercially operated ORC turbine, and the simulation results were confirmed. Therefore, supersonic vanes can be designed by relying on the novel and relatively inexpensive MoC-based design method rather than on expensive shape optimization techniques.
- The computed performance of symmetric and asymmetric MoC-based supersonic vanes is similar at design operating conditions. However, at off-design operating conditions, the performance of symmetric vanes is considerably superior. Therefore, a symmetric vane design should be adopted for all ORC power systems that often operate in off-design conditions, for example the envisaged waste heat recovery systems of long-haul trucks.
- The Deych's method, well-established for the design of conventional supersonic cascades, fails to accurately predict the optimum preliminary design parameters. Therefore, this method must not be used to design supersonic vanes of ORC turbines.

Part II: Adjoint-based shape optimization

- A CAD-based blade parametrization method enables proper handling of geometrical constraints and consequently improves the robustness of adjoint-based shape optimization.
- The solution of a forced response problem inherently depends on the coupling between aero-forcing and aero-damping work. Hence, aero-elastic blade optimization considering solely one of these quantities does not necessarily provide a solution to the forced response problem.

- Given a two-dimensional blade aero-elastic optimization problem, the computational cost of performing one design step involves a duration of 28 hours, if a 17 gigabytes RAM and 20 cores computer is employed. If a finite-difference method is adopted, the same design step requires 7 days with the same computer. Therefore, an adjoint-based framework should be adopted for the aero-elastic design optimization of turbomachinery.

The findings documented in this dissertation demonstrate the disruptive potential of automated design methods, especially for the design of turbomachines affected by strong non-uniform flows, particularly supersonic turbines and boundary layer ingestion fans. Supersonic turbines are the prime movers in thermal energy harvesting systems exploiting low-density energy sources, which could provide a substantial contribution to permanently address the questions related to climate-change. Similarly, the boundary layer ingestion propulsor has the potential to increase the propulsive efficiency by as much as 8% if compared to a conventional turbofan and is considered a leading technology in the effort of making aviation carbon-neutral.

All in all, further development of automated CFD-based design methods are accelerating the development of green turbomachinery concepts and will continue to do it in the foreseeable future. Hence, research on these topics could facilitate the achievement of our climate-neutral energy targets by the proposed time limit of year 2050.

Perspectives

The research presented in this dissertation is an active field, open for further investigation. Several considerations provide a compass to orient future efforts leading to results, which may be harvested by building up on the current foundation.

- Supersonic vanes of organic Rankine cycle turbines operating in regimes for which no nominal condition can be defined must be symmetric and designed according to a multi-point optimization method. A procedure to determine the points of operation must be devised, and consequently a multi-point optimization method developed.
- The numerous numerical experiments conducted at the basis of this research, highlighted that the SU2 flow solver is insufficiently robust for the case of supersonic flows. Therefore, to improve the convergence of the flow solver, further numerical features tailored to turbomachinery applications, like improved 2nd order advective schemes, need to be implemented. In addition, other improvements recently achieved by the SU2 developers community needs to be merged with the version containing the turbomachinery features.
- The optimization framework is being assessed on 1.5 axial stage test cases. Results put into evidence the impact of row interaction on the overall performance of the

turbine cascade. Hence, it can be argued that best optimization results can be obtained by applying the current framework to entire machines. This would possibly highlight the need for new optimization strategies to handle the large design space and limitations of the optimization infrastructure.

- The SU2 RANS solver used in this research was validated on test cases for which the working fluid obeys to the ideal gas law. The capabilities of the solver in case the flow exhibits non ideal gas dynamic effects has been assessed only by comparing overall calculated performance to one single set of measurements related to a high-speed mini-ORC turbine. Hence to gain further confidence in this type of fluid dynamic simulations, extensive experimental campaigns in a laboratory framework are required. In addition, such test-rig could also provide for back-to-back comparison of baseline and optimized design, thus quantifying the true potential of the adjoint-based optimization framework.

- All aero-elastic effects in blisk depend on the aerodynamic damping coefficient, which is therefore a critical parameter for aero-elastic design optimization. Hence, an optimization framework capable of optimally increasing or decreasing the aerodynamic damping coefficient of the blade for different vibrational modes could substantially improve the resulting aero-elastic design and it should be pursued.

- The adjoint-based shape optimization framework presented in this dissertation needs to be extended to encompass even more relevant physical effects. A truly multidisciplinary method could include heat transfer, rotor-dynamics and acoustics. The development effort would be large, but the envisaged results in terms of overall performance and time-to-market of products could be dramatic.

Appendix

A.1 Open-source software

A.1.1 ParaBlade

ParaBlade
A python based blade parametrization tool

ParaBlade is an open-source blade surface parametrization code. It is developed in python and is integrated with Pygmo optimization library and SU2-suite. It is available for use, download and contribute via the QR code below:

Figure 1: Link to ParaBlade GitHub page branch: `master`.

A.1.2 open-MoC

open-MoC

A python based Method of Charateristics tool

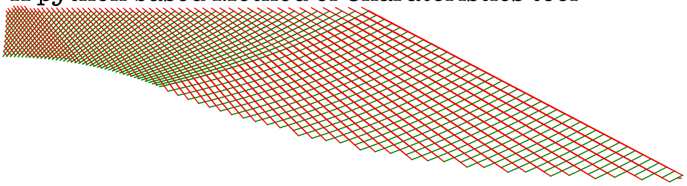

open-MoC is an open-access Method of Characteristics code to design de-Laval nozzle. The code is developed in python and is integrated to *CoolProp* and *FluidProp* thermodynamic libraries. It is available for use, download and contribute via the QR code below:

Figure 2: Link to open-MoC GitHub page branch: `master`.

A.1.3 SU2 Code

SU2-Code is an open-source multi-physics numerical suite. The code is developed and maintained by a diverse international community. The code is based in C/C++ and is wrapped with python for ease of use. The master version of the code is available in Git-Hub, while the code developed during the course of this research can be downloaded from the QR code below:

Figure 3: Link to SU2 Code branch: `feature_turbo_aeroelastic_AD`.

List of publications

Journal articles

Agromayor, R., **Anand, N.**, Pini, M., Nord, L. O., 2021. “Fluid Dynamic Design Optimization of a Transonic Axial Turbine for an Organic Fluid Test Rig”. *Global Propulsion & Power Journal*, In preparation.

Anand, N., Colonna, P., Pini, M., 2021. “Adjoint-based aeroelastic design optimization using a harmonic balance method”. *Journal of Turbomachinery*, In preparation.

Anand, N., Colonna, P., Pini, M., 2021. “Comparative Assessment of Asymmetric and Symmetric Supersonic Vanes at On- and Off-Design Conditions for High-Temperature Organic Rankine Cycle Turbines.”. *Journal of Engineering for Gas Turbine and Power*, In preparation.

Agromayor, R., **Anand, N.**, Muller, J. D., Pini, M., Nord, L. O., 2021. “A general parametrization and matching methodology for turbomachinery blades”. *Computer Aided Design Journal*, **133**, p. 102987 (16 pages).

Anand, N., Colonna, P., Pini, M., 2020. “Design guidelines for supersonic stators operating with fluids made of complex molecules”. *Energy Journal*, **203**, p. 117698 (9 pages).

Anand, N., Vitale, S., Pini, M., Otero, G.J., and Pecnik, R., 2018. “Design Methodology for Supersonic Radial Vanes Operating in Nonideal Flow Conditions”. *Journal of Engineering for Gas Turbines and Power*, **141**(2), p. 022601 (9 pages).

Conference proceedings

Sanghera, B. S., **Anand, N.**, Souverein, L., Penin, L., Pini, M., 2021. “Adjoint-based Optimisation of Rocket Engine Turbine Blades”. *Proceedings of the ASME Turbo Expo, 2021*, Virtual Online, GT2021-59580, pp. 1–12.

Anand, N., Rubino, A., Colonna, P., Pini, M., 2020. “Adjoint-based aeroelastic design optimization using a harmonic balance method”. *Proceedings of the ASME Turbo Expo*

2020, Virtual Online, GT2020-16208, pp. 1–12.

Anand, N., Colonna, P., Pini, M., 2019. “Design Guidelines for Supersonic Vanes Operating with Non-ideal Compressible Flows”. *Proceedings of the 5th International Seminar on ORC Power Systems – ORC-2019*, Athens - Greece, Paper ID: 022, pp. 1–9.

Anand, N., Vitale, S., Colonna, P., Pini, M., 2018. “Assessment of FFD and CAD-based shape parametrization methods for adjoint-based turbomachinery shape optimization.”. *Proceedings of Montreal 2018 Global Power & Propulsion Society Forum*, Montreal, Canada, GPPS-NA-2018-135, pp. 1–8.

Presentations

Anand, N., Pini, M., Colonna, P., 2020. “Adjoint 3D Aeroelastic Turbomachinery Optimization using Harmonic Balance”. *SU2 Conference*, Live Online.

Anand, N., Pini, M., Colonna, P., 2019. “Turbomachinery Capabilites in SU2: Status of Current Developments and Future Perspectives”. *SU2 Developers Meet*, Varenna, Italy.

Acknowledgements

The story of this research goes beyond these 140 odd pages and the four years of tenure. The countless number of coffee breaks, night-outs, drinks, bike falls and jokes required to achieve the objectives of this research cannot be overstated.

I would like to first thank my *copromotor* Dr.ir. Matteo Pini, his patience and appreciation for the baby steps in my research have been detrimental to the accomplishment of the goals of this dissertation. I am grateful to my *promotor*, Prof.dr.ir. Piero Colonna, whom I owe to regarding becoming a mature writer and an independent researcher. I would also like to express my gratitude to the *committee members* who took out time from their busy schedules to evaluate my dissertation and provide me with valuable feedback.

I would like to thank my collaborators Roberto, Gustavo, Salvo, Antonio, Zhang, Rubin and Simao. Working with you was truly an enriching experience and I hope we keep doing that in the future. I would like to acknowledge my collaborators at the Process and Energy Department (Stephan and René) and partners (and friends) at Triogen (Jos, Quirijn, Bas and Erik).

This project would not have been possible without the funding from the Applied and Engineering Sciences Division of the Dutch Research Council (NWO) and the support of the Guidance Committee of the project. The regular progress meetings have provided me with an outside perspective on my research, accompanied by rich feedback and suggestion. Thank you Dr. Leo Korstanje (NWO), Rogier Lammers (Mitsubishi Turbocharger and Engine Europe), Dr. Bambang Soemarwoto (NLR), Prof.dr. Damian Vogt (University of Stuttgart), Dr. Lars Axelsson (OPRA Turbines) and Willy Ahout (MTT).

During my research, I had the opportunity to work with some of the brightest master students. Their work helped me explore every crossroads that I encountered during my research. They have contributed to my knowledge and to this dissertation. I am thankful to my students: Jozef, Pablo, Ricardo, Shubhum, Federico, Hendrik, Hiera, Evert, Alex and Laurent.

Special thanks to Nando for translating the summary and proposition of this dissertation.

The only thing that kept me sane behind my workstation looking at those SU2 residuals with little to no hope of convergence was the emotional and psychological support of my PhD peers. In my early days as a PhD, they questioned my life choices. However, after my go/no-go meeting they knew I was hooked. They finally considered me one of them and provided me with a survival guide. Andre introduced me to his best friend (also my best friend now), beer. I was brought up to speed with necessary hipster-ness by Adam, Salvo and Imco. Meanwhile, Sebastian taught me how to be vigilant as “anyone can stab you from behind any day” (typical South American saying). Lucia always reminded me how uneducated I am by throwing at me some adjoint jargons, but then feeding me with some superb Italian food. Besides all this, I also learnt how to be Dutch thanks to Nando, Tom and Thomas. In contrast, I am also happy that I did not learn anything from Reynard, Federico and Sumit. It was fun to be part of the coolest PhD room on the sixth floor, I would like to thank my office mates old and new (Andrea, Matteo, Karthick, Federico, Nitish, Francesco, Andrea, Federica and Leonardo) and my friends from other PhD rooms (Maurice, Akshyeee, Biagio, Carmine, Rishikesh, Martijn (1 & 2), Anne and PJ).

Covid was especially difficult for all of us. However, regular beer meets (thanks to Thomas and Maurice), PP digital get together (thanks to Piero), Among Us (thanks to Sumit and co.), barely legal dinners (thanks to Adam, Reynard, Nando and André), *fietsen* (thanks to Nando, Imco, PJ, Biagio, Francesco and Martijn) and PUBG (thanks to Viraj, Ali, Junaid, Maximus) helped me fight through these difficult times.

I would like to thank my small family here in the Netherlands who always stood by me and lent me their ears without any reservations at some of my most difficult times. Your love and affection made this small city feel like home, thanks a lot for providing me with this safe space, Adam, Max, Sebastian, Cristina, André, Elisa, Anne, Nando, Sumit, Siddharth, Mattia.

Since I came to the Netherlands my friends from my early master days helped me take the blow of the cultural shock. My buddies from the Aeroflot flight SU233 from New Delhi (Mohit, Aashish, Sid and Ameya) and my fellow MSc buddies from the solid and fluid mechanics track (Nishant, Souvik, Christian, Rhoheth, Rahul and Prateek).

No matter how many friends I make around the world “old is gold”. My friends from India, more specifically from MechVilla: Reema, Nitisha, Arvind, Maal, Sid, Vineet, Pinkoo, Sneha, July, Surjo, Aakash, Roshni and Panda. Thanks for making my every visit back home warm and pleasurable.

My love goes to my extended family Sume, Shalu, Jeet, Titu, Bunty, Ravi, Anubha, Arpan and all beloved badepapa, badimaa, buas’, mausis’, phuphas’ and mausas’. Last but not least I would like to thank my brother Atul, bhabhi Manjari, mom and dad for their unconditional love, and for providing me with the foundation to dream big and fly high always. Special thanks, to my dearest Mitul for always surprising me with his knowledge and curiosity.

Nitish Anand
Delft, May, 2021.

About the author

Nitish Anand was born in Jamshedpur, India, on October 12^{th}, 1989. He did his Bachelor studies at the Institute of Technical Education and Research, Odisha, India and obtained his degree in August of 2012. After his Bachelors he was offered the position of Assistant Manager at Mahindra & Mahindra. He joined Mahindra's "Mahindra Research Valley" in Chennai, India. During his tenure at Mahindra, he was responsible for conducting vehicle level performance tests, like fuel efficiency, drive cycle development, vehicle ride and comfort, accelerated durability and coast-down tests. His curiosity about the energy balance in a vehicle motivated him to pursue a Masters degree in Energy Technology. In August of 2014, he started his Master studies at the Process and Energy department of 3mE faculty of Delft University of Technology. During his master thesis project, he proposed a supersonic vane design method and obtained his Master's degree in August of 2016.

His enthusiasm in energy technology kept him in the university to pursue his PhD in the Propulsion and Power Group at the Aerospace Engineering faculty of Delft University of Technology, the Netherlands.